



# **Magnetic Field Energy Harvesting for Smart Grid Applications**

by

**Sheng Yuan**

Submitted in accordance with the requirements for the award of  
the degree of Doctor of Philosophy of the University of  
Liverpool

August 2016

# Copyright

Copyright © 2016 Sheng Yuan. All rights reserved.

The copyright of this thesis rests with the author. Copies (by any means) either in full, or of extracts, may not be made without prior written consent from the author.

*To my family and my friends: Thank you for your support.*

# Table of Contents

|  |             |
|--|-------------|
| <i>Copyright</i>   | <i>i</i>    |
| <i>Table of Contents</i>   | <i>iii</i>  |
| <i>Acronyms</i>  | <i>viii</i> |
| <i>Acknowledgements</i>  | <i>xi</i>   |
| <i>List of Publications</i>  | <i>xii</i>  |
| <i>Abstract</i>  | <i>xv</i>   |
| <b>Table of Contents .....</b>   | <b>iii</b>  |
| <b>Acronyms .....</b>  | <b>vi</b>   |
| <b>Acknowledgements .....</b>  | <b>viii</b> |
| <b>List of Publications and Awards.....</b>  | <b>ix</b>   |
| <b>Abstract.....</b>   | <b>xi</b>   |
| <b>Chapter 1. Introduction.....</b>  | <b>1</b>    |
| 1.1 Background.....  | 1           |
| 1.1.1 Energy Harvesting Definition.....  | 1           |
| 1.1.2 Smart Grid & Wireless Sensors.....   | 2           |
| 1.2 A Review of Energy Harvesting in Smart Grid .....                                    | 5           |
| 1.2.1 Energy Sources in Power Distribution Systems .....                                 | 5           |
| 1.2.2 Cable-clamped Magnetic Field Energy Harvesting.....                                | 9           |
| 1.2.3 Free-standing Magnetic Field Energy Harvesting.....                                | 14          |
| 1.3 Motivation of the Work.....  | 20          |
| 1.4 Organisation of the Thesis .....   | 24          |
| 1.5 References.....  | 26          |
| <b>Chapter 2: System Overview of Free-standing Magnetic Field Energy Harvesting.....</b> | <b>32</b>   |

|  |           |
|--|-----------|
| 2.1 Introduction .....                                       | 32        |
| 2.2 Magnetic Field near High Voltage Equipment.....          | 33        |
| 2.2.1 Under Overhead Power Lines .....                       | 33        |
| 2.2.2 Inside Electrical Substations.....                     | 39        |
| 2.3 Overview of a Magnetic Field Energy Harvester .....      | 41        |
| 2.3.1 System Modelling.....                                  | 41        |
| 2.3.2 Effective Permeability and Demagnetization Factor..... | 43        |
| 2.3.3 Energy Losses in a Ferromagnetic Core.....             | 52        |
| 2.3.4 Circuit Design.....                                    | 54        |
| 2.4 Summary.....   | 57        |
| 2.5 References .....   | 59        |
| <b>Chapter 3: The Development of a Bow-tie Coil.....</b>     | <b>61</b> |
| 3.1 Introduction .....                                       | 61        |
| 3.2 The Design and Analysis of the Bow-tie Coil .....        | 63        |
| 3.2.1 Optimum Core Shape Design.....                         | 64        |
| 3.2.2 Core Material Selection.....                           | 71        |
| 3.2.3 Optimum Winding Method .....                           | 75        |
| 3.3 Measurement Results and Discussions .....                | 78        |
| 3.4 Summary.....   | 85        |
| 3.5 References .....   | 86        |
| <b>Chapter 4: The Development of a Helical Coil.....</b>     | <b>90</b> |
| 4.1 Introduction .....                                       | 90        |
| 4.2 The Design and Analysis of the Helical Coil.....         | 91        |
| 4.2.1 Optimum Core Shape Design.....                         | 91        |
| 4.2.2 Core Material Selection.....                           | 96        |

|   |            |
|---|------------|
| 4.3 Optimization of the Helical Coil.....                           | 100        |
| 4.3.1 The Pitch Angle $\alpha$ .....                                | 102        |
| 4.3.2 Helical Width $W_H$ and Inner Diameter $D_{in}$ .....         | 103        |
| 4.3.3 Core Thickness $M_C$ .....                                    | 104        |
| 4.4 Experimental Validations and Discussions .....                  | 106        |
| 4.6 Summary.....  | 112        |
| 4.7 References .....  | 113        |
| <b>Chapter 5. Matching Circuit and Energy Management Unit .....</b> | <b>116</b> |
| 5.1 Introduction .....  | 116        |
| 5.2 The Investigation of Input Impedance .....                      | 119        |
| 5.2.1 Rectifier Design.....   | 119        |
| 5.2.2 The Input Impedance of a Resistive Load .....                 | 121        |
| 5.2.3 The Input Impedance of a Charging Capacitor .....             | 123        |
| 5.3 Matching Circuit Design of a Charging Capacitor .....           | 134        |
| 5.4 Energy Management Unit.....                                     | 138        |
| 5.5 Experimental Results and Discussions .....                      | 140        |
| 5.5 Summary.....  | 144        |
| 5.6 References .....  | 145        |
| <b>Chapter 6. Future Work and Contributions .....</b>               | <b>149</b> |
| 6.1 Summary.....  | 149        |
| 6.2 Key Contributions.....  | 151        |
| 6.3 Future Work .....   | 153        |
| <b>Appendix.....</b>  | <b>154</b> |

## Acronyms

|               |   |
|---------------|---|
| <b>AC</b>     | Alternating Current                               |
| <b>ADC</b>    | Analog to Digital Converter                       |
| <b>ADS</b>    | Advanced Design System                            |
| <b>CST</b>    | Computer Simulation Technology                    |
| <b>CVR</b>    | Conservative Voltage Reduction                    |
| <b>DAC</b>    | Digital to Analog Converter                       |
| <b>DC</b>     | Direct Current                                    |
| <b>DCM</b>    | Discontinuous Condition Mode                      |
| <b>DTR</b>    | Dynamic Thermal Rating                            |
| <b>EMU</b>    | Energy Management Unit                            |
| <b>ESU</b>    | Energy Storage Unit                               |
| <b>EH</b>     | Energy Harvesting                                 |
| <b>EMF</b>    | Electric and Magnetic Field                       |
| <b>FeSiB</b>  | Ferrous, Silicon and Boron                        |
| <b>GSM</b>    | Global System for Mobile Communications           |
| <b>ID</b>     | Inner Diameter                                    |
| <b>MCU</b>    | Micro Controller Unit                             |
| <b>MnZn</b>   | Manganese and Zinc                                |
| <b>MOSFET</b> | Metal-Oxide-Semiconductor Field-Effect Transistor |
| <b>OD</b>     | Outer Diameter                                    |
| <b>PWM</b>    | Power Width Modulation                            |

|             |                        |
|-------------|------------------------|
| <b>RF</b>   | Radio Frequency        |
| <b>RMS</b>  | Root Mean Square       |
| <b>SW</b>   | Switch                 |
| <b>UVLO</b> | Under Voltage Lock-out |
| <b>2D</b>   | Two Dimensional        |
| <b>3D</b>   | Three Dimensional      |



## Acknowledgements

In my four years PhD studies, I am grateful to many people. First and foremost, I would like to express my sincere appreciation and thanks to my supervisor Professor Yi Huang. I thank you for giving me the opportunity to be one of your PhD students. I hope I have repaid the faith you shown in me several years ago. I learned so much from you both academically and personally. Thank you for the invaluable comments and advice on my research as well as my career development. I also would like to acknowledge Dr. Jiafeng Zhou for supporting my research and providing me with opportunities to be involved in the IET local network.

I would also like to thank my parents. Your continuous support and understanding have made my life full of love and I am grateful for everything you have done. I would also like to express my gratitude to my girlfriend. I would never have succeeded without her love, support, encouragement and patience.

Special thanks are also paid to my brilliant and lovely colleagues; in particular to Dr. Ping Cao, Dr. Jingwei Zhang, Dr. Qian Xu and Dr. Lei Xing as well as Chaoyun Song, Zhihao Tian, Zhouxiang Fei, Yaxing Ren and Amir Kotb, Anqi Chen, Yuan Zhuang, Muayad Kod, for many fruitful discussions and enjoyable moments.

Finally, the financial support from the Centre for Global Eco-Innovation and the Invisible-Systems Ltd is gratefully acknowledged. I would like to thank Pete Thompson and Martyn Gilbertson from the Invisible-Systems Ltd for providing me with different kinds of wireless sensors for experimental trials.

# List of Publications and Awards

## Journal Publications

- [1] **S. Yuan**, Y. Huang, Q. Xu, J. Zhou, C. Song and G. Yuan, “A highly efficient helical core for magnetic field energy harvesting”, *IEEE Transactions on Power Electronics*
- [2] **S. Yuan**, Y. Huang, Q. Xu, J. Zhou, C. Song and P. Thompson, “Magnetic Field Energy Harvesting Under Overhead Power lines”, *IEEE Transactions on Power Electronics*, Vol. 30, Issue 11, May, 2015.
- [3] C. Song, Y. Huang, P. Carter, J. Zhou, **S. Yuan**, Q. Xu and M. Kod, "A Novel Six-band Dual CP Rectenna Using Improved Impedance Matching Technique for Ambient RF Energy Harvesting", *IEEE Transaction on Antennas and Propagation*.,, pp. 1-1, 2016.
- [4] Q. Xu, Y. Huang, X. Lei and **S. Yuan**, “B-Scan in a Reverberation Chamber”, *IEEE Transaction on Antennas and Propagation*, Vol.64, Issue 5, Feb, 2016.
- [5] Q. Xu, Y. Huang, **S. Yuan**, X. Lei and Zhihao Tian, “Two Alternative methods to Measure the Radiated Emission in a Reverberation Chamber, *International Journal of Antennas and propagation*, Vol. 2016, Feb, 2016.
- [6] C. Song, Y. Huang, J. Zhou, J. Zhang, **S. Yuan** and P. Carter, “A High-Efficiency Broadband Rectenna for Ambient Wireless Energy Harvesting”, *IEEE Transaction on Antennas and Propagation*, Vol. 63, No. 8, August, 2015.

## Awards:

- [1] **S. Yuan**, Merit Award, “Singapore Challenge: The Science of Future Cities”, Singapore, September, 2015.
- [2] **S. Yuan**, Final Winner, “CWIEME Challenge: The Best University Project”, Berlin, May, 2015

- [3] **S. Yuan**, Winner, “IET Present Around the World in Lancashire Network”, Preston, April, 2015

## Abstract

Real-time data of power infrastructures collected by wireless sensors are the foundation of many smart grid applications. However, the finite life span of the batteries which power the wireless sensor becomes a bottleneck problem as it is expensive to periodically replace these batteries. Energy harvesting can be an effective solution for autonomous, self-powered wireless sensors. In the vicinity of high voltage/current equipment, a strong magnetic field is generated, which could be a consistent energy source. The purpose of this thesis is to present a comprehensive study into a magnetic field energy harvesting system which mainly consists of coil and rectifying circuit with the ultimate goal to obtain the maximum energy as efficiently as possible for a given condition. The main contribution of this thesis is in two research areas:

The first area is about the design of an energy harvesting coil. The ferromagnetic core is the most important part to determine the output power from the whole energy harvesting system. Thus, the precise knowledge of ferromagnetism is critical. As the harvesting coil may not fully enclosure the current conductor, the demagnetization factor which is closely related to the core geometry is carefully studied and minimized. Two new core shapes have been proposed and optimized to have much lower demagnetization factors (hence more power) than that of a conventional rod.

1. A bow-tie-shaped core is introduced and designed to have two large end surfaces. By making its two ends broader, more magnetic flux can be guided from the air into the ferromagnetic core. This intensifies the magnetization at the middle of the core where the wire is wound on.
2. A new helical core is introduced as a further improved version of the bow-tie core. It utilizes two big circular plates fitted at the both ends for the flux collection. In the middle, a helical-shaped core is introduced to increase the path of the magnetic flux. Therefore, the separation between the north pole and south pole is lengthened dramatically, which leads to a reduction in the demagnetization factor and an increase in the magnetic flux density.

In addition to the core shape, the selection of the core material is studied and found

that high permeability ferrite is the most suitable core material due to its high relative permeability and ultra-low conductivity. Thus, the eddy current losses in the ferromagnetic core can be significantly reduced. Experimental results show that the proposed helical coil with only 400 turns of wire can have a power density of  $2.1 \mu\text{W}/\text{cm}^3$  when placed in a magnetic flux density of  $7 \mu\text{T}_{\text{rms}}$ . This value is 17 times greater than a previously reported design with 40,000 turns of wire ( $0.12 \mu\text{W}/\text{cm}^3$ ) placed in the same magnetic field. If a longer helical coil with 8,000 turns of wire is placed in a magnetic flux density of  $11 \mu\text{T}_{\text{rms}}$ , the produced power density is around  $131.4 \mu\text{W}/\text{cm}^3$  which is comparable to a solar panel working during a cloudy day.

The second area is about the rectifying circuit design which utilizes the energy harvested from the coil to power a commercial wireless sensor. A voltage doubler is applied to provide full-wave rectification and simultaneously boost the output voltage. A transient analysis is carried out to calculate the input resistance of a charging capacitor as a function of time. The theoretical analysis indicates that the input resistance is highly related to the input and output voltages. Therefore, a conventional matching network which consists of linear components cannot work well. A switch mode power converter is introduced as a matching network so that the charging capacitor can be isolated from the harvesting coil. The emulated input resistance looking into the power converter is a constant and determined by the frequency and the duty cycle of the power width modulation applied on the switch. The system is designed and made. The experimental results demonstrate that the energy conversion efficiency from the harvesting coil to the storage capacitor is around 74.6% which is twice as large as a previously reported design. Finally, an energy management unit is developed and it effectively utilizes the energy stored in the capacitor to power a commercial wireless sensor.

It is shown in this thesis that a highly efficient magnetic field energy harvesting system has been successfully demonstrated. A wireless sensor can be properly powered up by using a small coil (15 cm long) placed in a small magnetic flux density ( $7 \mu\text{T}_{\text{rms}}$ ). The proposed solution is a very efficient and attractive method for harvesting the magnetic field energy for a wide range of smart grid applications.

## Chapter 1. Introduction

### 1.1 Background

#### 1.1.1 Energy Harvesting Definition

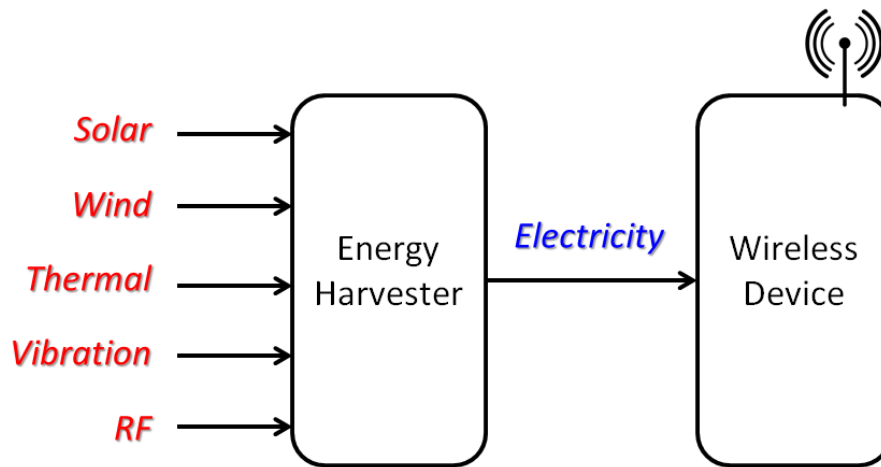


Fig. 1.1 An energy harvester powered wireless sensor

Energy Harvesting (EH), also known as energy scavenging, is a process in which energy is captured from the ambient environment (such as solar, wind, vibration, thermal, electromagnetic wave, etc.) and then converted into useable electric energy as shown in Fig. 1.1. Energy harvesters could be utilized to replace batteries for electronic devices with low power consumption. The advantages of EH are listed as follows [1-3]:

1. **Maintenance free:** If a wireless device can be totally self-powered, there is no need to replace the battery periodically. Therefore, the wireless sensor can be deployed at hard-to-reach places such as remote rural areas and inside the human body.
2. **Environmentally friendly:** Batteries usually contain chemicals and metals that are harmful to the environment and human health. By applying EH technologies, massive wireless sensors can be battery-free which is friendly to the environment.

A typical block diagram of an energy harvesting system is shown in Fig.1.2. It normally consists of an energy harvester, a rectifier (if necessary), an energy storage unit (e.g. rechargeable batteries and super-capacitors) and an energy management system (also known as battery management system).

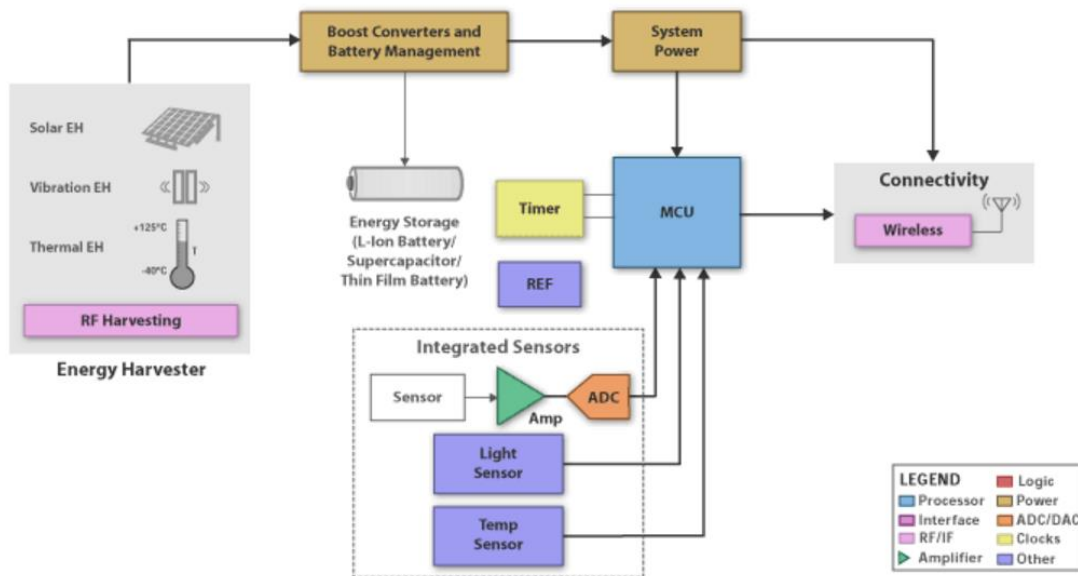


Fig. 1.2 A typical energy harvesting system [4].

## 1.1.2 Smart Grid & Wireless Sensors

Due to global urbanization and the rapid development of mega cities, it is expected that the demand for electric energy will continue to increase in the following decades [5]. It is also a big challenge to deliver this huge energy from power plants to end customers, as some existing overhead power lines may reach to their thermal limitations [6]. Furthermore, the increasing load on high voltage equipment could accelerate the deterioration of the insulation [7]. Especially for old equipment, it is more likely to breakdown due the aging effect and the heavy load. To deal with these problems and pressures, three key smart grid functions are being developed [8]:

**Delivery Optimization** could improve the transmission capacity of the power delivery system. The thermal limitation of overhead lines can be increased by applying the Dynamic Thermal Rating (DTR) technique [6, 9-12]. Based on the real-time data from local weather stations as shown in Fig. 1.3 (such as wind speed, air temperature, humidity, solar radiation,

etc.), cooling effects on overhead lines can be estimated to dynamically adjust thermal limitations. It is estimated that the transmission capacity of overhead lines could be increased by 5% to 15% if a proper DTR technique can be applied [12].



**Fig. 1.3 Weather stations placed under overhead power lines [13]**

**Demand Optimization** focuses on solutions to reduce peak demand and achieve energy savings. Conservation Voltage Reduction (CVR) is a typical demand response technology [14-15]. By lowering voltages on the power distribution system in a controlled manner, CVR can reduce the peak demand and achieve energy savings while keeps the lowest utilization voltage consistent with levels determined by regulatory agencies and standards-setting organizations [16]. The communications between substations for control and monitoring the voltage of transformers and load profiles play a critical role in CVR [14]. The smart meters shown in Fig. 1.4 are used to measure these real-time data.



**Fig. 1.4 Smart meters installed inside substations to measure the power profile [17-18]**



**Asset Optimization** is the application of monitoring and diagnostic technologies to reduce the maintenance costs of old electrical infrastructures, detect the potential problems in the early stage and extend their lifetime [10, 19-20]. This can be achieved by deploying condition monitoring sensors (such as partial discharge sensors and infrared detectors shown in Fig 1.5) to generators, transformers, switch gears, power cables, etc.





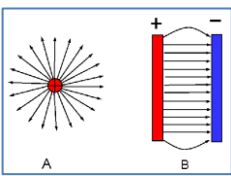
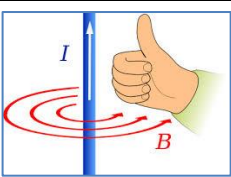
**Fig. 1.5 Condition monitoring sensors in substations. (a). Partial discharge sensor. (b) Infrared detector [21-22]**

It is important to note that all the technologies discussed above are only feasible if reliable real-time data from power infrastructures can be continuously collected and processed. Wireless sensors are considered as favorable tools for collecting these data because of their low power consumptions, rapid deployments and low costs [23]. **However, the finite life span of the batteries which power the wireless sensor becomes a bottleneck as it is expensive to periodically replace these batteries especially when sensors are deployed in the remote area. Thus, the energy harvesting technology is an attractive and promising solution to make wireless sensors self-sustainable.**

## 1.2 A Review of Energy Harvesting in Smart Grid

### 1.2.1 Energy Sources in Power Distribution Systems

Table 1.1 The comparison of different energy harvesting techniques near power infrastructures

| Energy sources  |                       | Advantages  | Disadvantages  |
|---|-----------------------|---|--|
|    | <b>Solar energy</b>   | High power density in a good weather condition        | 1. Power not stable<br>2. Need storage unit<br>3. Outdoor only     |
|   | <b>Wind energy</b>    | High power density in a good weather condition        | 1. Power not stable<br>2. High maintenance cost<br>3. Outdoor only |
|  | <b>Electric field</b> | Energy available when close to high voltage equipment | Low energy conversion efficiency due to the huge reactance         |
|  | <b>Magnetic field</b> | Energy available near a current conductor             | Energy losses inside the ferromagnetic core                        |

As shown in Table 1.1, there are several ambient energy sources (solar, wind, electrical field, magnetic field, etc.) available in electrical substations or under electricity pylons. Solar panels are a good option to collect energy during daytime in good weather conditions [24-25]. However, a solar energy device heavily relies on weather conditions and may require additional high-capacity energy storage units which are normally expensive in order to work at night [26-27]. Similar situations apply to the small wind turbine. Furthermore, harsh weather conditions like hail and storms could damage the turbine blades and solar panels [26, 28]. In the vicinity of high voltage equipment (such as transformers, power cables, switch gears, etc.), strong electromagnetic fields are generated. According to the data from the UK National Grid [29], the averaged electrical field and magnetic field inside a typical substation are around 10 kV/m and 32 A/m respectively. Therefore, the electric and magnetic field could

be consistent and reliable energy sources for wireless sensors deployed near the high voltage equipment.

The electric field is caused by the voltage of high power equipment (electric charges). Therefore, the electric field energy around the power equipment is stable regardless of the load demand. Even when there is no current inside the equipment, the electric field energy harvester can still work properly. The electric field energy can be harvested by two parallel plates acting as a coupling capacitor. The load is connected to this capacitor in parallel. Fig. 1.6 shows the equivalent circuit of an electric field energy harvester attached to an overhead line [30].

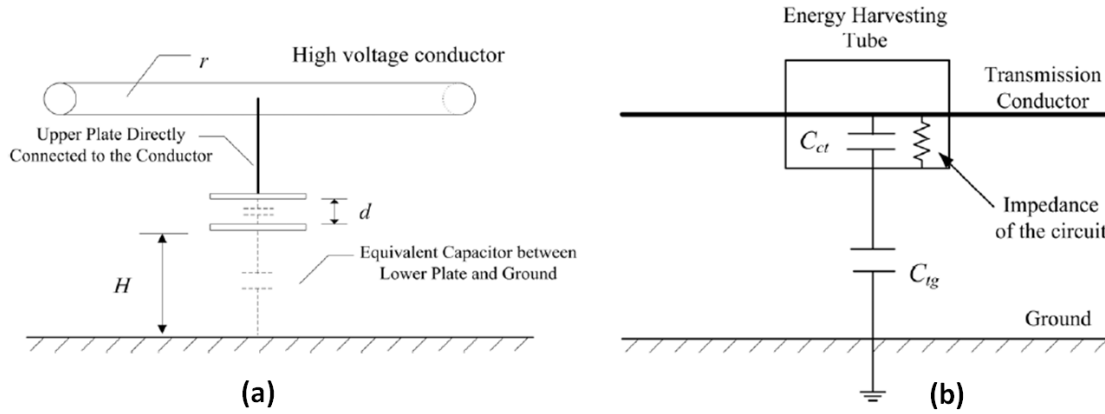


**Fig. 1.6 (a) the work principle of an electric field energy harvester attached to an overhead power line; (b) the equivalent circuit [30]**

There are several published papers about an electric field energy harvester attached to the high voltage power cable [30 - 36]. For different testing conditions, the power harvested varies significantly. In Table 1.2, only the work verified by experiment has been listed and compared. From [31, 32], when an electric field energy harvester is fully enclosure on a conductor with a very high voltage ( $\geq 100$  kV), more than 200 mW can be harvested which may be sufficient for the continuous operation of a measurement system with a GSM module [32]. However, when the voltage of the conductor is in the power distribution-level ( $\leq 33$  kV), the power collected is significantly reduced to several milliwatts or even smaller as the harvested power is proportional to the voltage squared [31, 33]. Besides, as indicated in Table 1.2, the size of a cylindrical capacitor is relatively big ( $\geq 35 \times 10^3 \text{ cm}^3$ ). In [34, 35], a free-standing capacitor was designed with two parallel plates which could be directly attached to a

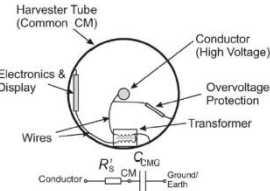
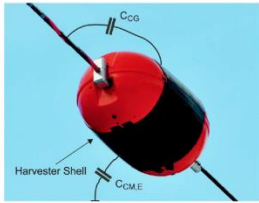
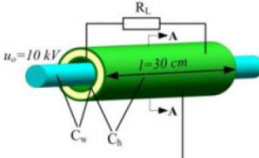
power cable or placed inside an electrical substation. Nevertheless, the power harvested is quite small for a free-standing capacitor especially when it is placed several meters away from the high voltage device [35]. For all the electric field energy harvesters, the power is limited due to the huge reactance of the coupling capacitor [34, 35]. The capacitance of a typical electric field energy harvester is in the magnitude of pF. As the power frequency is extremely low (50/60 Hz), the resonant inductance required is in the order of MH which is very difficult to obtain in practice. Therefore, the energy conversion efficiency of the electric field energy harvesting system is relatively low due to the unmatched load.

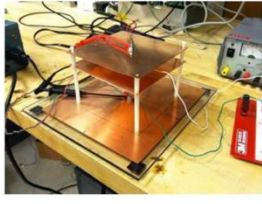
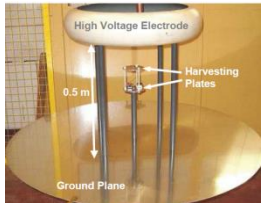
$$L_r = \frac{1}{\omega^2 C_{EH}} \quad (1.1)$$

where  $L_r$  is the resonant inductance in H,  $\omega$  is the angular frequency in rad/s and  $C_{EH}$  is the capacitance of the electric field energy harvester in F.

As a consequence, the electric field energy harvester is only applicable when it is directly attached or clamped on a conductor with a very high voltage ( $\geq 100$  kV).

**Table 1.2 The summary of electric field energy harvesters**

| Ref. | The Figure of Energy Harvester  | Size and Structure   | Testing Conditions                                      | Power Collected                       |
|------|---|--|---|---------------------------------------|
| [31] |  | A cylindrical capacitor with a diameter of 30 cm and a length of 55 cm | A). 50 kV cable<br>B). 100 kV cable<br>C). 150 kV cable | A). 45 mW<br>B). 200 mW<br>C). 370 mW |
| [32] |  | A cylindrical capacitor with an unknown size                           | 153 kV power cable in laboratory                        | Power a GSM unit (>350 mW)            |
| [33] |  | A cylindrical tube with a length of 30 cm and a diameter of 40 cm      | 10 kV power line  | 663 $\mu$ W                           |

|      |   |  |  |                       |
|------|---|--|--|-----------------------|
| [34] |  | Two parallel plates with a dimension of 15 cm x 15 cm and a separation of 2.4 cm | Attached to:<br>A). 20 kV cable<br>B). 35 kV cable             | A). 7 mW<br>B). 17 mW |
| [35] |  | Two parallel plates with a volume of $3.14 \times 10^3 \text{ cm}^3$             | Inside a 400 kV substation where the electric field is 5.8 V/m | 176 $\mu\text{W}$     |

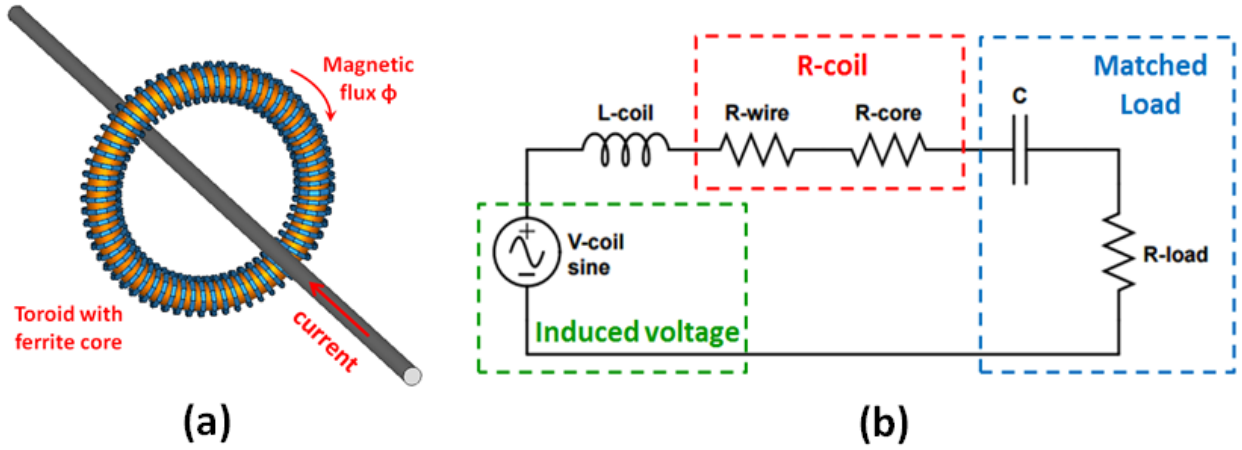


**Fig. 1.7 (a) a cable-clamped magnetic field energy harvester mounted on a power line, (b) the equivalent circuit of a magnetic field energy harvester**

The magnetic field is generated from the current inside power equipment. Fig. 1.7 shows a magnetic field energy harvester clamped on a power cable and its equivalent circuit. According to Faraday's Law, when a coil is placed inside a time varying magnetic field, the voltage can be induced and calculated by:

$$V_{coil} = NA \frac{dB_{core}}{dt} \quad (1.2)$$

where  $V_{coil}$  is the open circuit voltage of the coil,  $N$  is the number of turns wound on the coil,  $B_{core}$  is the magnetic flux density inside the coil in T,  $A$  represents the effective cross section of the coil in  $\text{m}^2$ . By using a ferromagnetic core, the magnetic flux density  $B_{core}$  can be increased as indicated in Equation (1.3).

$$B_{core} = \mu_{eff}\mu_0 H_{ex} \quad (1.3)$$

where  $H_{ex}$  is the magnetic field generated by the current in power equipment in A/m,  $\mu_0$  is the permeability of the free space and the  $\mu_{eff}$  is the effective permeability related to the core material and core geometry. For a typical toroid with a high  $\mu$  ferrite core, the effective permeability  $\mu_{eff}$  can be as large as 18,000 [37]. As a result, compared to the electric field energy harvesting, the magnetic field energy harvesting could be much more efficient when the field strength is relatively small. There are two types of magnetic field energy harvesters with different setups: the cable-clamped energy harvester and the free-standing energy harvester.

## 1.2.2 Cable-clamped Magnetic Field Energy Harvesting

The cable-clamped magnetic field energy harvester is usually mounted on a power cable or an overhead power line as shown in Fig. 1.8 to power the sensors which measure the line current, the cable temperature, the overhead line sage, etc.

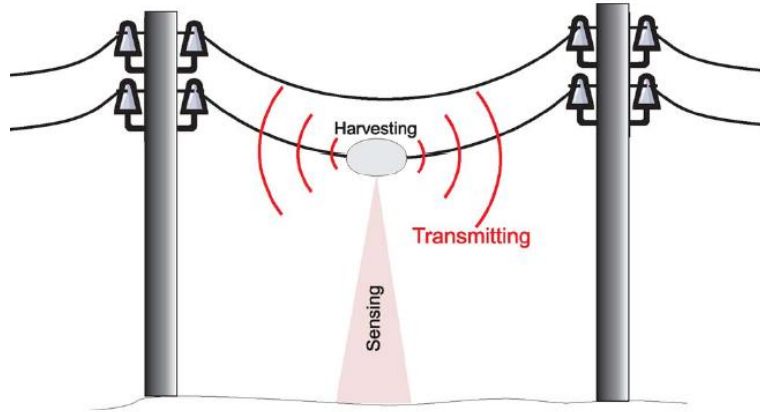


**Fig. 1.8 A cable-clamped energy harvester mounted on an overhead line to measure the line sag [31]**

As the harvesting coil can fully enclose the current conductor, the magnetic flux travels in the same medium. Thus, the effective permeability  $\mu_{eff}$  in Equation (1.3) is equal to the relative permeability  $\mu_r$  of the core material. Therefore, the magnetic flux density  $B_{core}$  in the core can be significantly increased by using a high  $\mu_r$  material, which leads to large output power. In Table 1.3, some typical ferromagnetic materials are concluded in terms of the relative

permeability  $\mu_r$ , resistivity  $R$  and the saturation magnetic flux density  $B_{sat}$ . For the core material with extremely high permeability ( $\mu_r \geq 10,000$ ), the flux density inside the core can easily become saturated when there is a small magnetic field applied. Thus, the output power of the cable-clamped energy harvester is normally limited by the core saturation. Besides, due to the nonlinear problem caused by the saturation in the ferromagnetic material, the whole system becomes much more complicated to determine the coil voltage, coil inductance, core losses, etc.

**Table 1.3 Typical ferromagnetic materials**

| Ref  | Material        | $\mu_r$   | $R$ ( $\mu\Omega\text{cm}$ ) | $B_{sat}$ (T) | Manufactory |
|------|-----------------|-----------|------------------------------|---------------|-------------|
| [38] | Metglas 2714A   | 1,000,000 | 142                          | 0.57          | Metglas     |
| [39] | Nanocrystalline | 80,000    | 130                          | 1.25          | Wiltan      |
| [40] | Permally 80     | 75,000    | 58                           | 0.75          | ESPI        |
| [41] | Mu-metal 1J85   | 60,000    | 55                           | 1.55          | MingShang   |
| [42] | Ferrite R15K    | 15,000    | $5 \times 10^6$              | 0.36          | DMEGC       |
| [43] | Ferrite 3E5     | 10,000    | $5 \times 10^7$              | 0.38          | Ferroxcube  |

In [44], an investigation was conducted to identify which core material was the most suitable for a cable-clamped energy harvester. As depicted in Fig. 1.10, they selected three toroid coils with different materials (ferrite, iron powder and nanocrystalline alloy) to clamp on the same current conductor. From the experimental results, they concluded the nanocrystalline alloy was the best material due to its high permeability and high saturation flux density. They used a cylindrical core with the outer diameter  $OD$  of 33.5 mm, inner diameter  $ID$  of 27.5 mm and the height  $H$  of 4 mm. 9 mW can be collected when it is mounted on a 5 A conductor which gives a power density of  $7.8 \mu\text{W}/\text{cm}^3$ . However, all of their results are based on the experiment and no theoretical analysis has been conducted to discuss the saturation problem in the ferromagnetic core.



Fig. 1.10 Three toroid coils with different core materials

Roscoe *et al* [45] used cylindrical ferrite cores ( $OD = 22$  mm,  $ID = 17$  mm,  $H = 6$  mm) to clamp on a conductor which carries a current of 50 A at 50 Hz. 170 mW can be collected which gives a power density of  $92.4 \mu\text{W}/\text{cm}^3$ . They selected the ferrite material with low relative permeability ( $\mu_r = 2000$ ) to avoid the magnetic flux saturation. However, as shown in Fig. 1.11, when the current becomes bigger, the ferrite core still comes saturated and leads to significant energy losses.

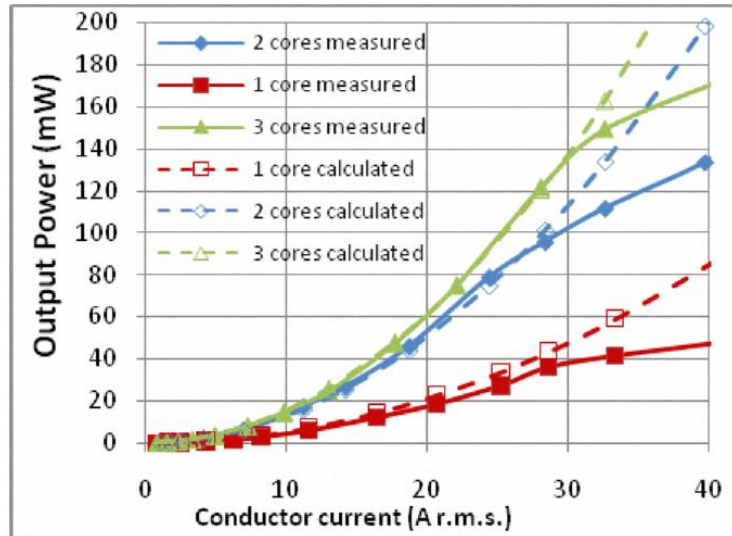


Fig. 1.11 The output power as a function of the conductor current [45]

Moon *et al* [46-49] used a time-varying inductor to model the saturation of the flux density in a ferromagnetic core. Therefore, the whole system became a purely circuit-based problem. For a typical inductor, its value is defined by:

$$L_{core} = N \frac{d\phi}{dI} \quad (1.4)$$



where  $L_{core}$  is the coil inductance,  $N$  is the number of turns,  $\varphi$  is the magnetic flux in the core and  $I$  is the current passing through the inductor. For a 60 Hz AC current, the waveform of a time-varying inductance in one clock cycle is shown in Fig. 1.12 [46].

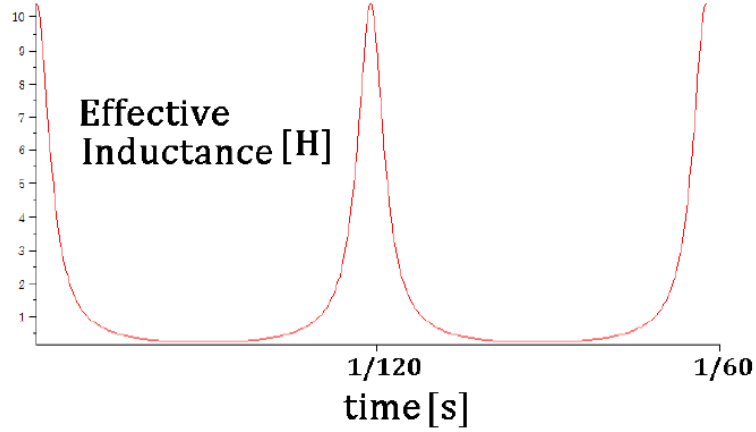


**Fig. 1.12 A time-varying inductance [46]**

When the current  $I$  is small, the magnetic field generated is small and the ferromagnetic core is far away from the saturation. In this case, the magnetic flux  $\varphi$  is linearly proportional to the current and the coil has a high value of inductance. When the current becomes bigger, the magnetic field increases correspondingly and the ferromagnetic core becomes saturated. In this situation, the magnetic flux keeps unchanged in regardless of the current and the effective coil inductance approaches to zero. Based on this circuit model, they developed an analytical expression to calculate the output power from the harvesting coil with a saturated core. From their experimental results, a toroid with a nanocrystalline core ( $OD = 24.5$  mm,  $ID = 16.5$  mm,  $H = 9$  mm) was mounted on a conductor with a current of 11.89 A. 78.6 mW was harvested which gave a power density of  $33.9 \mu\text{W}/\text{cm}^3$ .

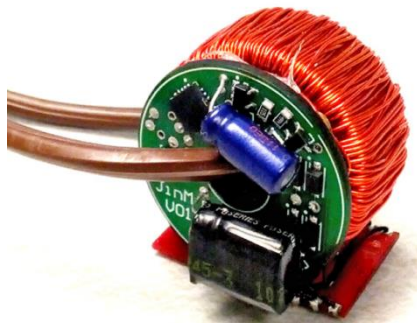


**Fig. 1.13 A toroid core clamped on a current conductor [46]**

To prevent the ferromagnetic core from the saturation, an air gap can be introduced to the toroid core as shown in Fig. 1.14. The magnetic flux travels through two different mediums and boundary conditions need to be applied. As a result, the flux density in the core may be dramatically reduced compared to an unbroken toroid core, which prevents the core from the saturation.

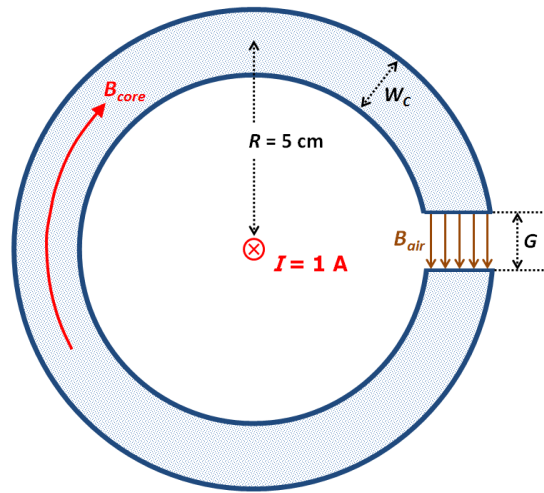


Fig. 1.14 A toroid core with an air gap [50]

In [50], a cylindrical core ( $OD = 16.3$  mm,  $ID = 14.4$  mm,  $H = 50$  mm) with an air gap is designed to clamp on a current conductor. Mu-metal is selected as the core material due to its high permeability. The air gap prevented the ferromagnetic core from the saturation so that the magnetic flux density in the core is linearly proportional to the current in the conductor. According to the experimental results, 14.36 mW was collected when the current was around 13.5 A, which produced a power density of  $6.37 \mu\text{W}/\text{cm}^3$ .

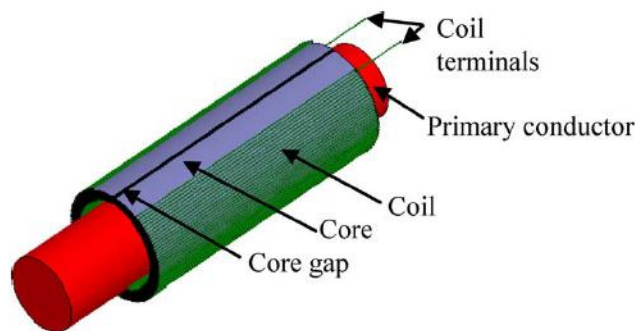


Fig. 1.15 A cylindrical core with an air gap mounted on a conductor [50]

In summary, although the output power from the cable-clamped magnetic field energy harvester is limited by the saturation in the ferromagnetic core, it still has several advantages compared to the electric field energy harvester.

1. The size of a toroid core is much smaller compared to a typical electric field energy harvester as illustrated in Table 1.2.
2. The typical inductance of a toroid coil is in the order of H or mH. At 50/60 Hz, its resonant capacitance is in the magnitude of nF or mF which is widely available on the market. Thus, a properly matching circuit can be designed to convert the magnetic field energy into a useable electrical energy efficiently. This is impractical for an electric field energy harvester due to its small capacitance.
3. By using a ferromagnetic core, the magnetic flux passing through the coil can be significantly increased. Therefore, the cable-clamped magnetic field energy harvester is able to collect plenty of energy ( $\geq 100$  mW) even when the current is only around 10 to 20 A [45-50]. As a consequence, this system can be applied to the high voltage power transmission system ( $\geq 33$  kV) as well as the domestic power system (230/110 V)

### **1.2.3 Free-standing Magnetic Field Energy Harvesting**

A cable-clamped magnetic field energy harvester is able to collect magnetic field energy efficiently. However, it has some limitations and inconvenience as it has to clamp on a current conductor.

1. For a high voltage power system, the power cable needs to be de-energized to allow the proper installation and maintenance.
2. When a cable-clamped energy harvester along with a sensor is mounted on an overhead power line, the weight of the system will increase the line sag and cause safety issues.
3. It is difficult to install a cable-clamped device on a big power transformer.

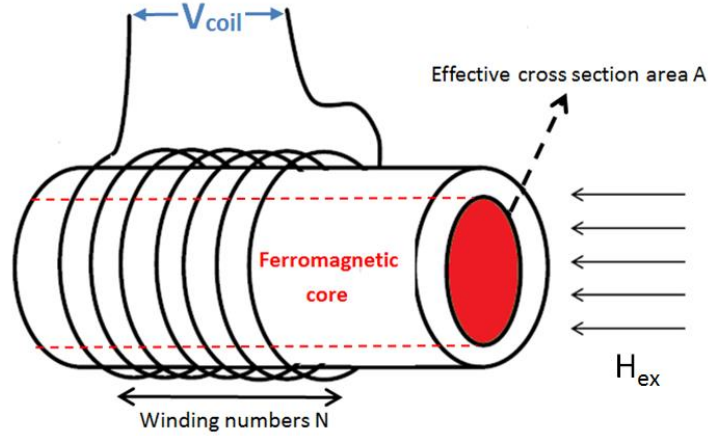


**Fig. 1.16 A typical free-standing magnetic field energy harvester**

A typical free-standing energy harvester shown in Fig. 1.16 can overcome these shortcomings. Unlike the cable-clamped one, this energy harvester can be installed in any places as long as there is an alternating magnetic field. Due to the great flexibility, the harvesting coil is capable of powering various sensors for different purposes. For example, partial discharge sensors can be powered to monitor the conditions of transformers in electrical substations. Thus, the potential problems can be detected in the early stage. Weather stations under overhead lines can be powered to collect the real-time weather data which are critical to dynamic thermal rating techniques.

The basic working principle of a free-standing energy harvester is similar to a cable-clamped one. As depicted in Fig. 1.16, when a coil is subjected into a time-varying magnetic field, voltage can be induced.

$$V_{coil} = N\omega A\mu_{eff}\mu_0 H_{ex} \quad (1.5)$$

where  $V_{coil}$  is the induced coil voltage,  $N$  is the number of turns wound on the coil,  $\omega$  is the angular frequency in rad/s,  $A$  represents the effective cross section of the coil in  $m^2$ ,  $\mu_{eff}$  is the effective permeability related to the core material and core geometry,  $H_{ex}$  is the magnetic field in A/m generated by the current conductor.

The main difference is a free-standing coil cannot fully enclose the current conductor. When a ferromagnetic rod with a finite length is magnetized, the demagnetization phenomenon appears and the magnetic flux density in the core is dramatically reduced. In other words, if a rod and a toroid core with the same material are placed in the same magnetic field  $H_{ex}$  shown

in Fig. 1.17, the flux density  $B_{rod}$  in the rod is much smaller than that of the toroid core  $B_{toroid}$ . More theoretical analysis regarding to the demagnetization will be discussed in Chapter 2. The power output from a free-standing coil is greatly limited compared to a cable-clamped energy harvester. As a consequence, the free-standing magnetic field energy harvester has to be finely optimized to maximize the output power.

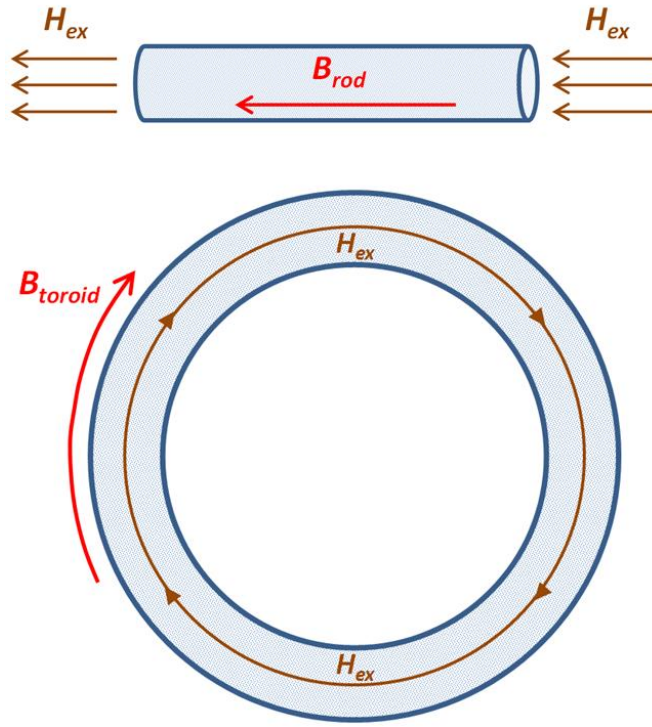


**Fig. 1.17** A rod and a toroid core placed in the same magnetic field  $H_{ex}$

In 2011, Tashiro *et al* used Brooks coils to harvest the magnetic energy from the power line as shown in Fig 1.18 [51]. From their experimental results, 6.32 mW could be collected by using an air-core coil with 18,395 turns placed in a magnetic flux density of 21.2  $\mu\text{T}_{rms}$  at 60 Hz. This gives a power density of 1.47  $\mu\text{W}/\text{cm}^3$ . It is concluded that by applying the ferromagnetic core, the output power from the coil is not significantly increased. This is not true as they have not carried out an in-depth research into the magnetization of the ferromagnetic material. The core shape should be optimized to increase the effective permeability and the suitable material needs to be identified to reduce the core losses. As a consequence, the output power density of this design is quite small.

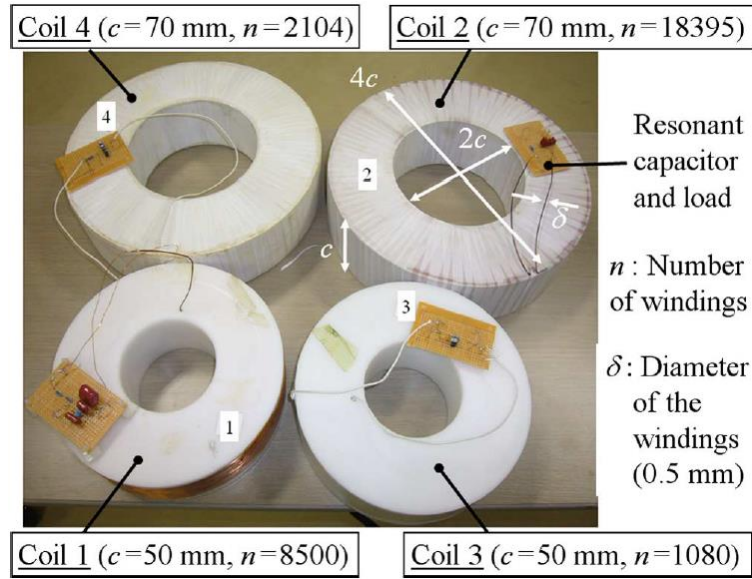


**Fig. 1.18. The testing coils in [51]**

In 2012, Roscoe *et al* developed a free-standing energy harvesting system to collect the magnetic field energy in an electrical substation [52-53]. Besides, a voltage doubler and an energy management unit were designed to convert the alternating magnetic field energy into the DC electrical energy. Finally, a small wireless sensor shown in Fig. 1.19 could be powered up in every 4 minutes to transmit the temperature reading to the receiver [54].

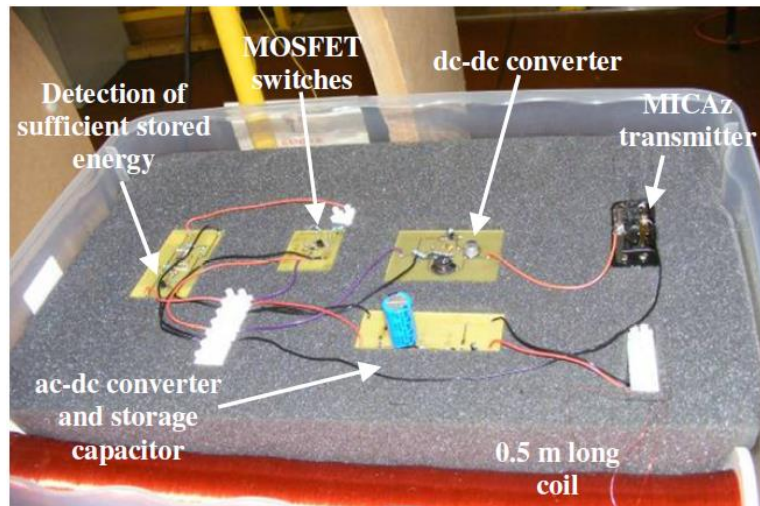


**Fig. 1.19 The magnetic field energy harvesting system in [52]**

In [52], it was suggested that a coil with a long and thin ferromagnetic core could increase the effective permeability and produce a higher power output. Therefore, a solenoid with a length

of 50 cm and a diameter of 5 cm has been designed. 833  $\mu\text{W}$  could be collected by placing the long solenoid with 40,000 turns in a magnetic flux density of  $18 \mu\text{T}_{rms}$  at 50 Hz. This gave a power density of  $0.845 \mu\text{W}/\text{cm}^3$ . The performance of their design is not significantly better than the results demonstrated in [51]. The main reason is that the cast iron is selected as the core material which suffered greatly from the eddy current losses. Therefore, a suitable ferromagnetic material should be identified by compromising the high permeability and low core losses. Besides, the core shape may be further optimized as the long rod occupies too much space because of its length.

On the circuit side, a voltage doubler is proposed to convert the AC power to a DC one and simultaneously boosting the output voltage. However, they have not designed a proper matching circuit to convert the energy from the coil into the load efficiently. Instead, only a compensating capacitor was added to eliminate the coil inductance. However, an extra matching network should be developed to match the input resistance to the coil resistance so that maximum energy can be transferred from the coil to the load. As a result, a more advanced circuit design is required.

In conclusion, the free-standing magnetic field energy harvester has its own advantages compared to the cable-clamped one:

1. The free-standing energy harvester can work in any places as long as there is an alternating magnetic field. Hence, it can be used to power various sensors, which is impractical for a cable-clamped one.
2. It is more convenient and safe to install and maintain a free-standing energy harvester as it is not directly attached to a high voltage equipment.

However, as the free-standing coil cannot fully enclosure the current conductor, the demagnetization phenomenon appears during the magnetization process, which leads to a reduction of the output power. According to the literature, only two groups have conducted the relevant research in this area and provided some experimental results. Nevertheless, both of their designs have some key limitations and the produced power density is relatively small. Therefore, a comprehensive study on the free-standing magnetic field energy harvesting system is required to optimize the output power in terms of the core shape, core material and

the relevant circuit design.



## 1.3 Motivation of the Work



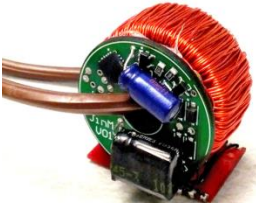
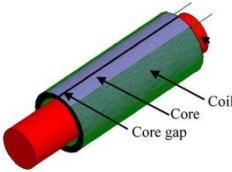
In recent years, a lot of ideas and applications related to the smart grid have been proposed, tested and implemented. Real-time data collected by wireless sensors are critical for all smart grid applications. However, the finite life span of the batteries which power the sensing system becomes a bottleneck as it is expensive to periodically replace these batteries. Thus, the energy harvesting technology is an attractive and promising solution to make the monitoring system self-sustainable. There are several ambient energy sources (solar, wind, electromagnetic, etc.) in electrical substations or under electricity pylons. Solar panels are a good option to collect energy during daytime in good weather conditions [24-25]. This technology is relatively mature and many products are already available on the market. However, a solar energy device heavily relies on weather conditions and may require additional high-capacity energy storage units which are normally expensive in order to work at night [26-27]. Similar situations apply to the small wind turbine. Furthermore, harsh weather conditions like hail and storms could damage the turbine blades and solar panels [26, 28].

In the vicinity of high voltage equipment, a strong electromagnetic field is generated, which could be a consistent energy source for wireless sensors. The electric field energy is always available as long as the high voltage equipment is turned on. However, it is very difficult to design a good matching circuit as the reactance of the electric field energy harvester (coupling capacitor) is extremely high. Therefore, the output power is greatly limited due to the low energy conversion efficiency. As summarized in Table 1.2, the electric field energy harvester is only applicable when it is directly attached or clamped on a conductor with a very high voltage ( $\geq 100$  kV).

The magnetic field strength is directly related to the current in the power equipment. An inductive coil can be applied to harvest the magnetic field energy. By using the ferromagnetic material, the magnetic flux passing through the coil can be increased significantly. Besides, it is much easier to find a resonant capacitor to compensate the high reactance of the inductive coil at 50/60 Hz. As a result, the magnetic field energy harvester is able to collect much more energy compare to the electric field energy harvester especially when the field strength is relatively small.

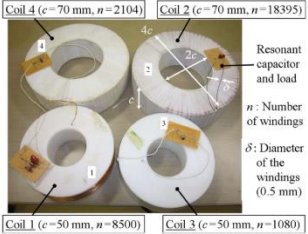
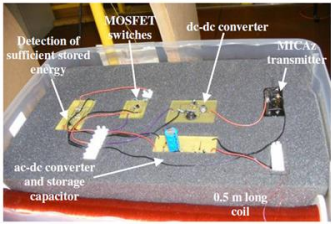
There are two types of magnetic field energy harvesters working for different purposes. The first one is the cable-clamped energy harvester shown in Fig. 1.8. It is mainly used to power the sensors which measure the line current and the cable temperature. As the ferromagnetic core can fully enclose the current conductor, the magnetic flux travels in the same medium so that the output power from the coil is relatively big. There are several published results [45-50] focused on cable-clamped energy harvesters which are mounted on power cables or overhead lines. Their designs are summarized in Table 1.4 in terms of the physical size, testing conditions and the output power. It is noted that the size of these cable-clamped energy harvesters are much smaller than the typical electric field energy harvesters illustrated in Table 1.2. According to their experimental results or predications, more than 100 mW can be collected when their coils are clamped on the conductors carrying a current of 50 A.

**Table 1.4 Summary of the cable-clamped magnetic field energy harvester**

| Ref.    | The Figure of Energy Harvester  | Size and Structure  | Testing Conditions               | Power ( $P$ ) and Power density ( $S$ )                              |
|---------|---|---|----------------------------------|--|
| [44]    |  | A cylindrical core with outer $D$ of 33.5 mm, inner $D$ of 27.5 mm and $H$ of 4 mm  | $I = 5\text{ A}$<br>at 60 Hz     | $P = 9\text{ mW}$ ;<br>$S = 7.8\text{ }\mu\text{W}/\text{cm}^3$      |
| [45]    |  | Two identical cores with outer $D$ of 22 mm, inner $D$ of 17 mm and $H$ of 6 mm     | $I = 50\text{ A}$<br>at 50 Hz    | $P = 170\text{ mW}$ ;<br>$S = 92.4\text{ }\mu\text{W}/\text{cm}^3$   |
| [46-49] |  | A cylindrical core with outer $D$ of 24.5 mm, inner $D$ of 16.5 mm and $H$ of 9 mm  | $I = 11.89\text{ A}$<br>at 60 Hz | $P = 78.6\text{ mW}$ ;<br>$S = 33.9\text{ }\mu\text{W}/\text{cm}^3$  |
| [50]    |  | A cylindrical core with outer $D$ of 16.3 mm, inner $D$ of 14.4 mm and $H$ of 50 mm | $I = 13.5\text{ A}$<br>at 60 Hz  | $P = 14.36\text{ mW}$ ;<br>$S = 6.37\text{ }\mu\text{W}/\text{cm}^3$ |

The second one is the free-standing energy harvester as shown in Fig. 1.16. Unlike the cable-clamped one, this energy harvester can be installed in almost any place as long as there is an alternating magnetic field. Due to the great flexibility, this kind of energy harvester is capable of powering various sensors for different purposes. For example, partial discharge sensors can be powered to monitor the conditions of transformers in electrical substations. Weather stations under overhead lines can be powered to collect the real-time weather data. These applications are impractical for a conventional cable-clamped energy harvester. Since the free-standing coil cannot fully enclose the current conductor, the demagnetization phenomenon appears during the magnetization process, which decreases the magnetic flux in the ferromagnetic core. The output power of a free-standing energy harvester is smaller compared to a cable-clamped one if both of them are tested under the same conditions. Therefore, the free-standing energy harvester has to be finely optimized to increase the output power.

**Table 1.5 Summary of the free-standing magnetic field energy harvester**

| Ref.    | The Figure of Energy Harvester  | Size and Structure   | Testing Conditions                      | Power ( $P$ ) and Power density ( $S$ )                       |
|---------|---|--|---|---|
| [51]    |  | A Brooks coil with an outer radius of 14 cm, inner radius of 7 cm and the height of 7 cm | $B_{ex} = 21.2 \mu\text{T}$<br>at 60 Hz | $P = 6.32 \text{ mW};$<br>$S = 1.47 \mu\text{W}/\text{cm}^3$  |
| [52-53] |  | A long solenoid with a length of 50 cm and a radius of 2.5 cm                            | $B_{ex} = 18 \mu\text{T}$<br>at 50 Hz   | $P = 0.883 \text{ mW};$<br>$S = 0.85 \mu\text{W}/\text{cm}^3$ |

To the best of our knowledge, only three journal papers [52-54] from two research groups have been published to discuss the applications, the concepts and the design details of a free-standing energy harvester. Their experimental results are compared and summarized in Table 1.5. Tashiro *et al* designed a Brooks coil to harvest the magnetic field energy from a power

line [52]. The power harvested from their design was limited as they did not use a ferromagnetic core. Roscoe *et al* designed a solenoid with a ferromagnetic rod to collect the magnetic field energy in a substation [53]. It was concluded that a thin and long rod could have high effective permeability which leads to high output power. However, in their work, the cast iron was selected as the core material which suffered greatly from the eddy current losses. Furthermore, a thin and long rod is also prone to damage. Both of their coil designs [52-53] have some key limitations which reduces the output power. In addition to the coil design, it is equally important to have a proper matching circuit which could transfer the energy from the harvesting coil to an energy storage unit efficiently. In [52], only a compensating capacitor was added to eliminate the coil inductance and leave the coil resistance unmatched. Thus, the energy conversion efficiency of their circuit is relatively low. Besides, the matching circuit design becomes much more complicated if the load is not a linear component (e.g. diodes, transistors, rechargeable batteries or charging capacitors). In other words, the input impedance looking from the coil is not a constant so that a conventional matching network cannot work properly. As a consequence, a comprehensive study is necessary to fully investigate and optimize a free-standing energy harvesting system in terms of the coil design and the circuit analysis.

To summarize, the main objectives of this research are listed as follows:

1. To investigate the magnetic flux density near the high voltage infrastructure and identify where are the suitable places to deploy a free-standing magnetic field energy harvester
2. To further study the magnetization process of a ferromagnetic material and identify what factors may affect the magnetic flux density inside a ferromagnetic core
3. To design and optimize a new harvesting coil by considering the ferromagnetism, the core losses, the winding method and the physical size
4. To develop a delicate matching circuit which can transfer the energy from the harvesting coil into an energy storage unit efficiently
5. To design an energy management unit that utilizes the stored energy to power a commercial wireless sensor.

## 1.4 Organisation of the Thesis

The contents of this thesis are organised in the following manner:

Chapter 1 provides the background information of this the project, the motivations of the work, the literature review and the layout of the thesis.

In Chapter 2, the system overview of a free-standing magnetic field energy harvester is presented. The magnetic field near the high power equipment is investigated. The concept of the demagnetization in the ferromagnetic material is explained. The energy losses in a ferromagnetic core are analysed and discussed. A circuit structure is proposed which can utilize the harvested energy effectively to power a wireless sensor.

In Chapter 3, a new bow-tie-shaped coil is designed to produce a much lower demagnetization factor (hence more power) than that of a conventional solenoid. The relationship between the core shape and the output power is explored and optimized. The selection of core material is studied and it is found that Mn-Zn ferrite is the most suitable core material because it greatly reduces the eddy current losses. The relevant experiment is conducted which demonstrates the proposed bow-tie coil is much more efficient than a conventional solenoid.

Chapter 4 introduces a more advanced coil with a novel helical core. By lengthening the path of the magnetic flux in a ferromagnetic core, the demagnetization factor can be greatly reduced which leads to a higher power output. The geometry shape of the helical core is optimized to increase the path of the magnetic flux and better utilize the winding area available inside the core. From the experimental results, it is demonstrated that the proposed helical coil can have a much better performance than the bow-tie coil under the same testing conditions.

In Chapter 5, a completed circuit system is developed which utilizes the energy collected by the harvesting coil to power a commercial wireless sensor. A transient analysis is conducted to calculate the input resistance of a charging capacitor as a function of time. A switch mode power converter is designed as a matching network to increase the energy conversion efficiency from the harvesting coil to a storage capacitor. A commercial wireless sensor can

be powered up by the energy stored in the storage capacitor via an energy management unit.

Finally, Chapter 6 draws the conclusion of the work. The main objectives are reviewed, and the contributions are highlighted. Furthermore, the challenges and possible extensions for future research are presented.

## 1.5 References

- [1] S. Ulukus, A. Yener, E. Erkip, O. Simeone, M. Zorzi, P. Grover and K. Huang, "Energy Harvesting Wireless Communications: A Review of Recent Advances", *IEEE Journal Selected Areas Communications*, vol. 33, no. 3, pp. 360-381, 2015.
- [2] Z. Wan, Y. Tan and C. Yuen, "Review on energy harvesting and energy management for sustainable wireless sensor networks", *2011 IEEE 13th International Conference on Communication Technology*, 2011
- [3] S. Yuan, Y. Huang, J. Zhou, Q. Xu, C. Song and P. Thompson, "Magnetic Field Energy Harvesting Under Overhead Power Lines", *IEEE Transactions on Power Electronics*, vol. 30, no. 11, pp. 6191-6202, 2015.
- [4] Smart Grid Infrastructure: Energy Harvesting - Block Diagram (SBD) | TI.com", Ti.com, 2016. [Online]. Available: [http://www.ti.com/solution/energy\\_harvesting](http://www.ti.com/solution/energy_harvesting). [Accessed: 23- Mar- 2016]
- [5] D. Hostick, D. Belzer and S. Hadley, "Projecting Electricity Demand in 2050", Pacific Northwest National Laboratory, Washington, 2014
- [6] D. J. Spoor and J. P. Roberts, "Development and Experimental Validation of a Weather-Based Dynamic Line Rating System", *Innovative Smart Grid Technologies Aisa (ISGT)*, pp. 1-7, 2011
- [7] Y. Biçen; F. Aras and Y. Kirkrici, "Lifetime Estimation and Monitoring of Power Transformer Considering Annual Load Factors", *IEEE Transaction on Dielectrics and Electrical Insulation*, vol. 21, issue. 3, pp. 1360-1367, 2014
- [8] B.R. Flynn and GE Energy, "Key Smart Grid Application", Available: [http://www.gedigitalenergy.com/multilin/journals/issues/spring09/smart\\_grid\\_applications.pdf](http://www.gedigitalenergy.com/multilin/journals/issues/spring09/smart_grid_applications.pdf). [Accessed: 23- Mar- 2016]
- [9] D. M. Green, J. P. Gentle and K. S. Myers, "A Comparison of Real-Time Thermal Rating Systems in the U.S. and the U.K.", *IEEE Transactions on Power Delivery*, vol.

- 29, issue: 4, pp. 1849-1858, 2014
- [10] C. Li, G. Ma and B. Qi, "Condition Monitoring and Diagnosis of High-Voltage Equipment in China –Recent Progress", *IEEE Electrical Insulation Magazine*, vol. 29, issue: 5, pp. 71-78, 2013
  - [11] A. K. Kazerooni, J. Mutale, M. Perry, S. Venkatesan and D. Morrice, "Dynamic thermal rating application to facilitate wind energy integration", *IEEE Trondheim PowerTech*, pp. 1-7, 2011
  - [12] A. Safdarian, M. Degefa, M. Fotuhi-Firuzabad and M. Lehtonen, "Benefits of Real-Time Monitoring to Distribution Systems: Dynamic Thermal Rating", *IEEE Transaction on Smart Grid*, vol. 6, no. 4, pp. 2023-2031, 2015.
  - [13] "Island Yacht Club • Weather", *Islandyachtclub.org.uk*, 2016. [Online]. Available: <http://www.islandyachtclub.org.uk/weatherstation/weatheryc.html>. [Accessed: 25-Mar- 2016].
  - [14] Z. Wang, M. Begovi, and J. Wang, "Analysis of Conservation Voltage Reduction Effects Based on Multistage SVR and Stochastic Process", *IEEE Transactions on Smart Grid*, vol. 5, no. 1, pp. 431-439, 2014
  - [15] Z. Wang and J. Wang, "Review on Implementation and Assessment of Conservation Voltage Reduction", *IEEE Transaction on Power System.*, vol. 29, no. 3, pp. 1306-1315, 2014.
  - [16] D. Kirshner, "Implementation of conservation voltage reduction at Commonwealth Edison", *IEEE Transaction on Power System*, vol. 5, no. 4, pp. 1178-1182, 1990.
  - [17] "Smart Meters – ecomagination", *ecomagination.com*, 2016. [Online]. Available: <http://www.ge.com/files/ecomagination/portfolio/smart-meters/>. [Accessed: 25- Mar- 2016].
  - [18] "What are smart meters and can they reduce your gas and electricity costs? «Spiral Group", *Spiral-group.co.uk*, 2016. [Online]. Available: <http://www.spiral-group.co.uk/blog/?p=89>. [Accessed: 25- Mar- 2016].



- [19] I. E. Portugués, P. J. Moore, I. A. Glover, C. Johnstone and R.H. Mckosky, “RF-Based Partial Discharge Early Warning System for Air-Insulated Substations”, *IEEE Transactions on Power Delivery*, vol. 24, no. 1, pp. 20-29, 2009
- [20] G. Montanari and A. Cavallini, "Partial discharge diagnostics: from apparatus monitoring to smart grid assessment", *IEEE Electrical Insulation Magazine*, vol. 29, no. 3, pp. 8-17, 2013.
- [21] "CC-TEV - Capacitive Coupler - IPEC Ltd", *Ipec.co.uk*, 2016. [Online]. Available: <http://www.ipec.co.uk/pd-products/cc-tev-capacitive-coupler/>. [Accessed: 25- Mar- 2016].
- [22] "UV/IR Flame Detector Type X5200 - IP&S", *Ipands.pl*, 2016. [Online]. Available: <http://www.ipands.pl/index.php?id=29&l=en>. [Accessed: 25- Mar- 2016].
- [23] V. C. Gungor, B. Lu, G. P. Hancke, “Opportunities and Challenges of Wireless Sensor Networks in Smart Grid”, *IEEE Transaction on Industrial Electronics*, vol. 57, no. 10, pp. 3557 – 3564, 2010
- [24] V. Raghunathan, A. Kansal, J. Hsu, J. Friedman, Mani Srivastava, “Design considerations for solar energy harvesting wireless embedded systems,” *Information Processing in Sensor Networks*, pp. 457-462, 2005
- [25] S. Bader, B. Oelmann, “Enabling Battery-Less Wireless Sensor Operation Using Solar Energy Harvesting at Locations with Limited Solar Radiation,” *4<sup>th</sup> Int. conf. on Sensor Technologies and Applications (SENSORCOMM)*, pp. 602-608, 2010
- [26] H. Zangl, T. Bretterklieber and G. Brasseur, “A Feasibility Study on Autonomous Online Condition Monitoring of High-Voltage Overhead Power Lines”, *IEEE Transactions on Instrumentation and Measurement*, vol. 50, no. 5, pp. 1789-1796, 2009
- [27] J. A. Paradiso and T. Starner, “Energy Scavenging for Mobile and Wireless Electronics”, *IEEE Pervasive Computing*, vol. 4, pp.18-27, 2005
- [28] C. Tsai, C. Hsieh, S. Huang, “Enhancement of Damage-Detection of Wind Turbine

- Blades via CWT-Based Approaches”, *IEEE Transactions on Energy Conversion*, vol. 21, no. 3, pp. 776-781, 2006
- [29] "National Grid substations | EMFs.info", *EMFs.info*, 2013. [Online]. Available: <http://www.emfs.info/sources/substations/substations-ng/>. [Accessed: 28- Mar- 2016].
- [30] F. Guo, H. Hayat and J. Wang, "Energy harvesting devices for high voltage transmission line monitoring", *2011 IEEE Power and Energy Society General Meeting*, 2011.
- [31] H. Zangl, T. Bretterklieber and G. Brasseur, "A Feasibility Study on Autonomous Online Condition Monitoring of High-Voltage Overhead Power Lines", *IEEE Trans. Instrum. Meas.*, vol. 58, no. 5, pp. 1789-1796, 2009.
- [32] M. Moser, T. Bretterklieber, H. Zangl and G. Brasseur, "Strong and Weak Electric Field Interfering: Capacitive Icing Detection and Capacitive Energy Harvesting on a 220-kV High-Voltage Overhead Power Line", *IEEE Transaction on Industrial Electronics.*, vol. 58, no. 7, pp. 2597-2604, 2011.
- [33] J. Zhang, P. Li, Y. Wen, F. Zhang and C. Yang, "A Management Circuit with Upconversion Oscillation Technology for Electric-Field Energy Harvesting", *IEEE Transactions on Power Electronics*, vol. 31, no. 8, pp. 5515-5523, 2016.
- [34] R. Moghe, A. Iyer, F. Lambert and D. Divan, "A Low-Cost Electric Field Energy Harvester for an MV/HV Asset-Monitoring Smart Sensor", *IEEE Transactions on Industry Applications*, vol. 51, no. 2, pp. 1828-1836, 2015.
- [35] M. Zhu, M. Judd and P. Moore, "Energy Harvesting in Substations for Powering Autonomous Sensors", *2009 Third International Conference on Sensor Technologies and Applications*, 2009.
- [36] J. Rodriguez, D. Holmes, B. McGrath and R. Wilkinson, "Maximum energy harvesting from medium voltage electric-field energy using power line insulators", *2014 Australasian Universities Power Engineering Conference (AUPEC)*, 2014.
- [37] Ferroxcube, 3E8 Material Specification, [Online]. Available:

- <http://www.ferroxcube.com/FerroxcubeCorporateReception/datasheet/3e8.pdf>,  
[Accessed: 28- Mar- 2016].
- [38] "Metglas 2714A Magnetic Alloy - Ideal Shielding and sensor material", *Metglas.com*, 2016. [Online]. Available: [http://www.metglas.com/products/magnetic\\_materials/2714a.asp](http://www.metglas.com/products/magnetic_materials/2714a.asp). [Accessed: 25- Apr- 2016].
- [39] Wiltan, Nanocrystalline Material Specification, [Online]. Available: [http://www.wiltan.co.uk/client\\_files/default/nanocrystalline\\_cores.pdf](http://www.wiltan.co.uk/client_files/default/nanocrystalline_cores.pdf) [Accessed: 25- Apr- 2016].
- [40] "Permalloy 80 | Permalloy 80", *Espimetals.com*, 2016. [Online]. Available: <http://www.espimetals.com/index.php/technical-data/175-permalloy-80>. [Accessed: 25- Apr- 2016].
- [41] Mingshang, Mu-metal 1J85 Material Specification, [Online]. Available: <http://ft.chinaln.bmlink.com/supply-3964124.html> [Accessed: 25- Apr- 2016].
- [42] DMEGC, Ferrite R15K Material Specification, 2016. [Online]. Available: [http://www.chinadmegc.com/material\\_download.php?23](http://www.chinadmegc.com/material_download.php?23). [Accessed: 25- Apr- 2016].
- [43] Ferroxcube, 3E5 Material Specification, [Online]. Available: <http://www.ferroxcube.com/FerroxcubeCorporateReception/datasheet/3e5.pdf>,  
[Accessed: 25- Apr- 2016].
- [44] M. dos Santos, D. Vieira, Y. Rodriguez, C. Souza, T. Moraes and R. Freire, "Energy harvesting using magnetic induction considering different core materials", *2014 IEEE International Instrumentation and Measurement Technology Conference (I2MTC) Proceedings*, 2014.
- [45] N. Roscoe, M. Judd and J. Fitch, "Development of magnetic Induction Energy Harvesting For Condition Monitoring", *2009 44th International University Power Engineering Conference (UPEC)*, 2009.
- [46] J. Moon and S. Leeb, "Analysis Model for Magnetic Energy Harvesters", *IEEE*

- Transactions on Power Electronics*, vol. 30, no. 8, pp. 4302-4311, 2015.
- [47] J. Moon, J. Donnal, J. Paris and S. Leeb, "VAMPIRE: A magnetically self-powered sensor node capable of wireless transmission", *2013 Twenty-Eighth Annual IEEE Applied Power Electronics Conference and Exposition (APEC)*, 2013.
- [48] J. Moon and S. Leeb, "Power Electronic Circuits for Magnetic Energy Harvesters", *IEEE Transactions on Power Electronics*, vol. 31, no. 1, pp. 270-279, 2016.
- [49] J. Moon and S. Leeb, "Power loss analysis with high primary current in magnetic energy harvesters", *2015 IEEE 16th Workshop on Control and Modeling for Power Electronics (COMPEL)*, 2015.
- [50] R. Bhuiyan, R. Dougal and M. Ali, "A Miniature Energy Harvesting Device for Wireless Sensors in Electric Power System", *IEEE Sensors Journal*, vol. 10, no. 7, pp. 1249-1258, 2010.
- [51] K. Tashiro, H. Wakiwaka, S. Inoue and Y. Uchiyama, "Energy Harvesting of Magnetic Power-Line Noise", *IEEE Transaction on Magnetics.*, vol. 47, no. 10, pp. 4441-4444, 2011.
- [52] N. Roscoe and M. Judd, "Harvesting Energy From Magnetic Fields to Power Condition Monitoring Sensors", *IEEE Sensors Journal*, vol. 13, no. 6, pp. 2263-2270, 2013.
- [53] N. Roscoe and M. Judd, "Optimization of Voltage Doublers for Energy Harvesting Applications", *IEEE Sensors Journal*, vol. 13, no. 12, pp. 4904-4911, 2013.
- [54] MICAz wireless sensor, (MPR2400) 2.4 GHz Mote, <http://www.memsic.com/products/wireless-sensor-networks/wirelessmodules.html>, Accessed: 25- Apr- 2016]

## **Chapter 2: System Overview of Free-standing Magnetic Field Energy Harvesting**

### **2.1 Introduction**

The knowledge provided in this chapter is to gain a better understanding of a free-standing magnetic field energy harvesting system. The chapter is divided into two parts:

In the first part, the magnetic flux density near high voltage equipment is studied as it is one of the most important factors to determine the maximum power that can be harvested. Two typical environments (under overhead power lines and inside electric substations) are investigated. A case study is presented to calculate the distributions of the magnetic flux density under a 400 kV double circuit pylon. It is found that the field distributions are determined by many factors such as the line current, the balance in the three phase system, the line sag, etc. The field distributions in an electric substation are even more complicated as there are a variety of power equipment carrying currents in different directions.

In the second part, a system overview of a free-standing magnetic field energy harvester is presented. An equivalent circuit is introduced to model a harvesting coil connected with a matched load. Three case studies are provided to calculate the effective permeability of the cores with different shapes and the concept of the demagnetization in a ferromagnetic core is explained in details. The energy losses in the ferromagnetic core are analysed. It is found that the eddy current losses are dominant in the core losses and can be reduced either by optimizing the core shape or using a core material with higher resistivity. Finally, a circuit structure is proposed which utilizes the harvested energy effectively to power a wireless sensor.

## 2.2 Magnetic Field near High Voltage Equipment

### 2.2.1 Under Overhead Power Lines

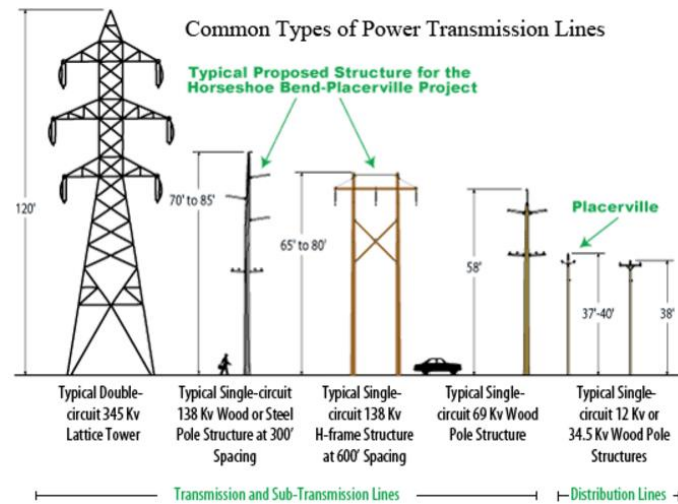


**Fig. 2.1** Different kinds of overhead power lines [1]

Obviously, for different kinds of pylons shown in Fig. 2.1, the physical structures of overhead power lines and their corresponding typical line currents are different, resulting in various distributions of the magnetic fields. The UK National Grid [2] used the L12 pylon for their study and the same system is used in this work for comparisons. The physical structure of a L12 pylon is shown in Fig. 2.2.

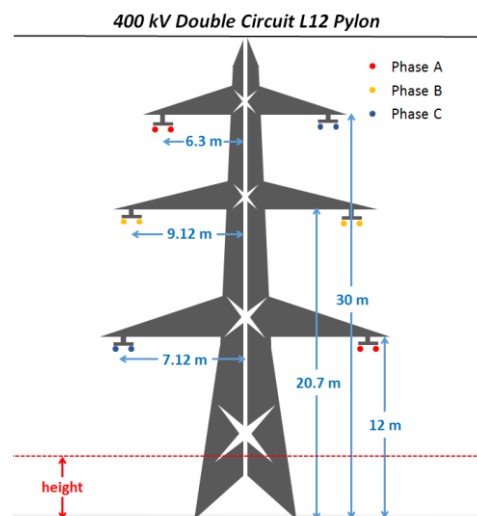


**Fig. 2.2** The physical structure of a 400 kV double circuit L12 Pylon

As overhead power lines are usually significantly long so that they can be treated as infinite long lines, hence a 3D field problem can be simplified to a 2D one. Due to the large ground plan underneath, the electromagnetic wave reflects back from the earth may be considered and the image theory can be applied [3]. The image current is equal in magnitude and opposite in direction to the real current in the conductor. However, as the ground is not a perfect conductor, the distance of the image conductor buried under the ground can be expressed by  $(z_i + \alpha)$  as shown in Fig. 2.3 [3].

$$\alpha = \sqrt{2}\delta e^{-j\pi/4} \quad (2.1)$$

$$\delta = 503 \sqrt{\rho_g / f} \quad (2.2)$$

where  $\rho_g$  is the earth resistivity in  $\Omega\text{m}$  and  $f$  is the frequency in Hz. As the typical values of the earth resistivity range from 10 to 100  $\Omega\text{m}$ , the image currents are normally hundreds of meters below the earth [3]. Therefore, the magnetic field reflected by the imperfect ground is relatively small and therefore can be ignored.

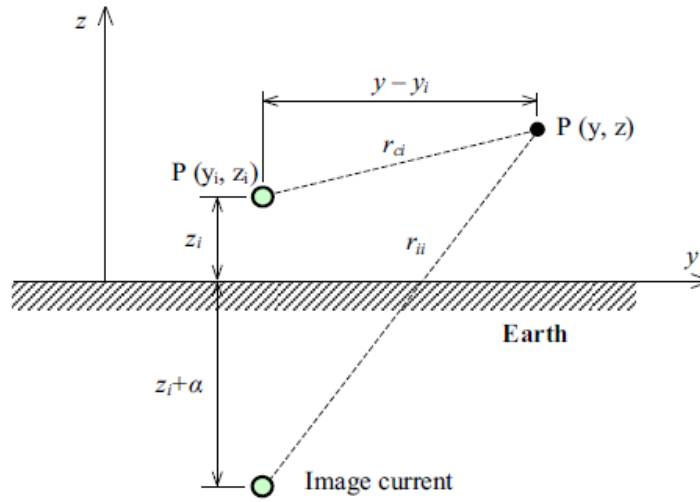


**Fig. 2.3 Image current due to the imperfect ground [3]**

As the frequency of the electrical power system is extremely low (50/60 Hz), quasi-static approximations can be applied to simplify the field calculation. In [4], it shows that the quasi-static approximations only result in an error of 0.000002% for fields at 100 m or less from the power line. Thus, Ampere's Law can be applied on each conductor to calculate the magnetic flux density at a particular point as plotted in Fig. 2.4:

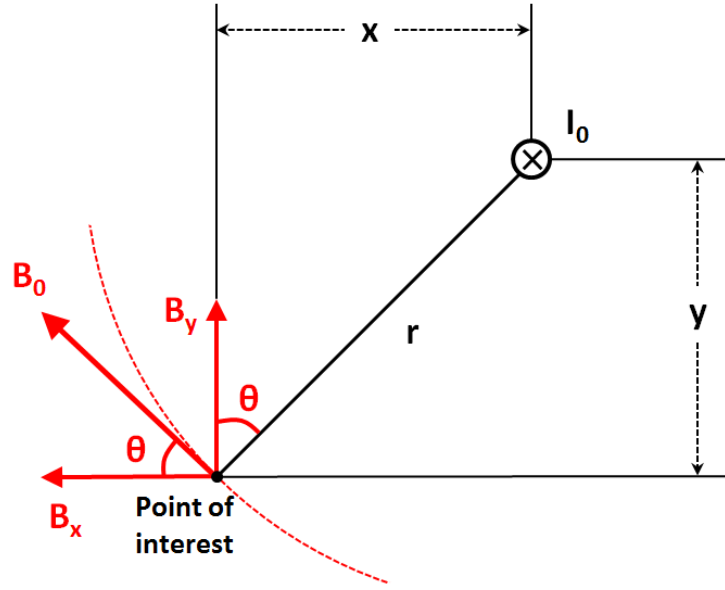


Fig. 2.4 The magnetic flux density generated from a current

$$B_0 = \frac{\mu_0 I_0 \sin(\omega t)}{2\pi r} \quad (2.3)$$

where  $B_0$  is the magnetic flux density generated by the conductor in T,  $\mu_0$  is the permeability of the free space in H/m,  $I_0$  is the amplitude of the current inside the conductor,  $\omega$  is the angular frequency in rad/s,  $t$  is the time in second and  $r$  is the distance between the current conductor and the point of interest. The magnetic flux density  $B_0$  can be decomposed in  $x$  and  $y$  direction [2]:

$$B_{0x} = B_0 \cos \theta = \frac{\mu_0 I_0 \sin(\omega t) y}{2\pi r^2} \quad (2.4)$$

$$B_{0y} = B_0 \sin \theta = \frac{\mu_0 I_0 \sin(\omega t) x}{2\pi r^2} \quad (2.5)$$

For a balanced three-phase system, the current in each conductor has the same amplitude while the phase is  $120^\circ$  apart from the other two.

Table 1.1 The current in a three-phase system

| Phase A              | Phase B                               | Phase C                               |
|----------------------|---------------------------------------|---------------------------------------|
| $I_0 \sin(\omega t)$ | $I_0 \sin(\omega t + \frac{2}{3}\pi)$ | $I_0 \sin(\omega t - \frac{2}{3}\pi)$ |



As the pylon L12 has two three-phase circuits (one on each side), the overall magnetic flux density of a particular point can be calculated by the summation of the magnetic flux density from 6 conductors:

$$B_x = B_{Ax} + B'_{Ax} + B_{Bx} + B'_{Bx} + B_{Cx} + B'_{Cx} \quad (2.6)$$

$$B_y = B_{Ay} + B'_{Ay} + B_{By} + B'_{By} + B_{Cy} + B'_{Cy} \quad (2.7)$$

$$B_{total} = \sqrt{B_x^2 + B_y^2} \quad (2.8)$$

where  $B_{Ax}$  and  $B'_{Ax}$  are the magnetic flux densities in x direction generated from the two current conductors in phase A in the double circuits and  $B_{total}$  is the overall magnetic flux density at the point of interest (POI).

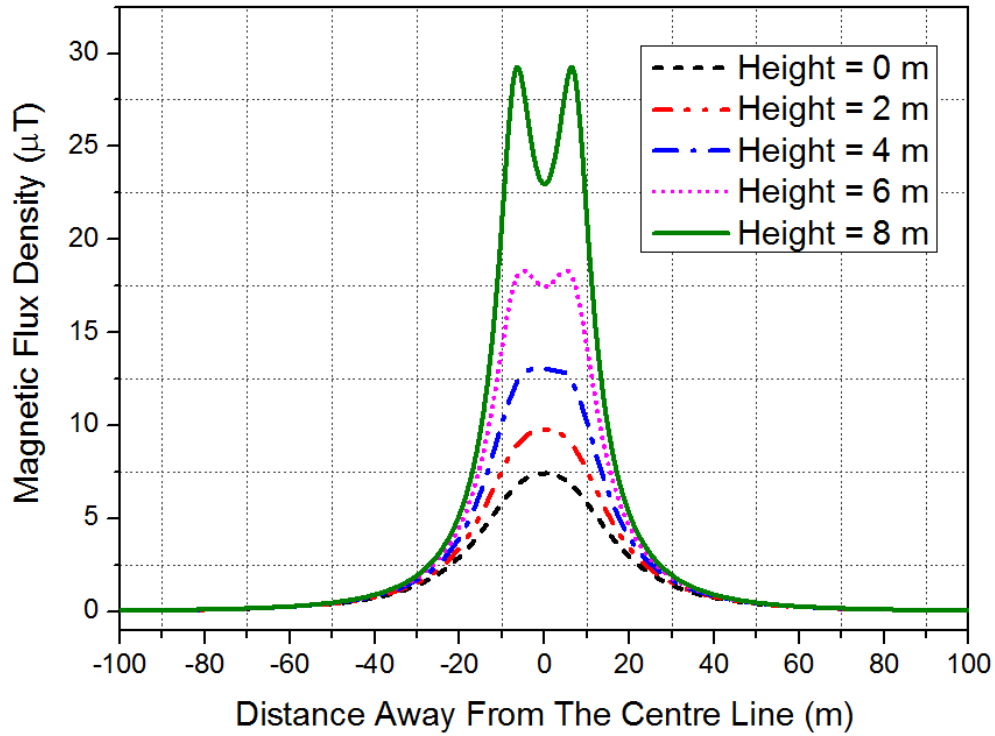


**Fig. 2.5** The magnetic flux density under the L12 pylon when the current is 700 A in both circuits

According to the data from the UK National Grid [4], the overhead power line used for bulk transmissions can have a current rating of 4000 A, but the average current in a typical circuit is around 700 A. We first assume that the two three-phase circuits are perfectly balanced and carry a current of 700 A in each phase. Under these conditions, the magnetic flux densities under the L12 pylon are calculated and plotted in Fig. 2.5. The results are in good agreement

with the data provided by the UK National Grid [5]. It is expected that the flux density increases with the height as it is more close to the current conductor. When the height above the ground is lower than 6 meters, the largest magnetic flux density always appears in the centre of the pylon. As shown in Fig. 2.6, a weather station is usually installed on the anti-climbing protective device where is 4 or 5 meters above the ground [6]. The magnetic flux density in this case is around  $12 \mu T_{rms}$ .



Fig. 2.6 Example of a weather station installed on the anti-climbing protective device [6]

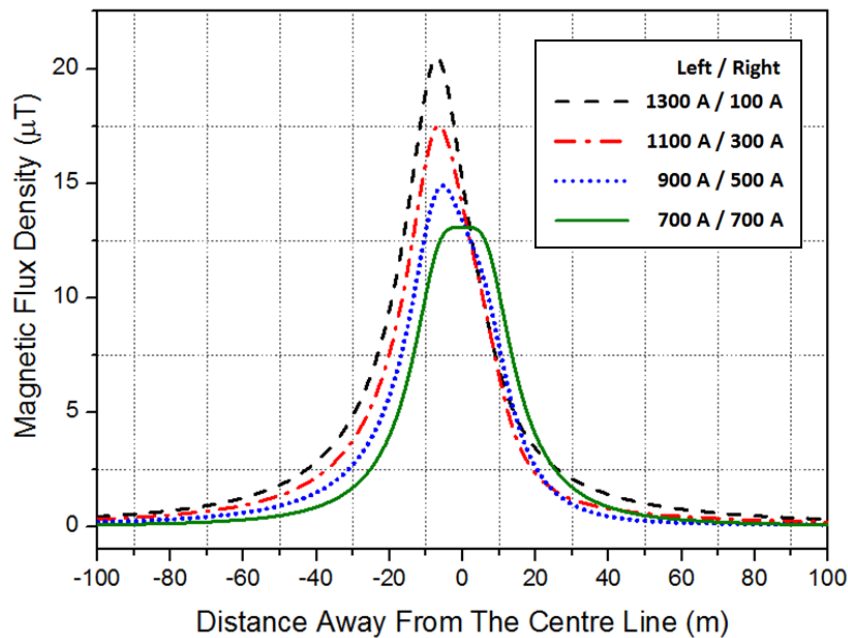


Fig. 2.7 The magnetic flux density under the L12 pylon when the height is 4 meters above the ground

However, the two three-phase circuits in the pylon are not always balanced especially when the two circuits are used to supply the power to different places. The distributions of the

magnetic flux densities change when the two circuits are not balanced. We assume that the two three-phase systems carry a total current of 1400 A but share it differently. The flux densities at 4 m above the ground are calculated and plotted in Fig. 2.7. The maximum flux density generated from the two unbalanced circuits is always higher than that of the balanced one. If the three-phase circuit on the left hand side has a higher current as depicted in Fig. 2.7, the  $B$  field at this side is larger compared to the balanced situation (700 A in each circuit). On the contrary, the  $B$  field on the right side of the pylon is smaller compared to the balanced case. However, in reality, it is very difficult to predict which circuit in a pylon will have a higher current. It is important to note that the flux density at the centre of the pylon does not change significantly when the two circuits are unbalanced.

In conclusion, the best place to deploy a free-standing energy harvester is directly under the centre of a pylon where the magnetic flux density is large and consistent. In Table 2.1, the magnetic flux densities under various overhead power lines have been summarized based on the data provided by the UK National Grid [5]. The magnetic flux density is always higher than  $7 \mu\text{T}_{rms}$  which could be a reliable energy source for a free-standing magnetic field energy harvester.

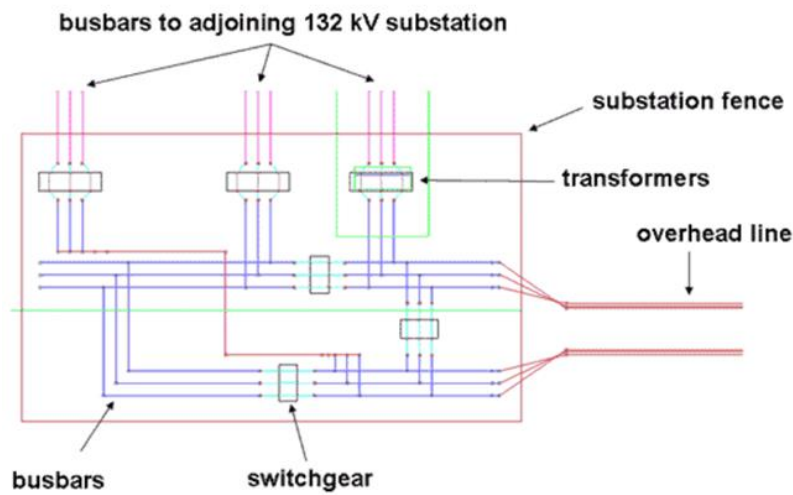
**Table 2.1 Summary of the magnetic flux density under overhead lines**

| The types of overhead power lines | Test conditions   | Magnetic flux density at the centre of the pylon |
|-----------------------------------|---|--|
| 400 kV L12 Pylon                  | $I = 700$ A (balanced circuit)<br>3 meters above the ground | $11.3 \mu\text{T}_{rms}$                         |
| 400 kV T-Pylon                    | $I = 700$ A (balanced circuit)<br>3 meters above the ground | $7.7 \mu\text{T}_{rms}$                          |
| 132 kV L7 Pylon                   | $I = 700$ A (balanced circuit)<br>4 meters above the ground | $8.6 \mu\text{T}_{rms}$                          |
| 132 kV L4 Pylon                   | $I = 700$ A (balanced circuit)<br>4 meters above the ground | $8.2 \mu\text{T}_{rms}$                          |

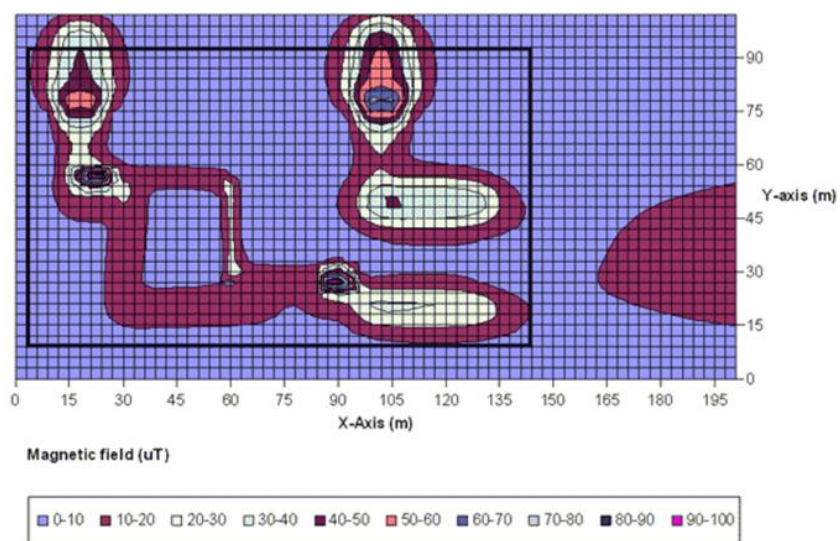
## 2.2.2 Inside Electrical Substations



(a)



(b)



(c)

Fig. 2.8 (a) the picture of a 132 kV substation (b) the physical structure of a 132 kV substation, (c) the magnetic flux density inside the substation [7]

Electrical substations are where various power cables are connected and switched and where the voltage is changed by power transformers. It is very complicated to calculate the magnetic field accurately in a substation as there are a variety of conductors carrying currents in different directions. The UK National Grid has built a simple model of a 132 kV substation which only includes a double circuit overhead line, busbars, switchgears and transformers [7]. The layout of the substation and the magnetic flux densities are plotted in Fig. 2.8. It is noted that the flux density  $B$  near the busbars varies from 10 to 20  $\mu\text{T}_{rms}$  while the  $B$  field close to the transformers can be as high as 60  $\mu\text{T}_{rms}$ . Although it is only a simplified model, it indicates the magnetic flux density in the substation is relatively high especially close to transformers.

There are several published papers on the investigation of the levels of the magnetic flux density  $B$  inside different electrical substations. The results are summarized in Table 2.2. They have confirmed that the flux density does not exceed regulatory levels [8 - 11]. From their work, it can be concluded that the magnetic flux densities are always higher when it is close to transformers and switchgears. Therefore, in the vicinity of these power devices where the magnetic field strength is strong and consistent, plenty of energy can be harvested by a free-standing magnetic field energy harvester to power a wide range of condition monitoring sensors.

**Table 2.2 Summary of the magnetic flux density inside different substations**

| The types of electrical substations | Test conditions                         | Magnetic flux density        |
|-------------------------------------|---|------------------------------|
| 11 kV indoor Substation [8]         | Near power transformers and switchgears | 15 - 20 $\mu\text{T}_{rms}$  |
| 150 kV outdoor Substation [9]       | Close to voltage transformers           | 26 - 28 $\mu\text{T}_{rms}$  |
| 345 kV outdoor Substation [10]      | Near high voltage circuit breakers      | 30 - 40 $\mu\text{T}_{rms}$  |
| 400 kV outdoor Substation [11]      | In the vicinity of an air-core reactor  | 50 - 150 $\mu\text{T}_{rms}$ |

## 2.3 Overview of a Magnetic Field Energy Harvester

### 2.3.1 System Modelling

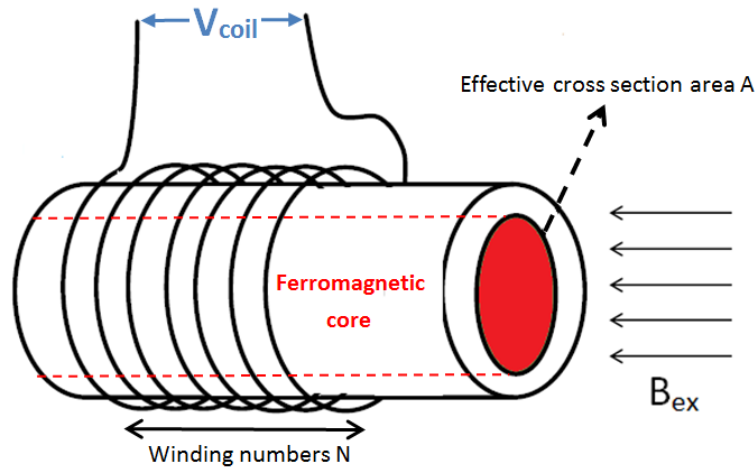


Fig. 2.9. A free-standing solenoid with a ferromagnetic core placed inside an alternating magnetic field

At 50/60 Hz, the most efficient way to harvest the magnetic field energy is to employ coils wrapped typically on ferromagnetic cores as shown in Fig. 2.9. Though the energy harvesting coil may be several meters away from the high voltage equipment, it is still an inductive coupling system since the wavelength of the 50/60 Hz electromagnetic wave is extremely long. Therefore, the maximum power that the coil can harvest does not solely depend on the surrounding magnetic field, but also on the effective coil resistance and the optimized load.

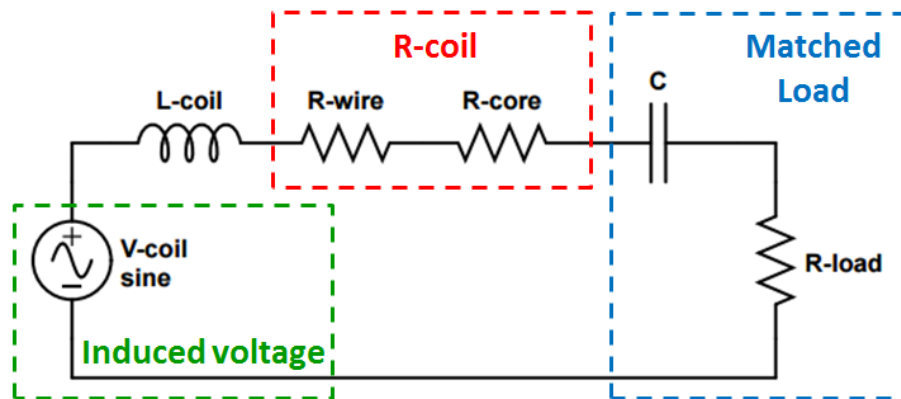


Fig. 2.10 The equivalent circuit of a free-standing energy harvester with a matched load.

Fig. 2.10 shows the equivalent circuit of a harvesting coil connected with a compensating capacitor and a load resistor with the same value of  $R_{coil}$ . The induced coil voltage  $V_{coil}$  is a function of the surrounding magnetic flux density and the coil properties by applying Faraday's Law:

$$V_{coil} = N\omega B_{core}A \quad (2.9)$$

where  $V_{coil}$  is the RMS voltage of the AC waveform,  $N$  is the number of turns wound on the coil,  $B_{core}$  is the magnetic flux density inside the ferromagnetic core in  $T_{rms}$ ,  $A$  represents the effective cross section of the coil in  $m^2$ ,  $\omega$  is the angular frequency in rad/s.

The effective coil resistance  $R_{coil}$  consists of two parts: copper resistance and equivalent core resistance. The copper resistance is caused by the resistance of the long enameled wire wound on the core.

$$R_{copper} = \rho_{wire}l_{wire} \quad (2.10)$$

where  $\rho_{wire}$  is the wire resistance in  $\Omega/m$  and  $l_{wire}$  is the total length of the enameled wire in m. When the core is subject to a time-varying magnetic field, some of the power to be delivered to the load is lost in the core and is dissipated as heat. These losses can be treated as the equivalent core resistance. To provide the maximum power from the coil to the load, the maximum power transfer theory is applied. A compensating capacitor  $C = 1/(\omega^2 L_{coil})$  is added in series to the coil to eliminate the coil inductance  $L_{coil}$ . The load resistance  $R_{load}$  should be the same of the coil resistance. Under this condition, as shown in Fig. 2.10, the power delivered to the load:

$$P_{load} = \left(\frac{V_{coil}}{2}\right)^2 / R_{coil} \quad (2.11)$$

The *power density* (the output power per unit volume, which is different from the definition of the power density in electromagnetics) of this system can be derived as follow:

$$S_{power} = \frac{1}{4} \frac{V_{coil}^2}{R_{coil}} / Vol \quad (2.12)$$

where  $Vol$  is the total volume of the harvesting coil in  $m^3$ . To maximize the power output from the coil, its coil voltage  $V_{coil}$  should be increased while the coil resistance  $R_{coil}$  must be minimized. These two variables are correlated to the core shape, the core material and the

properties of the enameled wires.

### 2.3.2 Effective Permeability and Demagnetization Factor

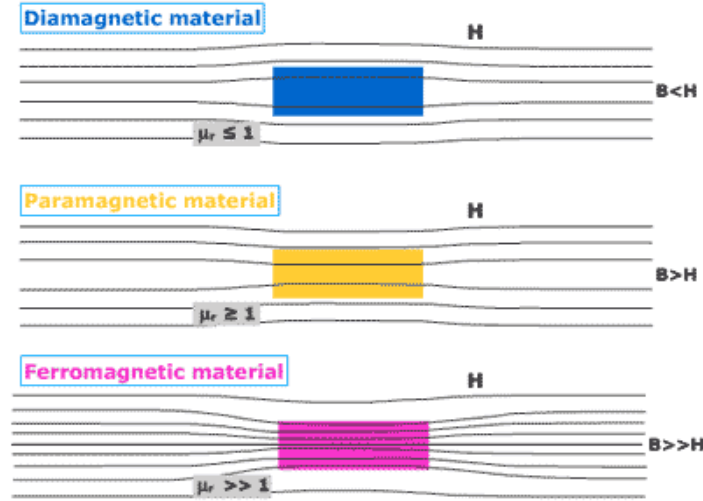


Fig. 2.11 The distribution of the magnetic flux with different magnetic material [12]

In the power transformer system, the laminated iron core is used to improve the energy conversion efficiency. The similar idea can be applied in the energy harvesting system to scavenge more magnetic field energy. When a specific material is placed in a magnetic field, the field distributions will be disturbed depending on the relative permeability of the material shown in Fig. 2.11. The ferromagnetic material can attract surrounding magnetic flux to pass through themselves so that they can be used as the core material to capture more magnetic field energy. According to Equation (2.9) and (2.12), the magnetic flux density in the core  $B_{core}$  is one of the most important factors to determine the output power. Therefore, the purpose of this section is to investigate  $B_{core}$  when a ferromagnetic core is placed in an externally applied magnetic field  $H_{ex}$ .

When a ferromagnetic core is subjected to an external magnetic field  $H_{ex}$ , the magnetic flux density  $B_{core}$  consists of two contributions:

$$B_{core} = \mu_0(H_{core} + M) \quad (2.13)$$

where  $H_{core}$  is the magnetic field inside the core in A/m generated either by electrical



currents outside the material or from a permanent magnet;  $M$  is the magnetization in A/m inside the material caused by  $H_{core}$ . The magnetization  $M$  and the flux density  $B_{core}$  can be correlated to  $H_{core}$  by the susceptibility  $\chi$  and permeability  $\mu$  [13]:

$$\chi = \frac{M}{H_{core}} \quad (2.14)$$

$$\mu = \frac{B_{core}}{H_{core}} \quad (2.15)$$

The susceptibility and permeability describe the response of a magnetic material when subjected to an external magnetic field [13]. It should be noted that the susceptibility and permeability may or may not be constant depending on the type of material. For example, when a ferromagnetic core is saturated, the magnetization  $M$  in the core does not increase with the magnetic field  $H_{core}$  as shown in Fig. 2.12(a). However, in the application of energy harvesting, the magnetic field  $H_{core}$  is quite small and a soft ferromagnetic material with a small coercive field is used. Therefore, we can assume that  $M$  is always linearly proportional to  $H_{core}$  as shown in Fig. 2.12(b). In the application of a free-standing magnetic field energy harvester,  $\chi$  and  $\mu$  can be treated as constants.

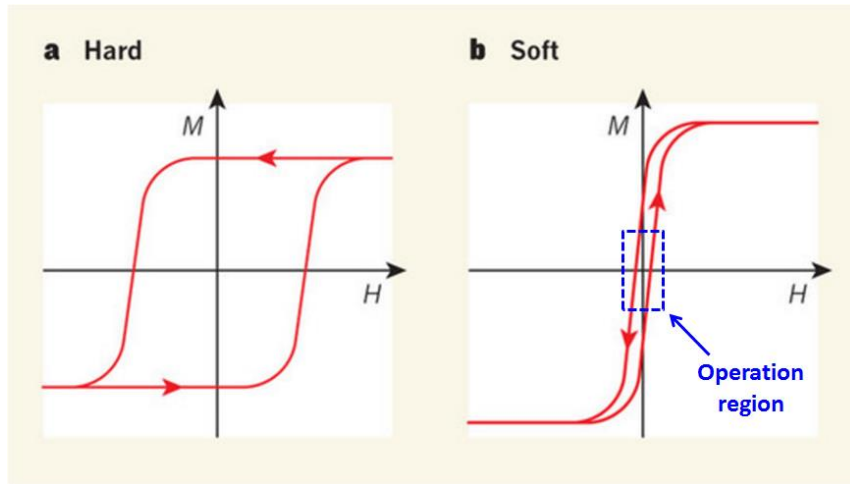


Fig. 2.12 The hysteresis loop of hard and soft ferromagnetic materials [14]

The term ‘relative permeability’ of a material is defined by:

$$\mu_r = \frac{\mu}{\mu_0} \quad (2.16)$$

$$B_{core} = \mu_r \mu_0 H_{core} \quad (2.17)$$

where  $\mu_0$  is the permeability of free space  $\mu_0 = 4\pi \times 10^{-7}$  H/m. In some circumstances, it is difficult to directly calculate the value of the magnetic field inside the core  $H_{core}$ . Thus, the term ‘effective permeability’ is defined to directly describe the relationship between flux density inside the core  $B_{core}$  and the external applied magnetic field  $H_{ex}$ :

$$B_{core} = \mu_{eff}\mu_0 H_{ex} = \mu_{eff} B_{ex} \quad (2.18)$$

Three different situations have been studied to calculate the flux density  $B_{core}$  by a given  $H_{ex}$ . If there is a conductor carries a current of  $I$  A shown in Fig. 2.13, the magnetic field  $H_{ex}$  can be calculated by Ampere’s law:

$$H_{ex} = \frac{I}{2\pi r} \quad (2.19)$$

where  $r$  is the distance away from the current conductor. when  $I = 1$  A and  $r = 5$  cm, the magnetic field  $H_{ex}$  is around 3.2 A/m and the external magnetic flux density  $B_{ex}$  is 4  $\mu$ T.

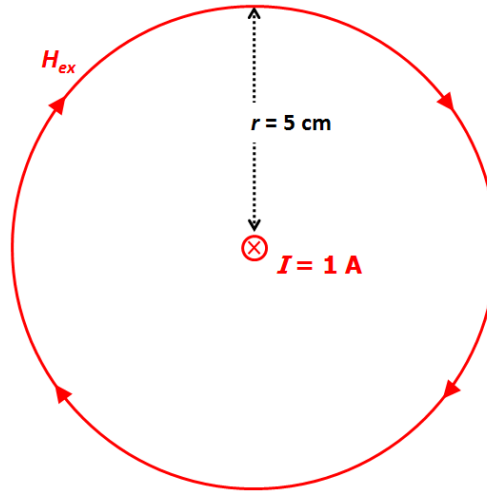


Fig. 2.13 The magnetic field around a current conductor

### **Situation One:**

If there is a toroid core fully enclosed to a current conductor as shown in Fig. 2.14, the magnetic field inside the core  $H_{core}$  can also be calculated by Ampere’s law as the magnetic flux travels in a single medium. In this scenario, the effective permeability  $\mu_{eff}$  is equal to the relative permeability  $\mu_r$  of the core material and therefore  $B_{core}$  is linearly proportional

to  $\mu_r$  as shown in Fig. 2.15. If the relative permeability  $\mu_r$  is 1000, the flux density in the core  $B_{core}$  is 4 mT which is 1000 times higher than the external applied magnetic flux density  $B_{ex}$ .

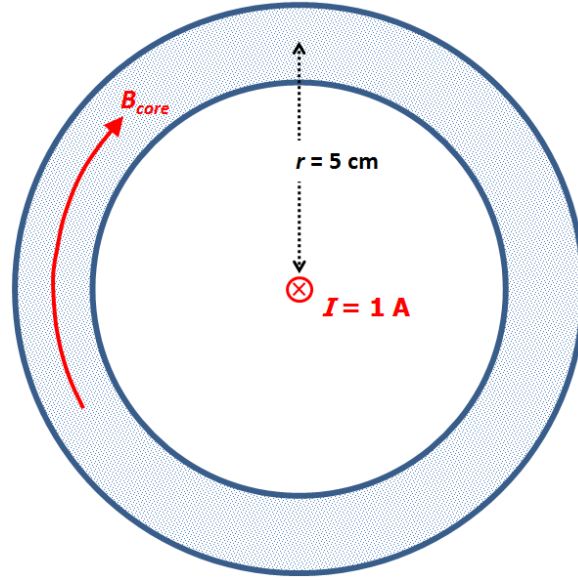


Fig. 2.14 A toroid with a ferromagnetic core

$$H_{core} = H_{ex} = \frac{I}{2\pi r} \quad (2.20)$$

$$B_{core} = \mu_r \mu_0 H_{core} = \mu_r B_{ex} \quad (2.21)$$

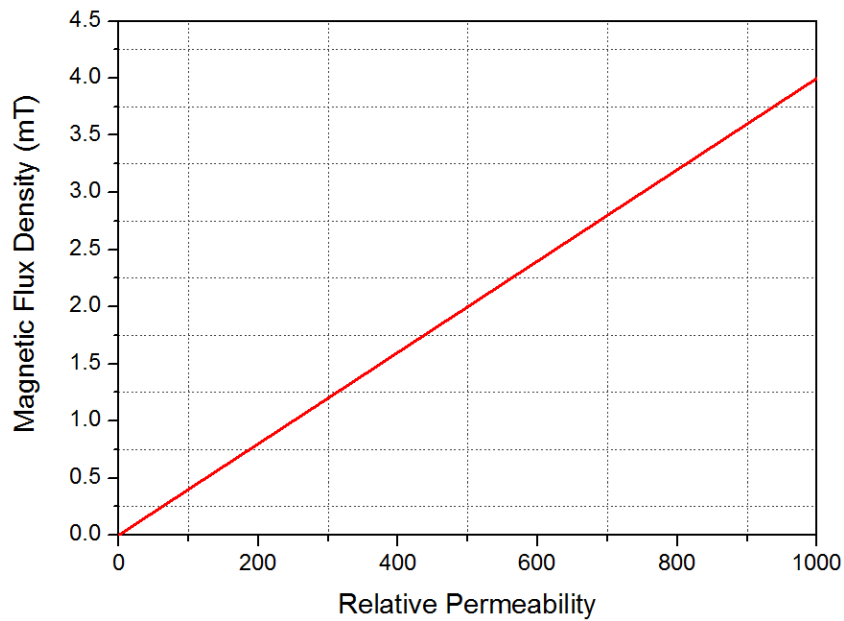
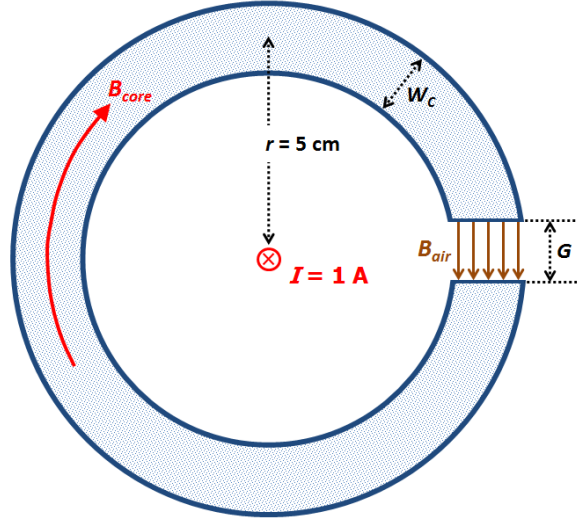


Fig. 2.15 The magnetic flux density  $B_{core}$  in a toroid as a function of the relative permeability

**Situation Two:****Fig. 2.16 A ferromagnetic toroid with an air gap**

If a toroid core with a small air gap is clamped on the current conductor as shown in Fig. 2.16, Equation (2.21) is not valid in this case since the magnetic flux travels through two different mediums. If Ampere's law is applied again:

$$I = H_{core}(2\pi r - G) + H_{air}G \quad (2.22)$$

where  $H_{core}$  is the magnetic field inside the core,  $G$  is the length of the air gap,  $H_{air}$  is the magnetic field in the air gap. Obviously, the magnetic field in this case is discontinuous when travels from the core into the air gap. Thus it is difficult to calculate the magnetic field  $H_{core}$  and then obtain the flux density  $B_{core}$ . The theory of magnetic circuits can be applied to calculate  $B_{core}$  as a function of the effective permeability  $\mu_{eff}$  and the applied magnetic field  $H_{ex}$ . As the air gap is quite small compared to the perimeter of the toroid core, fringing fields can be ignored and the magnetic flux in the core can be calculated [13]:

$$\varphi = \frac{\eta}{R_m} \quad (2.23)$$

where  $\varphi$  is the magnetic flux in Webbers (analogue to current in electrical circuits),  $\eta$  is the magnetomotive force in ampere-turns (analogue to voltage in electrical circuits),  $R_m$  is the magnetic reluctance in ampere-turns per weber (analogue to resistance in electrical circuits). These three parameters can be obtained by:

$$\varphi = B_{core}A \quad (2.24)$$

$$A = \pi(0.5W_c)^2 \quad (2.25)$$

$$\eta = I \quad (2.26)$$

$$R_m = \frac{2\pi r - G}{A\mu_r\mu_0} + \frac{G}{A\mu_0} \quad (2.27)$$

where  $A$  is the cross section area of the toroid core in  $m^2$ ,  $W_c$  is the radius of the cross section area in m. By combining Equation (2.23) to (2.27):

$$B_{core} = \frac{I\mu_r\mu_0}{2\pi r - G + G\mu_r} \quad (2.28)$$

The current  $I$  can be substituted by Equation (2.18),

$$B_{core} = \frac{2\pi r\mu_r}{2\pi r - G + G\mu_r} \mu_0 H_{ex} \quad (2.28)$$

The effective permeability  $\mu_{eff}$  can be defined as:

$$\mu_{eff} = \frac{2\pi r\mu_r}{2\pi r - G + G\mu_r} \quad (2.30)$$

$$B_{core} = \mu_0 \mu_{eff} H_{ex} \quad (2.31)$$

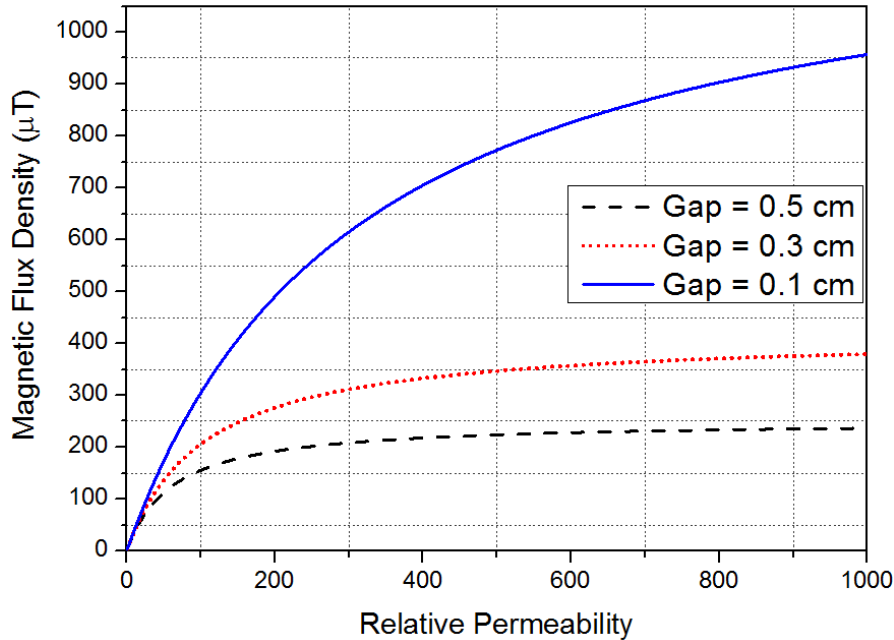


**Fig. 2.17** The magnetic flux density  $B_{core}$  of a toroid with a gap as a function of the relative permeability

If the air gap  $G$  is configured to 0.5 cm and  $\mu_r = 1000$ , the effective permeability  $\mu_{eff}$  is only

around 62.4. By introducing a small air gap to a toroid core, the flux density  $B_{core}$  is significantly reduced compared to an unbroken one. When the air gap becomes larger, the magnetic flux  $B_{core}$  is further reduced as depicted in Fig. 2.17.

### **Situation Three:**

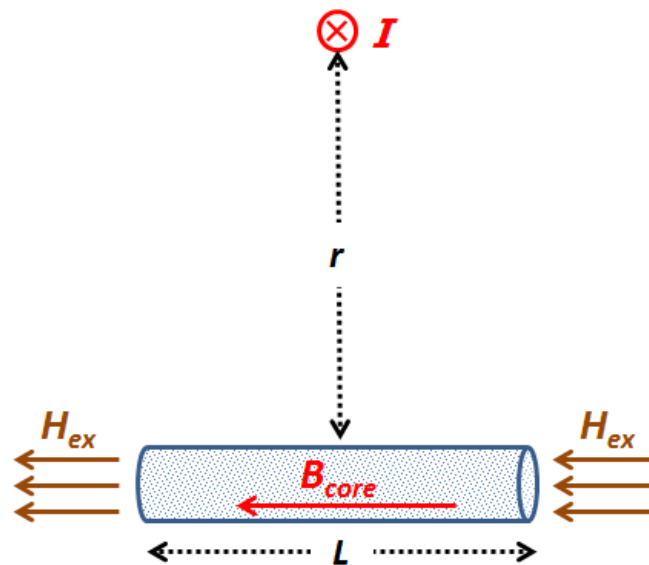


**Fig. 2.18 A ferromagnetic rod below a current conductor**

However, when there is only a ferromagnetic rod under a current conductor shown in Fig. 2.18, the problem becomes much more complicated compared to a toroid clamped on a conductor. The theory of magnetic circuits cannot be applied as the majority of the magnetic flux generated from the current conductor is distributed in the air. In this case, the demagnetization should be considered and analyzed to calculate the flux density  $B_{core}$  in the rod.



**Fig. 2.19 A ferromagnetic bar without a magnetic field**

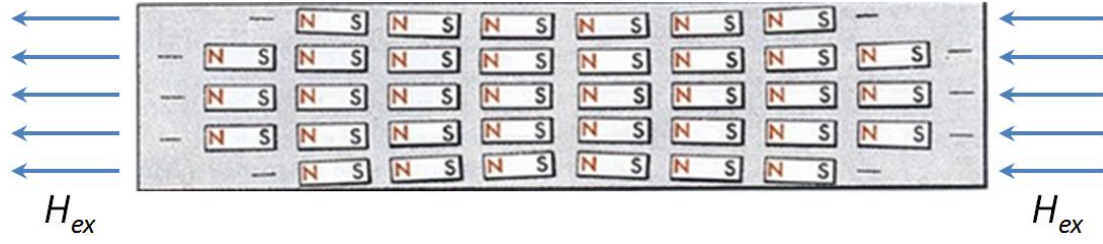


Fig. 2.20 A ferromagnetic bar with an external magnetic field

When a ferromagnetic rod is not magnetized, thousands of tiny magnets are randomly distributed inside as demonstrated in Fig. 2.19. When an external magnetic field  $H_{ex}$  is applied, tiny magnets are all oriented in the same direction as shown in Fig. 2.20. The poles of adjacent magnets cancel each other everywhere except at the end of the rod, leaving a surface layer of north poles on one end and south poles on the other. Magnetic fields always start from the north poles and end at the south poles. Thus, as shown in Fig. 2.21, a demagnetizing field  $H_d$  is generated which is against the external applied magnetic field  $H_{ex}$ . The magnetic field  $H_{core}$  in the core can be expressed by:

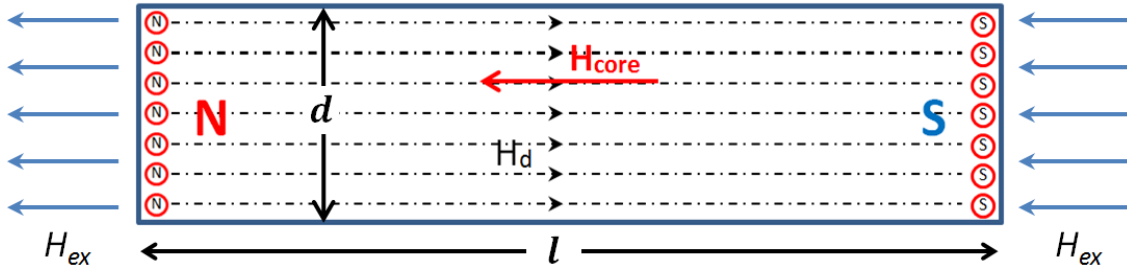


Fig. 2.21 The demagnetizing field inside a ferromagnetic rod

$$H_{core} = H_{ex} - H_d \quad (2.32)$$

The demagnetizing field  $H_d$  depends on two factors [13]: the magnetization  $M$  in the material (the surface pole strength) and the shape of the specimen (the pole distributions). The demagnetization factor  $D_M$  is introduced to describe the relationship between the demagnetizing field  $H_d$  and the magnetization  $M$ .

$$H_d = D_M \times M \quad (2.33)$$

The demagnetization factor  $D_M$  is solely determined by the specimen geometry [13]. The flux density  $B_{core}$  in the rod can be expressed by either  $H_{core}$  and  $H_{ex}$

$$B_{core} = H_{core}\mu_r\mu_0 = H_{ex}\mu_{eff}\mu_0 \quad (2.34)$$

According to Equation (2.13) and Equations (2.32) to (2.34), the effective permeability  $\mu_{eff}$  of an open core can be obtained:

$$\mu_{eff} = \frac{\mu_r}{1 + D_M(\mu_r - 1)} \quad (2.35)$$

When the relative permeability  $\mu_r$  is much bigger than 1,  $\mu_{eff}$  is solely dependent on the demagnetization factor  $D_M$  which is purely related to the core geometry. When a ferromagnetic rod can be made longer, the separation between the north poles and the south poles is increased which leads to a reduction in the demagnetizing field  $H_d$ . By making the rod thinner, fewer poles are generated at the two end surfaces which also reduces the demagnetizing field  $H_d$ . However, even for a uniform rod, it is very difficult to have an analytical expression for the calculation of the demagnetizing field  $H_d$  as well as the demagnetization factor  $D_M$  [15-17]. Chen *et al* built a 2D model to investigate the demagnetization factor  $D_M$  as a function of the length to diameter ratio  $\gamma$  [15].

$$\gamma = \frac{l}{d} \quad (2.36)$$

where  $l$  is the length of the rod in meters and  $d$  is the diameter of the rod shown in Fig. 2.21. According to the data in [13], the demagnetization factors for various core shapes are summarized in Table 2.3.

**Table 2.3 Demagnetization factors for various core shapes**

| Core geometry | Test conditions: ratio $\gamma$ | Demagnetization factor |
|---------------|---------------------------------|------------------------|
| Toroid        | N/A                             | 0                      |
| Cylinder      | $\gamma = \infty$               | 0                      |
| Cylinder      | $\gamma = 10$                   | 0.017                  |
| Cylinder      | $\gamma = 8$                    | 0.020                  |
| Cylinder      | $\gamma = 5$                    | 0.040                  |
| Sphere        | N/A                             | 0.333                  |



Similar to the two cases discussed above, if a ferromagnetic rod is placed in the same external magnetic field  $H_{ex}$  of 3.2 A/m, the magnetic flux density inside this rod  $B_{core}$  is plotted in Fig. 2.22 as a function of the relative permeability  $\mu_r$ . It is noted that a thinner and longer rod can have a high flux density  $B_{core}$  than a shorter and fatter one. Besides, compared to the toroid core, the flux density in the rod is much smaller when they have the same core material and placed in the same magnetic field  $H_{ex}$ . As a consequence, for a free-standing energy harvesting coil, the core shape has to be further optimized to achieve higher output power.

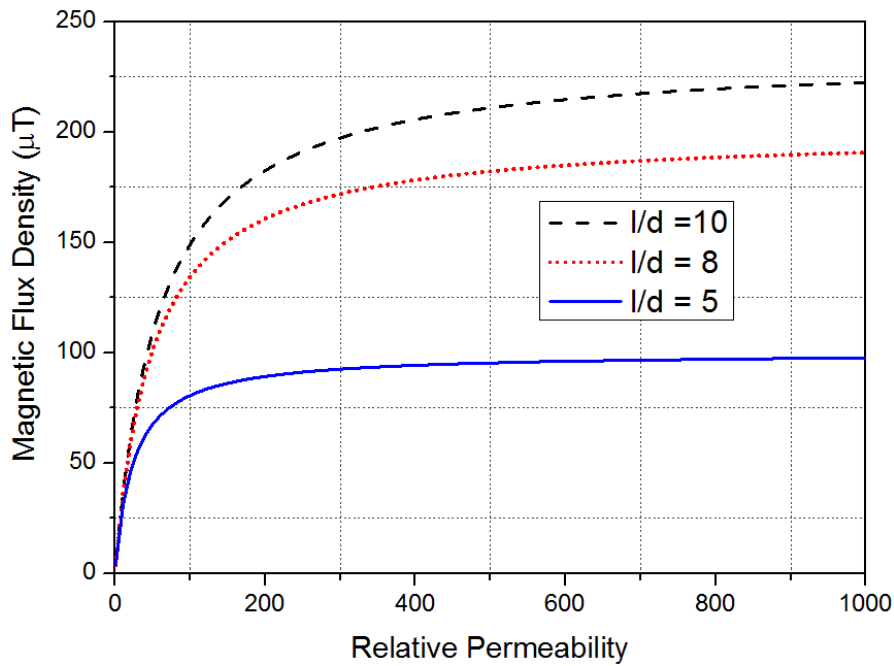


Fig. 2.22 The magnetic flux density  $B_{core}$  inside a rod as a function of the relative permeability

### 2.3.3 Energy Losses in a Ferromagnetic Core

When a ferromagnetic core is placed in a time-varying magnetic field, some of the power to be delivered to the load is lost in the core and dissipated as heat. In general, the core losses can be mainly divided into the hysteresis losses and eddy current losses.

The hysteresis phenomenon causes the magnetic flux density  $B_{core}$  in the core to lag behind the magnetic field  $H_{core}$  as shown in Fig. 2.12. For a free-standing energy harvester, the magnetic field in the core is relatively small due to the demagnetizing field. Furthermore, the frequency of the magnetic field (50/60 Hz) is extremely low. Therefore, the hysteresis losses

in this application are considerably low compared to the eddy current losses and therefore can be ignored.

When a time-varying magnetic field impinges on a conducting magnetic medium, eddy currents are generated which causes a dissipation of power. The power losses of the eddy current  $P_{ec}$  can be calculated by solving Maxwell's equations in a homogenous magnetic material of fixed permeability [13]. From Faraday's law of induction:

$$\nabla \times E = \frac{1}{A} \oint E dl = -\frac{dB_{core}}{dt} \quad (2.37)$$

Where  $E$  is the electric field in the core in V/m,  $l$  is the path of the eddy current in m,  $A$  is the effective area of the magnetic material in  $m^2$  and  $B_{core}$  is the flux density impinged on the material. If a magnetic flux impinges on a circular lamina with a radius of  $r$ , the eddy currents are shown in Fig. 2.23.

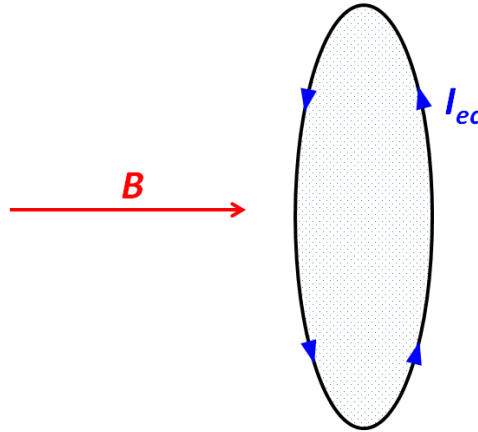


**Fig. 2.23 The magnetic flux density  $B_{core}$  impinges on a circular lamina**

$$\frac{1}{A} \oint E dl = \frac{2\pi r}{\pi r^2} E = -\frac{dB_{core}}{dt} \quad (2.38)$$

Assuming that the electric field  $E$  is uniform distributed,  $E$  can be expressed as a function of  $B_{core}$ :

$$E = -\frac{r}{2} \frac{dB_{core}}{dt} \quad (2.39)$$

The eddy current density  $J$  can be obtained by:

$$J = \frac{E}{\rho} = -\frac{r}{2\rho} \frac{dB_{core}}{dt} \quad (2.40)$$

where  $\rho$  is the resistivity of the material in  $\Omega\text{m}$ . The power losses can be calculated from the integral of the product of the current density  $J$  and the electric field  $E$  over the volume:

$$P_{ec} = \int_0^{r_0} JE(2\pi r)dr = \frac{\pi r^4}{8\rho} \left(\frac{dB_{core}}{dt}\right)^2 \quad (2.41)$$

In general, the classic power loss per unit volume of the eddy current  $S_{ec}$  can be expressed by:

$$S_{ec} = \frac{d^2}{2\beta\rho} \left(\frac{dB_{core}}{dt}\right)^2 \quad (2.42)$$

where  $d^2$  is the cross section area in  $\text{m}^2$ ,  $\beta$  is the shape factor, which has the value  $\beta = 6$  for laminations,  $\beta = 16$  for cylinders and  $\beta = 20$  for spheres. To reduce the eddy current losses, the resistivity of the ferromagnetic material should be maximized and the core shape needs to be optimized.

In summary, due to the small magnetic field in the core and the extremely low frequency, the hysteresis losses are considerably small compared to the eddy current losses. To reduce the eddy current, a core material with high resistivity should be used and the core shape needs to be optimized.

## 2.3.4 Circuit Design

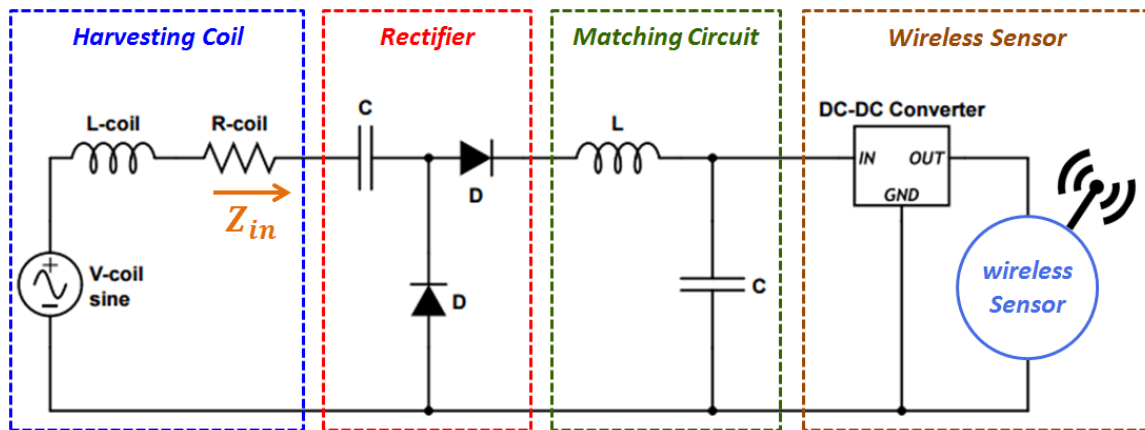


Fig. 2.24 A typical circuit topology for an energy harvesting system

The voltage waveform from a harvesting coil is a sine wave at the power frequency (50/60 Hz) and its amplitude changes with the surrounding magnetic field. However, the typical supply voltage for a commercial wireless sensor is a fixed DC voltage typically ranging 3.3 V to 5 V. Therefore, a circuit design is required to provide a stable voltage output to a wireless sensor. In addition, the impedance matching has to be considered to transfer the maximum energy from the harvesting coil to the wireless sensor.

A typical circuit mode used for energy harvesting is shown in Fig. 2.24. A rectifier is added to convert the AC signal to a DC value and the Schottky diode can be used to reduce the energy losses [18]. As shown in Fig. 2.10, to extract the maximum energy from the harvesting coil, the input impedance looking from the coil should be the complex conjugate of the coil impedance. Thus, a matching circuit is required to transfer the input impedance to a desired value. Finally, a DC-DC converter is applied to provide a stable output voltage and the wireless sensor can be powered up.

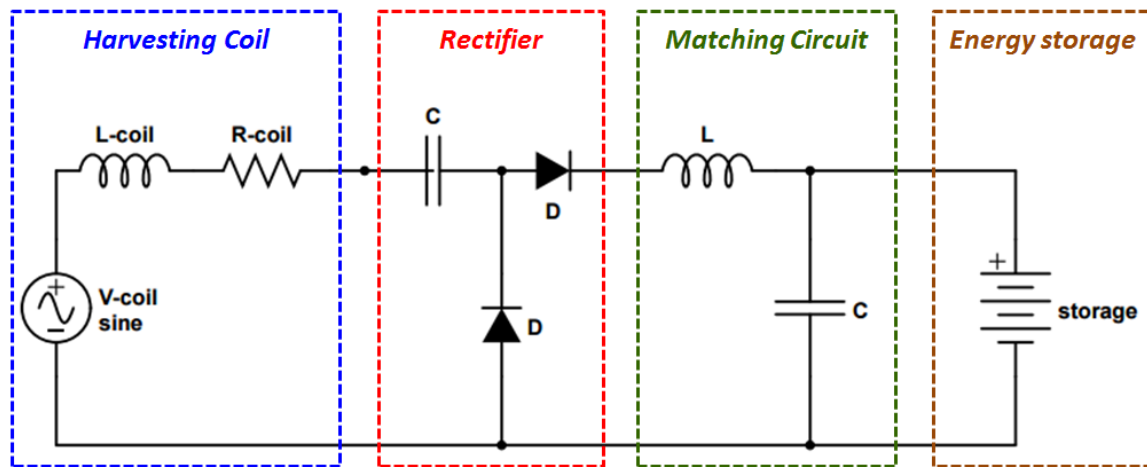


Fig. 2.25 The circuit diagram for charging an energy storage unit

However, in general cases, the power harvested by a free-standing magnetic field energy harvester is around several milliwatts or even smaller. For a typical wireless sensor, hundreds of milliwatts are required during its active operation [19]. Therefore, the energy collected by the coil should be stored in an energy storage unit (ESU) as shown in Fig 2.25. The ESU acts as a buffer stage to adapt for current surge from the wireless sensor. An energy management unit (EMU) shown in Fig 2.26 is used as a start-up circuit for the wireless sensor. It monitors and controls the energy in the ESU. Once the stored energy is larger than a certain level, the

wireless sensor is connected to the ESU via a DC-DC converter.

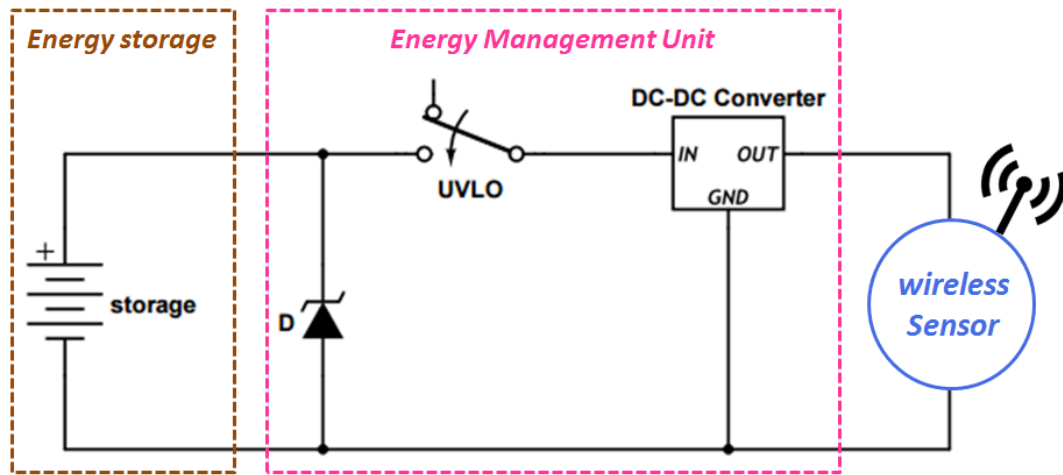


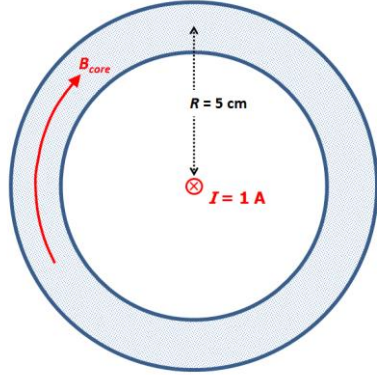
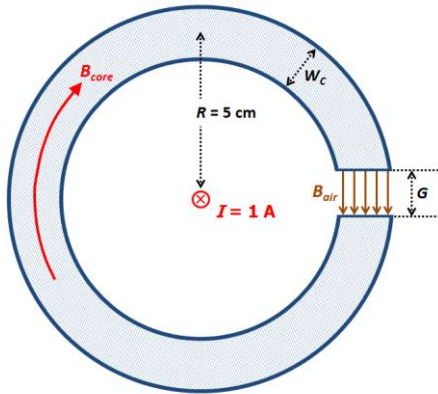
Fig. 2.26 The energy management unit

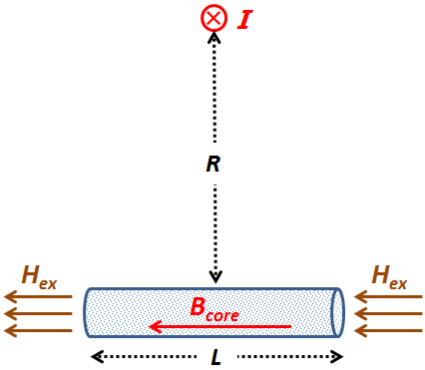
## 2.4 Summary

In this chapter, the magnetic flux density near the high voltage equipment has been investigated. From the results summarized in Table 2.1 and Table 2.2, a minimum magnetic flux density of  $7 \mu\text{T}_{rms}$  is available under overhead powers line or inside electrical substations.

The system overview of a free-standing magnetic field energy harvester has been presented and discussed. Three case studies have been provided to calculate the effective permeability of the cores with different shapes. The results are summarized in Table 2.5.

**Table 2.5 The effective permeability of various core shapes**

| Core shape               | Figure   | Effective permeability                                  |
|--------------------------|--|---|
| <b>Toroid</b>            |    | $\mu_{eff} = \mu_r$                                     |
| <b>Toroid with a gap</b> |  | $\mu_{eff} = \frac{2\pi R \mu_r}{2\pi R - G + G \mu_r}$ |

|                           |   |  |
|---------------------------|---|--|
| <p><b>Uniform rod</b></p> |  | $\mu_{eff} = \frac{\mu_r}{1 + D_M(\mu_r - 1)}$ |
|---------------------------|---|--|

The concept of the demagnetization in a ferromagnetic core has been explained in details and the core shape is the key factor to determine the effective permeability. The energy losses in the ferromagnetic core have been analysed and discussed. The eddy current losses could be reduced either by optimizing the core shape or using a core material with higher resistivity. Finally, a circuit structure has been proposed which utilizes the energy collected from the harvesting coil to power a wireless sensor.

## 2.5 References

- [1] "power systems loss: July 2011", *Powersystemsloss.blogspot.co.uk*, 2016. [Online]. Available: [http://powersystemsloss.blogspot.co.uk/2011\\_07\\_01\\_archive.html](http://powersystemsloss.blogspot.co.uk/2011_07_01_archive.html). [Accessed: 04-Apr- 2016].
- [2] National Grid, "Geometries of power lines | EMFs.info", *EMFs.info*, 2013. [Online]. Available: <http://www.emfs.info/sources/overhead/ohl-calculating/geometries/>. [Accessed: 04-Apr- 2016].
- [3] E. Lunca, M. Istrate, A. Salceanu and S. Tibuliac, "Computation of the magnetic field exposure from 110 kV overhead power lines", *2012 International Conference and Exposition on Electrical and Power Engineering*, 2012.
- [4] R. Olsen and P. Wong, "Characteristics of low frequency electric and magnetic fields in the vicinity of electric power lines", *IEEE Transactions on Power Delivery*, vol. 7, no. 4, pp. 2046-2055, 1992.
- [5] National Grid, "Height above ground | EMFs.info", *EMFs.info*, 2013. [Online]. Available: <http://www.emfs.info/sources/overhead/factors/height/>. [Accessed: 05-Apr- 2016].
- [6] D. Spoor and J. Roberts, "Development and experimental validation of a weather-based dynamic line rating system", *2011 IEEE PES Innovative Smart Grid Technologies*, 2011.
- [7] "National Grid substations | EMFs.info", *EMFs.info*, 2013. [Online]. Available: <http://www.emfs.info/sources/substations/substations-ng/>. [Accessed: 08-Apr- 2016].
- [8] I. Said, H. Hussain and V. Dave, "Characterization of magnetic field at distribution substations", *2010 9th International Conference on Environment and Electrical Engineering*, 2010.
- [9] K. Choma and M. Etezadi-Amoli, "Magnetic field measurements in a 345 kV substation", *2011 North American Power Symposium*, 2011.
- [10] A. Safigianni and C. Tsompanidou, "Electric- and Magnetic-Field Measurements in an Outdoor Electric Power Substation", *IEEE Transactions on Power Delivery*, vol. 24, no. 1, pp. 38-42, 2009.



- [11] J. Latva-Teikari, T. Karjanlahti, J. Kurikka-Oja, J. Elovaara, T. Langsjo and L. Korpinen, "Measuring occupational exposure to electric and magnetic fields at 400 kV substations", *2008 IEEE/PES Transmission and Distribution Conference and Exposition*, 2008.
- [12] "Magnetic materials ~ Pooza Creations", Poozacreations.blogspot.co.uk, 2012. [Online]. Available: <http://poozacreations.blogspot.co.uk/2012/04/magnetic-materials.html>. [Accessed: 08- Apr- 2016].
- [13] D. Jiles, "Introduction to Magnetism and Magnetics Materials", in *Magnetism*, 2<sup>nd</sup> ed. Ames, Iowa: Chapman & Hall, pp. 49-51, 1998
- [14] R. James, "Materials science: Magnetic alloys break the rules", *Nature*, vol. 521, no. 7552, pp. 298-299, 2015.
- [15] D. Chen, J. Brug and R. Goldfarb, "Demagnetizing factors for cylinders", *IEEE Transaction on Magnetics.*, vol. 27, no. 4, pp. 3601-3619, 1991.
- [16] Du-Xing Chen, E. Pardo and A. Sanchez, "Demagnetizing factors of rectangular prisms and ellipsoids", *IEEE Transaction on Magnetics.*, vol. 38, no. 4, pp. 1742-1752, 2002.
- [17] B. Pugh, D. Kramer and C. Chen, "Demagnetizing Factors for Various Geometries Precisely Determined Using 3-D Electromagnetic Field Simulation", *IEEE Transaction on Magnetics*, vol. 47, no. 10, pp. 4100-4103, 2011.
- [18] "BAT54 Series, Schottky Barrier Diodes", NXP Semiconductors, 2012. [Online]. Available: [http://www.nxp.com/documents/data\\_sheet/BAT54\\_SER.pdf](http://www.nxp.com/documents/data_sheet/BAT54_SER.pdf). [Accessed: 10- May- 2016].
- [19] Invisible-systems, 868 MHz Temperature & Pulse Transmitter, [Online]. <http://www.invisible-systems.com/Transmitters.php#temperature>. [Accessed: 10- May- 2016].

## **Chapter 3: The Development of a Bow-tie Coil**

### **3.1 Introduction**

For electric power transmission networks, high voltage overhead power lines are of great importance. Due to temperature variations, aging effects and ice accumulation [1, 2], the sag of the conductor may lead to dangerous circumstances and huge maintenance costs [3]. Hence, monitoring overhead power line conditions, disturbances, faults and sags is essential to ensure the proper operation of the power line transmission networks. Several critical parameters such as the ambient temperature and the line current may affect the operability and availability of overhead power lines. With the advancement in wireless communication technologies, inexpensive and ultra-low power wireless sensors have been developed and can be applied to monitoring these important parameters. However, the finite life span of the batteries which power the sensing system becomes a bottleneck as it is expensive to periodically replace these batteries. Thus, the energy harvesting technology is an attractive and promising solution to make the system monitoring self-sustainable [4].

As discussed in Chapter 1, solar panels and small wind turbines are good options to collect energy in good weather conditions [4, 5]. However, they also require additional high-capacity energy storage units which are normally expensive in order to work at night or when there are no winds available [3, 6]. Furthermore, harsh weather conditions like hail and storms could damage the turbine blades and solar panels [3, 7]. In the vicinity of high voltage power lines, a strong electromagnetic field is generated, which could be a consistent energy source for wireless sensors. Recently, a number of energy harvesting devices have been developed to collect the electrical [3, 8-12] or magnetic field energy from overhead power lines [13-17]. These devices are all wrapped on the power lines as shown in Fig. 3.1 to provide a range of wireless measurements such as conductor temperature, line sags and ambient temperature.

A limitation of all these designs is that the devices have to be mounted on overhead power lines. This limits the size and the weight of the sensors as it would further increase the line sag. The real-time weather data (such as wind speed, humidity and air temperature) near

overhead power lines is the foundation of the dynamic thermal rating technique, which could have a significant increase in the transmission capacity compared with the traditional static rating [18, 19]. Normally, the size of a weather station with a wind sensor is relatively large compared with temperature and humidity sensors [20]. Besides, it needs to be installed on a stationary object to keep it still. Therefore it is almost impractical to connect the weather station to a conventional energy harvester which is mounted on the power line. An energy harvesting device placed off the power lines, such as on the ground can overcome these shortcomings. Besides, this free-standing energy harvester can be easily combined with the solar pane or the wind turbine to form a reliable and efficient energy harvesting system. Zhu and colleagues designed a free standing capacitor to scavenge the electric field energy in a substation [21, 22]. However, the power output was limited due to the loading effect caused by the large impedance of the capacitor. Tashiro *et al* used Brooks coils to harvest the energy from the power line [15]. From their experiment, a power density of  $1.47 \mu\text{W}/\text{cm}^3$  was achieved in an area with the magnetic flux density of  $21.2 \mu\text{T}_{\text{rms}}$ . Their power density was limited due to the core shape and material. Roscoe *et al* designed a 50 cm long solenoid with a diameter of 5 cm to collect the magnetic field energy in a substation [23]. The power density in the coil was  $0.845 \mu\text{W}/\text{cm}^3$  when it was placed in a field of magnetic flux density of  $18.5 \mu\text{T}_{\text{rms}}$ . They selected cast iron as the coil core material which suffered greatly from the eddy current losses. This chapter provides a comprehensive study on the magnetic field energy harvester in terms of the coil geometrical shape, core material and wound method. Details on the coil designs and design equations are given in Section 3.2. In Section 3.3, the experiment evaluation of the proposed designs is presented. The discussion and conclusions are given in Section 3.4.

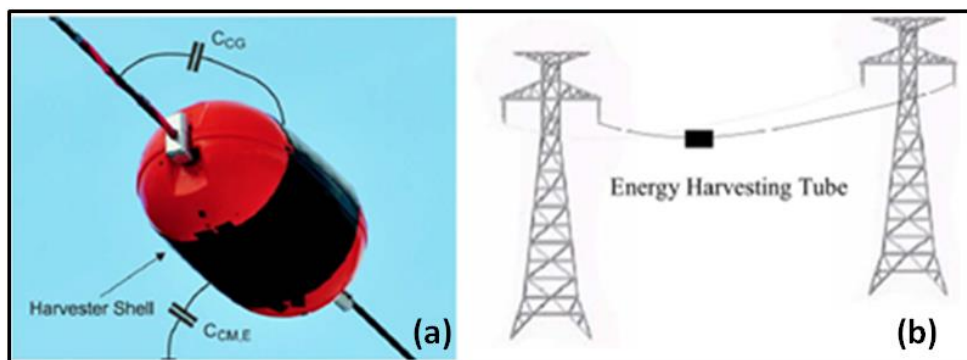


**Fig. 3.1** Energy harvesters mounted on the overhead power line. (a) from [10] and (b) from [11]

### 3.2 The Design and Analysis of the Bow-tie Coil

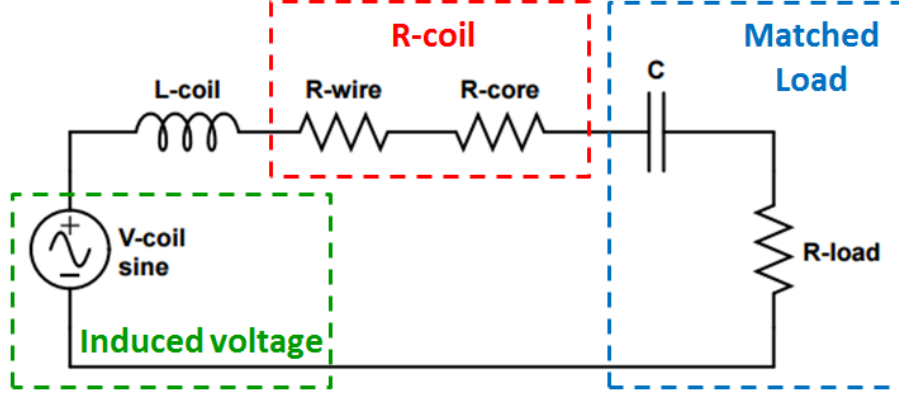


Fig. 3.2 The equivalent circuit of a free-standing energy harvester with a matched load.

At 50 Hz, the most efficient way to harvest the magnetic energy is to employ coils wrapped typically on ferromagnetic cores. Though the energy harvesting coil may be more than 10 meters away from the overhead power lines, it is still an inductive coupling system since the wavelength of the 50 Hz electromagnetic wave is extremely long. Therefore, the maximum power that the coil can harvest does not solely depend on the surrounding magnetic field, but also on such as the effective coil resistance and the optimized load. Fig. 3.2 shows the equivalent circuit of a harvesting coil connected with a compensating capacitor and a load resistor with the same value of  $R_{coil}$ . The induced coil voltage  $V_{coil}$  is a function of the surrounding magnetic flux density and the coil properties by applying Faraday's Law [23]:

$$V_{coil} = N\omega B_{ex}A\mu_{eff} \quad (3.1)$$

where  $V_{coil}$  is the peak value of the AC waveform,  $N$  is the number of turns wound on the coil,  $B_{ex}$  is the external magnetic flux density in T applied to the coil,  $A$  represents the effective cross section of the coil in  $m^2$ ,  $\omega$  is the angular frequency in rad/s and  $\mu_{eff}$  is the effective permeability related to the core material and core geometry.

The effective coil resistance  $R_{coil}$  consists of two parts: copper resistance and equivalent core resistance. The copper resistance is caused by the resistance of the long enameled wire wound on the core.

$$R_{copper} = \rho_{wire}l_{wire} \quad (3.2)$$

where  $\rho_{wire}$  is the wire resistance in  $\Omega$  per meter and  $l_{wire}$  is the total length of the enameled wire in m. When the core is subject to a time-varying magnetic field, some of the power to be delivered to the load is lost in the core and is dissipated as heat. These losses can be treated as the equivalent core resistance.

To provide the maximum power from the coil to the load, the maximum power transfer theory is applied. A compensating capacitor  $C = 1/(\omega^2 L_{coil})$  is added in series to the coil to eliminate the coil inductance  $L_{coil}$ . The load resistance  $R_{load}$  should be the same of the coil resistance. Under this condition, the power delivered to the load is calculated:

$$P_{load} = \left(\frac{V_{coil}}{2}\right)^2 / R_{coil} \quad (3.3)$$

The power density of this system can be derived as follow:

$$S_{power} = \frac{1}{4} \frac{V_{coil}^2}{R_{coil}} / Vol \quad (3.4)$$

where  $Vol$  is the total volume of the harvesting coil in  $m^3$ . To maximize the power output from the coil, its coil voltage  $V_{coil}$  should be increased while the coil resistance  $R_{coil}$  must be minimized. These two variables are correlated to the core shape, the core material and the properties of the enameled wires.

### 3.2.1 Optimum Core Shape Design

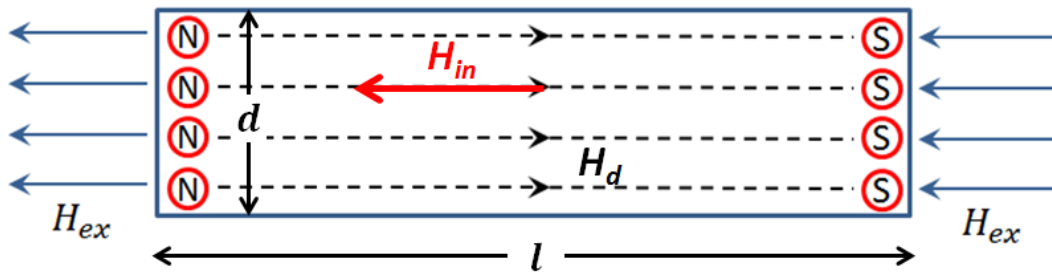


Fig. 3.3 The demagnetizing field  $H_d$  inside a ferromagnetic bar when applying an external magnetic field  $H_{ex}$

Since a free-standing coil cannot entirely enclose a current conductor, the demagnetization phenomenon appears during the magnetization process, which decreases the effective

permeability  $\mu_{eff}$ . When an external magnetic field  $H_{ex}$  is applied to the ferromagnetic rod/core as shown in Fig. 3.3, the north and south poles are created at two opposite sides, leading to the demagnetizing field  $H_d$ .

$$H_{in} = H_{ex} - H_d \quad (3.5)$$

The demagnetizing field  $H_d$  depends on two factors [24]: the magnetization in the material (the surface pole strength) and the shape of the specimen (the pole distribution). The demagnetization factor  $D_M$  is introduced to describe the relationship between the demagnetizing field  $H_d$  and the magnetization  $M$ .

$$H_d = D_M \times M \quad (3.6)$$

The demagnetization factor  $D_M$  is solely determined by the specimen geometry [24]. Thus the core shape needs to be optimized to reduce the demagnetization factor. Roscoe *et al* used a solenoid with a ferromagnetic core to harvest the magnetic field energy in a substation [23, 25]. They concluded that a thin long solenoid could have large effective permeability based on their experiment. However, a very long and thin solenoid may not be the best solution: although its volume may not be large, it can still occupy too much space because of its length. Furthermore, a long and thin ferromagnetic rod is brittle and prone to damage. We therefore propose a novel bow-tie-shaped core, shown in Fig. 3.4, which has a low demagnetization factor.

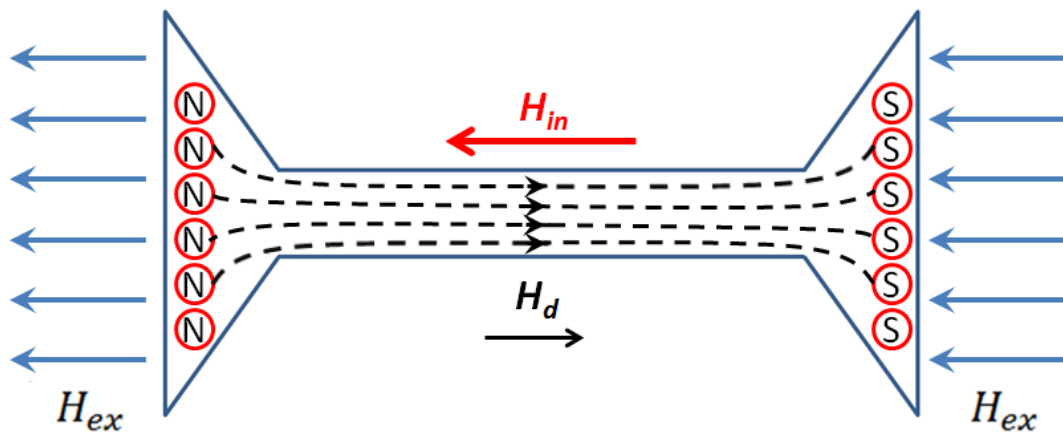


**Fig. 3.4** The demagnetizing field inside a bow-tie-shaped core when applying an external magnetic field

The two ends of the core have been broadened like a bow-tie. There are two main reasons for choosing this shape to reduce the demagnetization factor:

1. Based on Gauss's Law for magnetism, the larger surface areas at the both ends can guide more magnetic flux from the air into the ferromagnetic core. This intensifies the magnetization at the middle of the core where the wire is wound on.
2. When this bow-tie core is magnetized, the south and north poles are mainly formed at the end surfaces. As the surface has been increased, the separation between the south and north poles is therefore increased, which results in a reduction of the demagnetizing field at the middle of the bow-tie core.

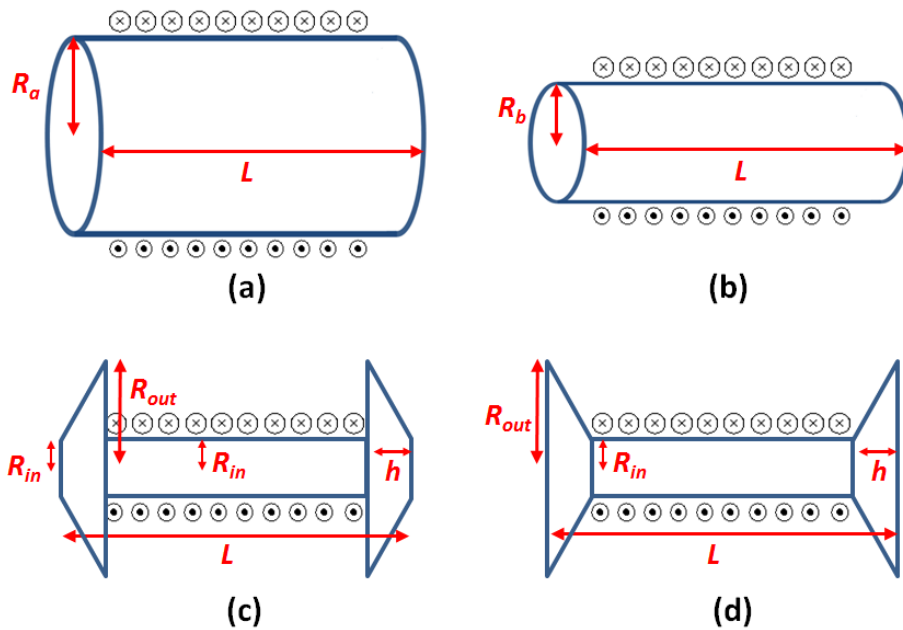


**Fig. 3.5** (a) The conventional solenoid with  $R_a = 5$  cm,  $L = 15$  cm. (b) the conventional solenoid with  $R_b = 2$  cm,  $L = 15$  cm. (c) the dumbbell core with  $R_{out} = 5$  cm,  $R_{in} = 1$  cm,  $h = 2.4$  cm and  $L = 15$  cm. (d) the bow-tie core with  $R_{out} = 5$  cm,  $R_{in} = 1$  cm,  $h = 2.4$  cm and  $L = 15$  cm

To verify these two arguments, four cores depicted in Fig. 3.5 have been tested in the same uniform magnetic field generated by a Helmholtz coil. All of them have the following configurations for comparison:

1. The same length of 15 cm;
2. An ideal magnetic core material with the relative permeability  $\mu_r$  and zero conductivity;
3. Winding numbers  $N=100$  on the core;

4. Placed in the same alternating magnetic field area ( $6 \mu T_{rms}$ ).

Solenoid (b), Dumbbell core (c) and Bow-tie core (d) have the same volume. The outer radius of Bow-tie core (d) equals to the radius of Solenoid (a). Dumbbell core (c) and Bow-tie core (d) have the same effective area that is orthogonal to the incoming magnetic field. Therefore, a fair comparison can be made to observe the effect on the different separations between the north poles and south poles. As the conductivity of the core material is intentionally set to zero, eddy currents can be eliminated inside the core. Therefore, we can focus on the magnetic properties with different core shapes. CST is used as the simulation tool. A large Helmholtz coil is built to generate a uniform magnetic field area where the core under test is placed. The boundary condition is set to “open” to emulate the free space.

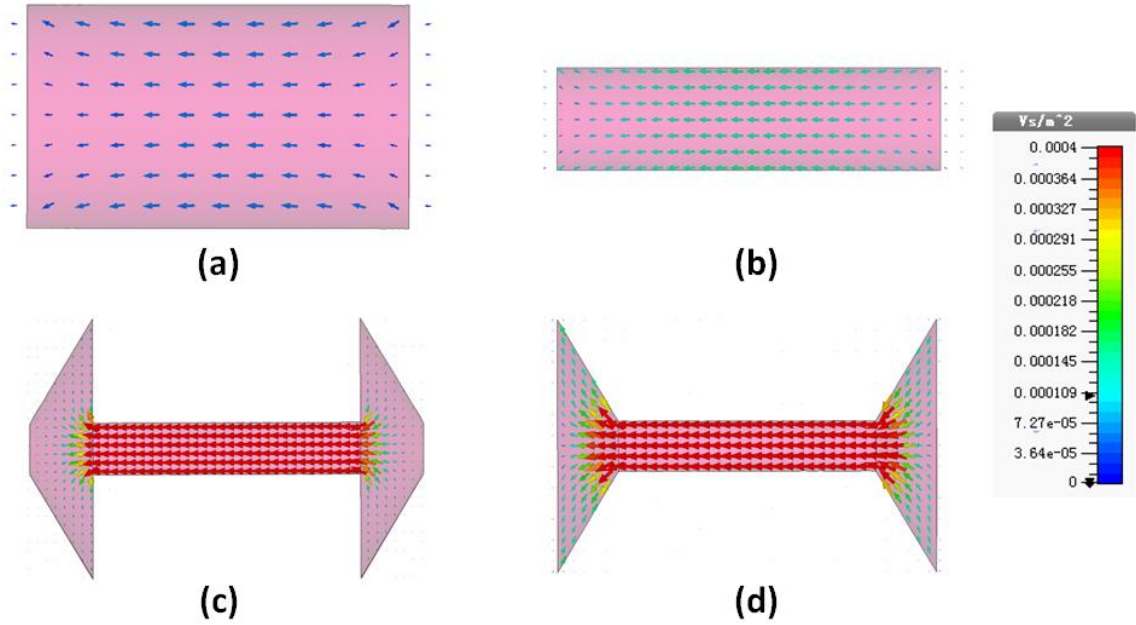


**Fig. 3.6** The magnetic flux density  $B_{in}$  inside the four cores when the external magnetic density of  $6 \mu T_{rms}$  is applied

Fig. 3.6 shows the simulated magnetic flux density  $B_{in}$  inside the four cores when the relative permeability  $\mu_r$  is configured to 2000. The magnetic flux density  $B_{in}'$  at the middle is  $785 \mu T_{rms}$  for Bow-tie core (d) and  $633 \mu T_{rms}$  for Dumbbell core (c), but only  $38.87 \mu T_{rms}$  for Solenoid (a) and  $110 \mu T_{rms}$  for Solenoid (b). This validates the first argument that the large end surface (but small middle section) will increase the magnetization intensity in the middle of the core. The effective permeability  $\mu_{eff}'$  and the fluxmetric demagnetization factor  $D'$  at



the middle of the core can be obtained using [1]:

$$\mu_{eff}' = B_{in}'/B_{ex} \quad (3.7)$$

$$D' = (\mu_r/\mu_{eff}' - 1)/(\mu_r - 1) \quad (3.8)$$

The fluxmetric demagnetization factors  $D'$  of Dumbbell core (c) and Bow-tie core (d) are found to be 0.009 and 0.007 respectively. The  $D'$  of Bow-tie core (d) is smaller than that of Dumbbell core (c), which validates the second argument that by increasing the separations between the north and south poles, the demagnetization factor can be reduced and therefore increase the power output.

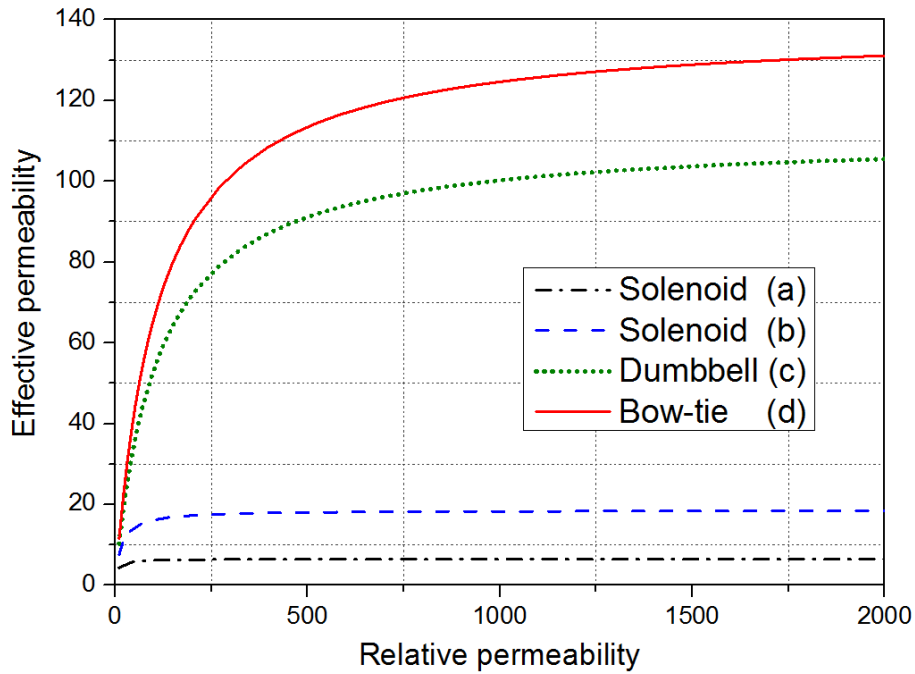


**Fig. 3.7** The effective permeability of four cores as a function of  $\mu_r$

It is also found that the effective permeability of Bow-tie core (d) is the highest among these four testing cores, as shown in Fig. 3.7. The  $\mu_{eff}'$  of Solenoid (b) is 2 times bigger than that of Solenoid (a) which validates the concept discussed in [23, 25]. Furthermore, four curves become saturated as  $\mu_r$  increases. For the curves of Solenoid (a) and (b), their knee points appear when  $\mu_r$  approaches 100. In contrast, for the curve of the bow-tie core, its knee point is around 300 and the effective permeability increased with  $\mu_r$ , though the slope is small. However, the power density of the harvesting coil depends not only on  $\mu_{eff}'$ , but also on the effective cross section area and the coil resistance. As the ideal core material has been used,

the coil resistance is determined by the copper resistance. If an enameled wire with the diameter of 0.14 mm and the wire resistance of 1.11  $\Omega/\text{m}$  is used, the copper resistance is calculated and shown in Table 3.1.

**TABLE 3.1 The parameters of the three cores when  $\mu_r = 2,000$  and  $N = 100$**

| Core Type                                  | Solenoid (a) | Solenoid (b) | Dumbbell (c) | Bow-tie (d) |
|--|--------------|--------------|--------------|-------------|
| Effective permeability                     | 6.48         | 18.33        | 105.51       | 130.81      |
| Demagnetization factor                     | 0.154        | 0.0540       | 0.009        | 0.007       |
| Open circuit voltage ( $\text{mV}_{rms}$ ) | 8.61         | 3.54         | 6.09         | 7.54        |
| Wire resistance ( $\Omega$ )               | 34.87        | 13.94        | 6.97         | 6.97        |
| Output power ( $\mu\text{W}$ )             | 0.53         | 0.23         | 1.33         | 2.04        |
| Power density ( $\text{nW}/\text{cm}^3$ )  | 0.45         | 1.19         | 7.04         | 10.82       |

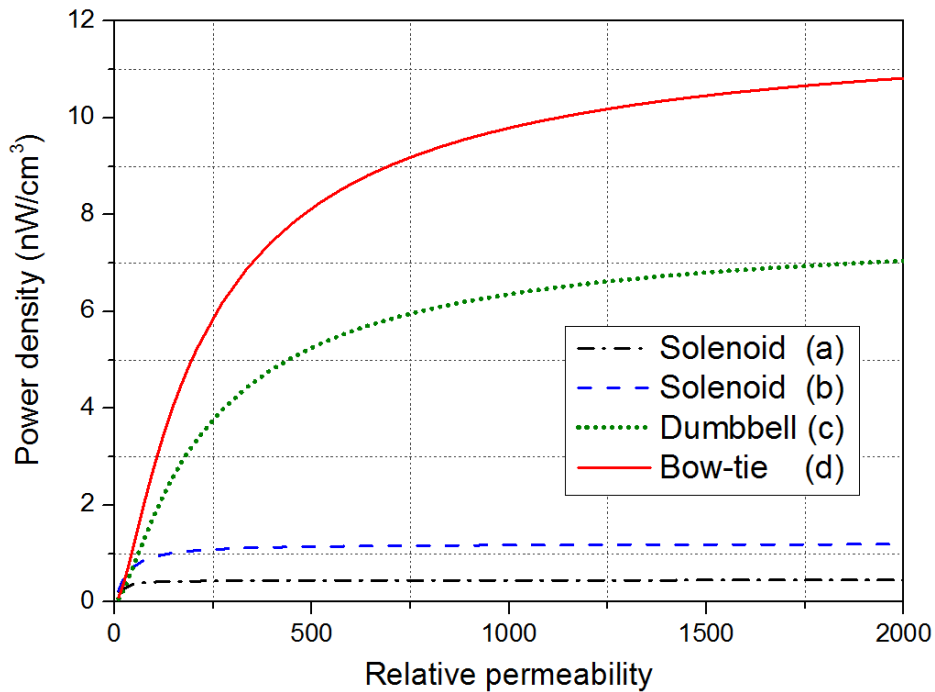


**Fig. 3.8 The power density of four cores as a function of  $\mu_r$  when  $N$  is 100**

According to Equations (3) and (4), the power density of the four cores is plotted in Fig. 3.8 as a function of the relative permeability  $\mu_r$ . As shown in Table 3.1, the bow-tie core has the smallest copper resistance due to its small inner radius  $R_{in}$ , which leads to the largest output

power though its volume is much smaller than Solenoid (a). The output powers are low due to the small number of turns. The relationship between the winding properties and the output power will be discussed later. As shown in Fig. 3.8, when  $\mu_r = 2000$ , the power density of the Bow-tie core (d) is 1.5 times as much as that of Dumbbell core (c) and 8 times bigger than Solenoid (b). As a consequence, the bow-tie-shaped core shows the best performance compared with other cores.

A parametric study has been conducted on the bow-tie core to maximize the output power when the volume and the length are fixed. The outer radius  $R_{out}$  and the inner radius  $R_{in}$  are tuned in a certain range, while the height  $h$  is configured accordingly to keep the core volume and length unchanged. In theory, when the outer radius  $R_{out}$  is increased, more magnetic flux can be guided into the core and the surface poles formed at the two ends are separated even further. Therefore, a larger outer radius may generate a higher voltage. Fig. 3.9 shows the simulation results. As the inner radius  $R_{in}$  increases, the coil voltage increases slightly. Nevertheless, a smaller inner radius will have lower copper resistance. When the outer radius  $R_{out}$  increases, the voltage increases significantly as shown in Fig. 3.9. As a consequence, a bow-tie core with a larger outer radius  $R_{out}$  and smaller inner radius  $R_{in}$  could have a higher power density as shown in Fig. 3.10.

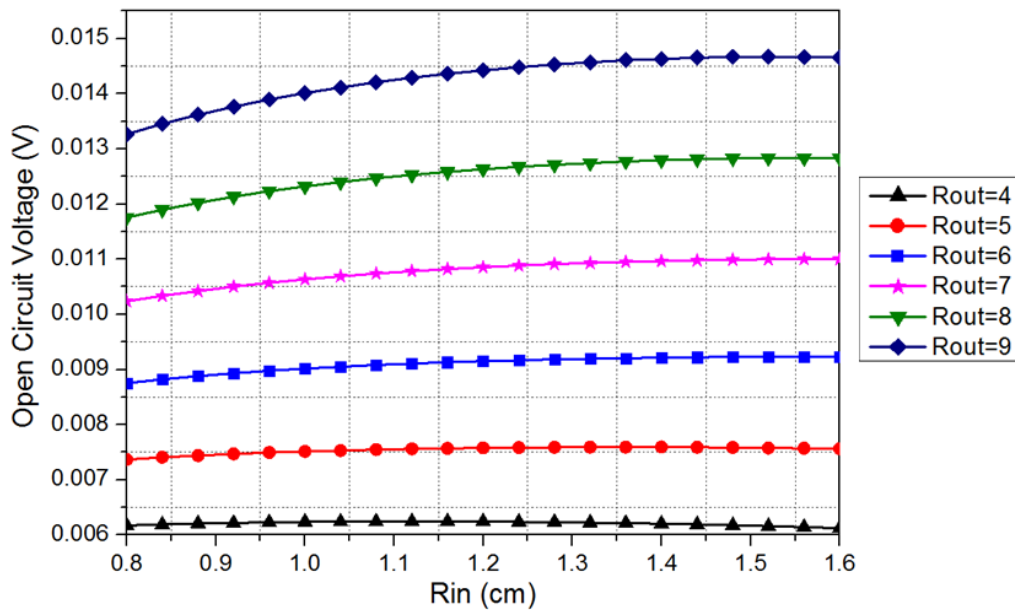


Fig. 3.9 The open circuit voltage of the bow-tie core with different inner radius  $R_{in}$  and outer radius  $R_{out}$

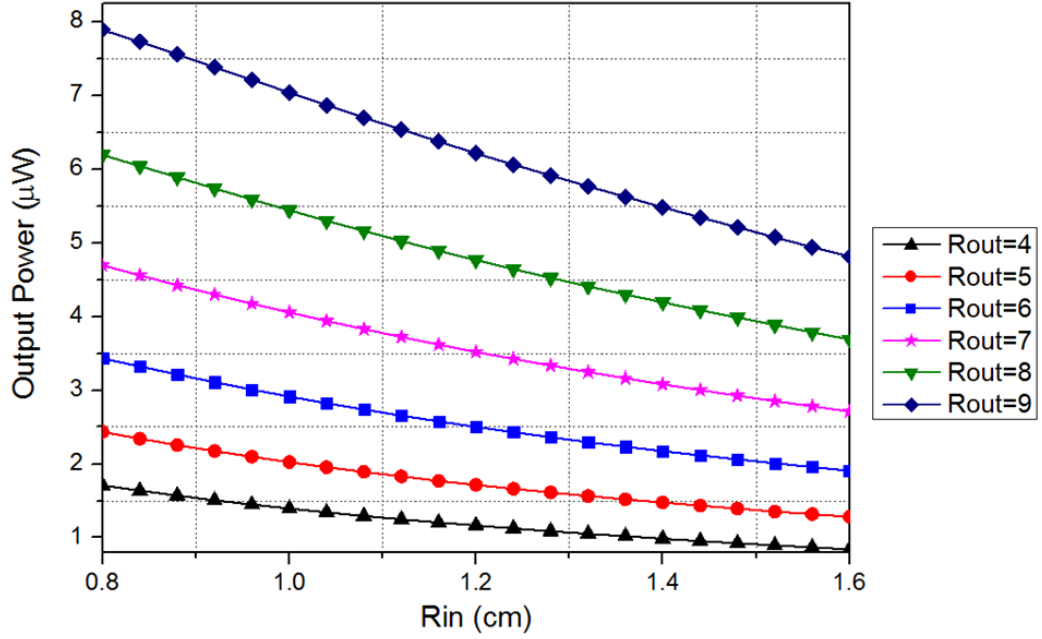


Fig. 3.10 The output power of the bow-tie core with different inner radius  $R_{in}$  and outer radius  $R_{out}$

### 3.2.2 Core Material Selection

It is important to note that the core material can have a huge effect on the performance of the harvesting coil. In [35], a research was conducted on harvesting magnetic field energy with different core materials. It was concluded that nanocrystalline alloy (FeSiB) was the most suitable material which has very high relative permeability ( $\mu_r = 8,000 \sim 40,000$ ) and saturation magnetization. However, they did not consider the case that the harvesting coil could not entirely enclose the conducting current. As depicted in Fig. 3.7, due to the demagnetization factor, the effective permeability  $\mu_{eff}$  becomes saturated when the relative permeability  $\mu_r$  is higher than about 400. Therefore, ultra high  $\mu_r$  would not provide a significant increment on the  $\mu_{eff}$ . Instead, it is more important to focus on the reduction of the core losses. In general, the core losses can be divided into hysteresis losses and eddy current losses. By using the soft ferromagnetic material with low coercivity, the hysteresis losses in this application are considerably smaller than the eddy current losses due to the weak magnetic field and extremely low frequency. Roscoe *et al* used cast iron as the core material and the device suffered greatly from eddy current losses [23, 25]. Their measurement results

showed that the effective coil resistance was up to 33 k $\Omega$ , dominated by the eddy current losses. As a consequence, the eddy current must be minimized to maximize the power output delivered to the load. According to [24], the equation to calculate the power consumption of the eddy current losses is:

$$w_{eddy} = \frac{S}{2k\rho} \left( \frac{dB_{in}}{dt} \right)^2 \quad (3.9)$$

where  $S$  is the cross section area in m<sup>2</sup>;  $B_{in}$  is the magnetic flux density inside the core in T;  $\rho$  is the material resistivity in  $\Omega\text{m}$  and  $k$  is the shape factor. We use stainless steel as the reference core material for the bow-tie coil shown in Fig. 3.3, whose relative permeability is close to 2,000 and conductivity is around  $2.17 \times 10^6$  S/m. Since the core material becomes conductive, eddy currents are generated when it is placed in an alternating magnetic field. The simulation indicates that the open circuit voltage is reduced to 5.9 mV compared with 7.6 mV when the conductivity is zero. Fig. 3.11(a) shows the eddy current density in the cross section at the middle of a bow-tie coil with  $R_{out} = 5$  cm,  $R_{in} = 1.5$  cm,  $h = 1.4$  cm and  $L = 15$  cm. At the edge of the core, the current density can be higher than 500 A/m<sup>2</sup>. These eddy currents generate the magnetic field, which is against the external applied magnetic field.

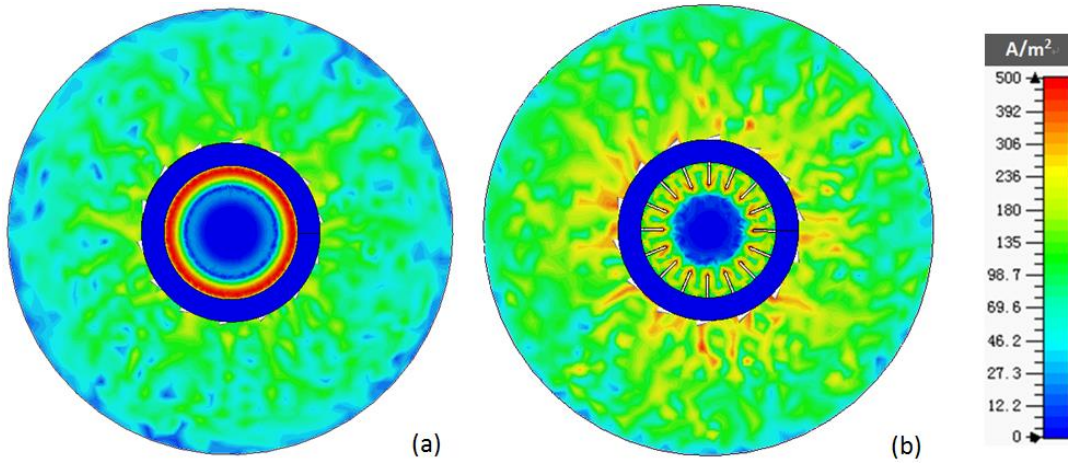


**Fig. 3.11 The eddy current density inside the core when  $\mu_r = 2,000$  and the conductivity  $\sigma = 2.17 \times 10^6$  S/m:**  
(a) The original core, (b) The core with air gaps

To reduce the eddy current, the shape factor  $k$  was studied. Analogous to the core lamination used in the transformer, several air gaps have been introduced to the center rod as shown in Fig. 3.12. The simulation result depicted in Fig. 3.11(b) shows that the average current

density inside the core is now reduced to  $52 \text{ A/m}^2$ . When more air gaps are introduced, the eddy current can be further reduced.

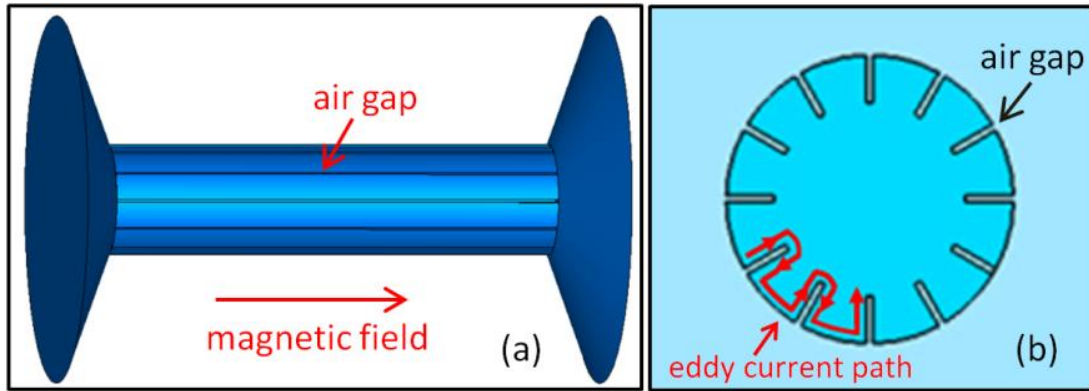


**Fig. 3.12** The air gaps inside the bow-tie core: (a) External view, (b) Cross section view from the middle of the core

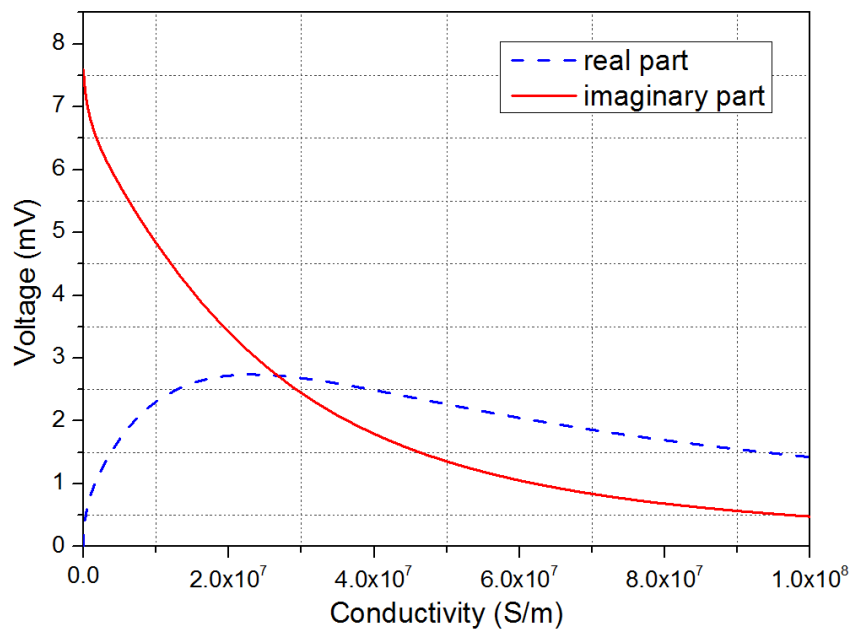


**Fig. 3.13** The complex open circuit voltage of the bow-tie coil as a function of the core conductivity when the relative permeability is 2,000.

If only several air gaps are introduced, the eddy current is still significant. The material conductivity is investigated and Fig. 3.13 plots the complex open circuit voltage of the bow-tie coil as a function of the core conductivity. When the conductivity is zero, the open circuit voltage only contains imaginary part which represents the voltage that can be coupled to the load. When the conductivity increases from zero, the real part of the open circuit voltage

appears caused by the eddy current losses inside the core, which is finally dissipated as heat. As the conductivity further increases, the real part can be higher than the imaginary part, which means most of the power is wasted in the core rather than delivered to the load. Thus we should have the conductivity as small as possible.

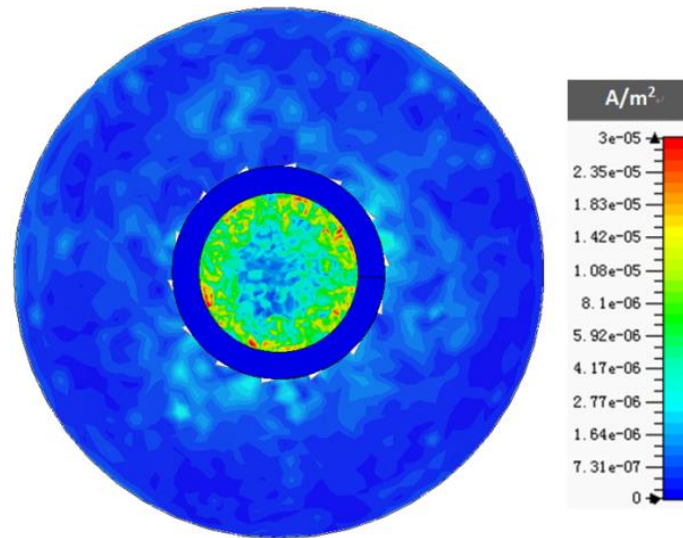


**Fig. 3.14** The eddy current density inside the core with the relative permeability of 2000 and the conductivity of 0.35 S/m

To summarize, the correct core material should have two main properties:

1. Soft ferromagnetic material with relative permeability above 400;
2. Minimal conductivity.

A ferrite seems to be the most suitable material according to these requirements. Mn-Zn soft ferrite could have relative permeability between 2,000 to 18,000 and ultra-low conductivity below 0.5 S/m [26]. In comparison, the conductivity of nanocrystalline alloy is normally higher than  $7 \times 10^5$  S/m. When a ferrite is used as the core material, the current density becomes several micro amperes per square meter in our case, as shown in Fig. 3.14. As a consequence, the eddy current is reduced significantly and the majority of the energy can be delivered to the load.



### 3.2.3 Optimum Winding Method

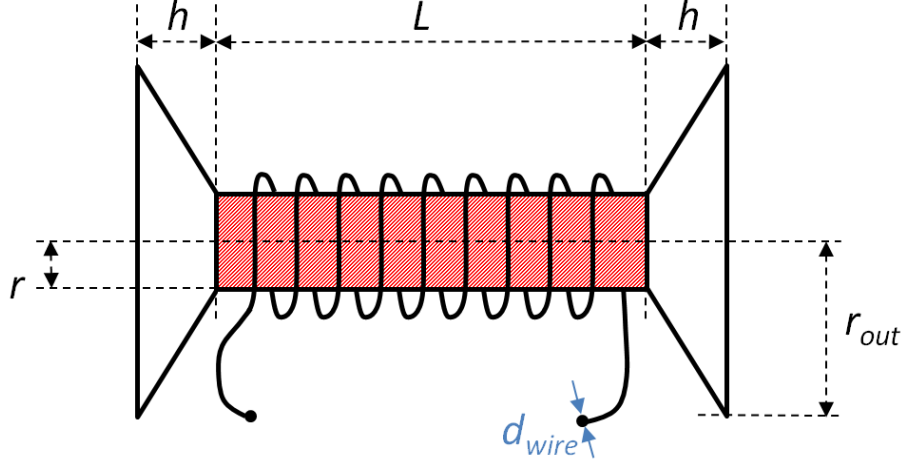


**Fig. 3.15** The physical dimensions of the bow-tie coil.  $R_{out}$  and  $r$  is the outer and inner radius.  $d_{wire}$  indicates the diameter of the enameled wires wound on the core.  $L$  represents the length of the center rod around which the wires are wrapped.

The bow-tie coil can be treated as a solenoid with length  $L$  and radius  $r$ , leaving the average effective permeability  $\mu_{eff}$  unchanged because the wires are only wrapped around the middle part of the core as shown in Fig. 3.15. The open circuit voltage can be obtained by applying Faraday's Law:

$$V_{coil} = N\pi r^2 \omega \mu_{eff} B_{ex} \quad (3.10)$$

The equivalent coil resistance  $R_{coil}$  can be divided into copper losses and core losses:

$$R_{coil} = R_{copper} + R_{core} \quad (3.11)$$

As the ferrite is selected as the core material, the core losses are considerably smaller compared with the copper losses when the number of winding turns  $N$  is sufficiently large:

$$R_{coil} \approx R_{copper} \quad (3.12)$$

There should be several layers of the enameled wire wrapped around the core as a large number of winding turns are needed to acquire a high coil voltage.

$$K_{layer} = N/(L/d_{wire}) \quad (3.13)$$

The total length  $l_{wire}$  of the enameled wire can be obtained as a function of the number of turns  $N$ :



$$l_{wire} = \left( \frac{r + r + K_{layer} \times d_{wire}}{2} \right) 2\pi N \quad (3.14)$$

Using Equations (2), (11) and (12), the copper resistance can be derived as:

$$R_{copper} = 2\pi r N \rho_{wire} + \pi N^2 d_{wire}^2 \rho_{wire} / L \quad (3.15)$$

According to (10) and (15), the power delivered to the matched load can be obtained as:

$$P_{load} = N\pi (r^2 \omega \mu_{eff} B_{ex})^2 / \left( 8r \rho_{wire} + \frac{4\rho_{wire} N d_{wire}^2}{L} \right) \quad (3.16)$$

The power output is dependent upon the property of the enameled wires in addition to the core shape and material. A higher winding number  $N$  could generate a higher voltage but could also produce a larger copper resistance. The enameled wire with a larger diameter has lower wire resistance but occupies more space. The properties of the enameled wire should be fully investigated to boost the power output from the coil.

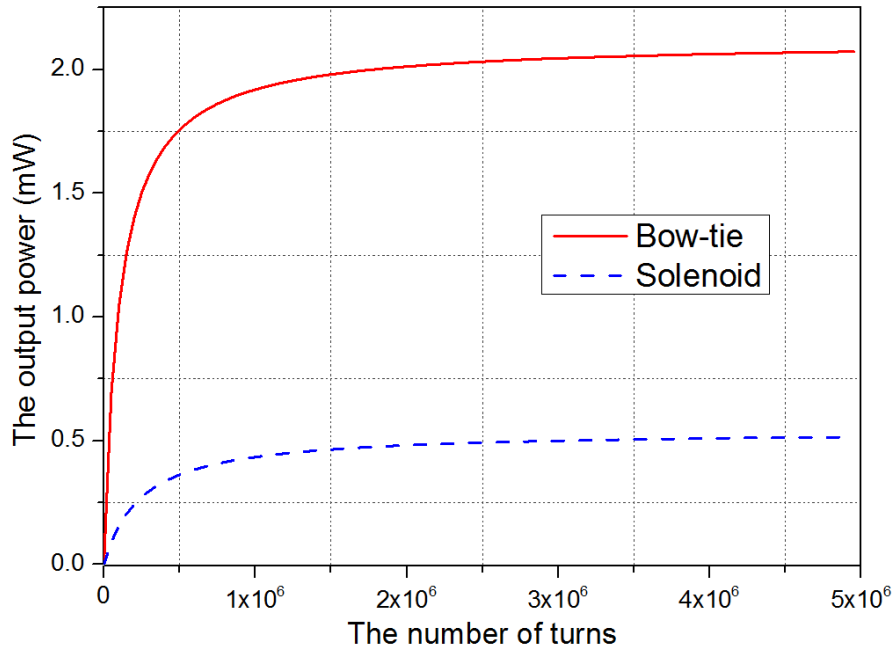


**Fig. 3.16 The power output as a function of the winding number**

Firstly, the enameled wire with the fixed diameter of 0.14 mm and the wire resistance of 1.11  $\Omega/m$  is wound on the ferrite core shown in Fig. 3.5(d). The power output is plotted in Fig. 3.16 as a function of the winding number, which indicates that the power output of the two coils increases with the increment of the winding number. However, when the number of

turns is extremely large, the power becomes saturated as there are too many layers on the core. In this situation, each turn added on the core requires much longer wires and results in larger resistance. In practical, it is impossible to wind 1,000,000 turns of enameled wire on such a small core.

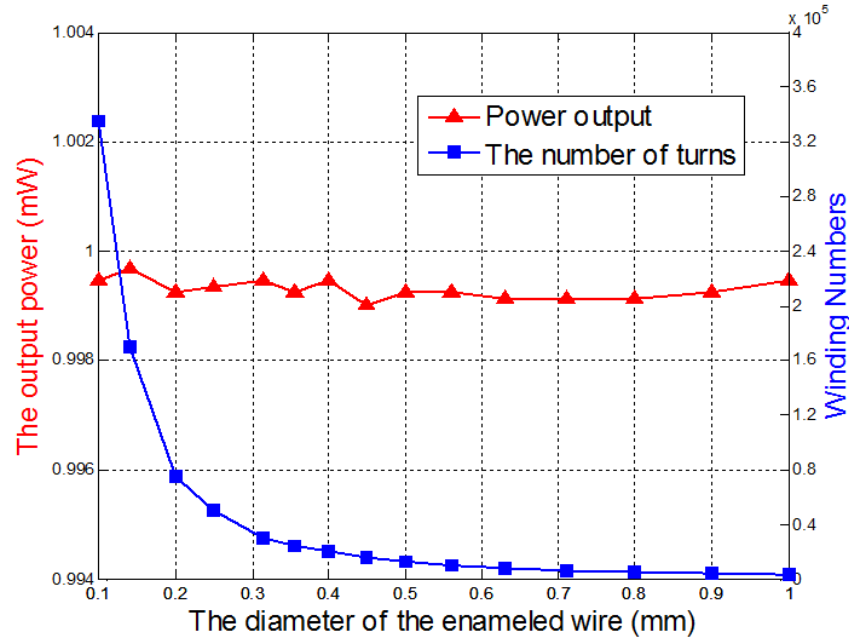


**Fig. 3.17 The power output of the bow-tie coil when different wires are used**

Secondly, by giving a fixed space of  $8 \times 10^{-4} \text{ m}^3$ , the wires with different diameters [27] are fully wound on the bow-tie core and their corresponding power output is plotted in Fig. 3.17. As the diameter increases, the number of turns decreases due to the fixed space while the power output does not change significantly. Therefore, the output power from the coil does not depend on the type of the enameled wire used but depends on the volume that the enameled wire occupies. From the financial point of view, the wire with a larger diameter is preferred as its unit price is cheaper. From the power delivery point of view, the enameled wire with a smaller diameter is better which can obtain a higher winding number and result in a higher coil voltage. When the coil is connected to a rectifier circuit, high coil voltage could lower the power dissipation on the rectifying diode, which increases the power transfer efficiency.

In conclusion, to increase the output power from the energy harvesting system, thin wires are preferred and the number of winding turns should be as large as possible.

### 3.3 Measurement Results and Discussions

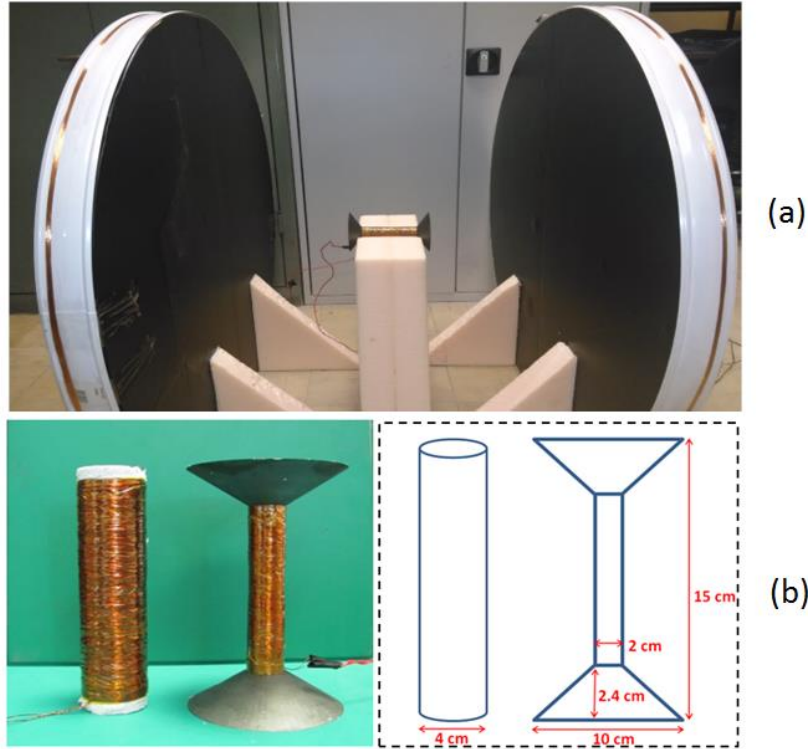


**Fig. 3.18 (a) A Helmholtz coil used to generate a uniform magnetic flux density in the laboratory, (b) The solenoid and the bow-tie coil made by ferrite with the given dimension**

A Helmholtz coil (consisting of two identical coil rings) is made to generate a uniform magnetic field to imitate the environment under overhead power lines. The diameter of each coil ring is 1 meter with 33 turns of conducting wire on it and the two coil rings are separated by half a meter. With a  $120 \text{ mA}_{\text{rms}}$  current passing through the Helmholtz coil, a magnetic flux density of  $7 \text{ } \mu\text{T}_{\text{rms}}$  is generated. A bow-tie coil and a solenoid with the same volume and length are fabricated. The specimens and their dimensions are shown in the Fig. 3.18(b). Mn-Zn ferrite [28] is used as the core material with relative permeability  $2300 \pm 25\%$  and conductivity of  $0.154 \text{ S/m}$ . Two coils are put into the Helmholtz coil and their open circuit voltages are measured using a multimeter. The results are compared against the simulated ones as shown in Fig. 3.19. From the measurement results, the voltage of the bow-tie coil is 1.5 times of that of the solenoid. This validates the concepts discussed in the previous section. It is noted that the simulation results are higher than the experiment values. This should be mainly caused by the errors in the fabricated ferrite core. First, the relative permeability of

the ferrite is in the range of 1700 to 2900 according to the datasheet [28], which may bring some uncertainty into the experiment. Secondly, due to the special geometry of the bow-tie coil, it is difficult and expensive to manufacture this whole ferrite core in one piece. Instead, five pieces are fabricated and then glued together as shown in Fig. 3.20. Therefore, gaps may exist in each contact surface. In this situation, the magnetic flux in the core and the effective permeability are reduced because more energy is required to drive the same flux across the air gap than through an equal volume of the ferrite [24]. As the air gap increases, the effective permeability will be further reduced. When a 0.05 mm air gap is introduced, the simulation results show that the average effective permeability decreases from 128 to 108 and its corresponding coil voltages are close to the measured values.

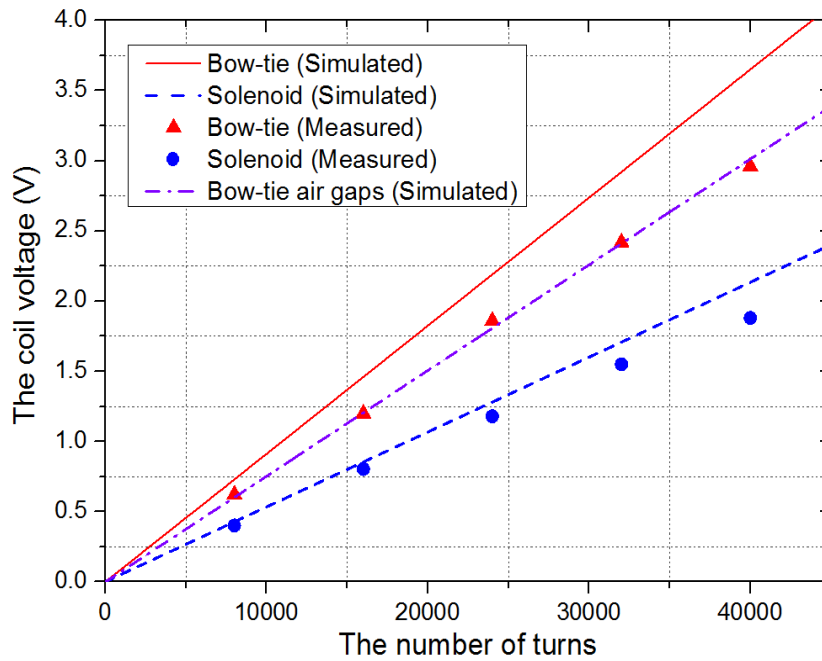


Fig. 3.19 The measurement results of the open circuit voltage as a function of the winding numbers.

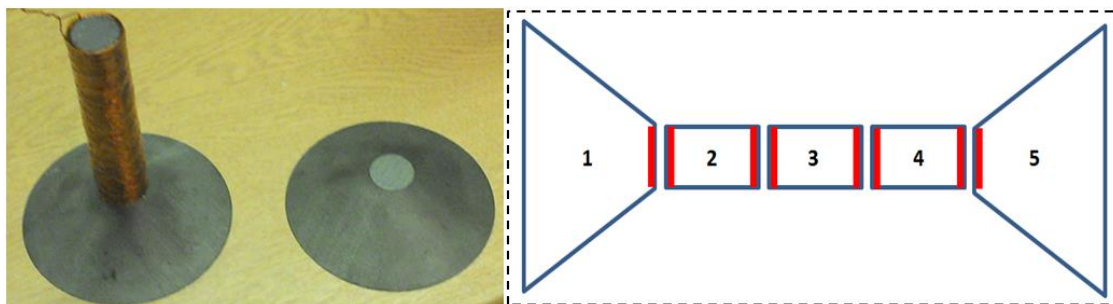
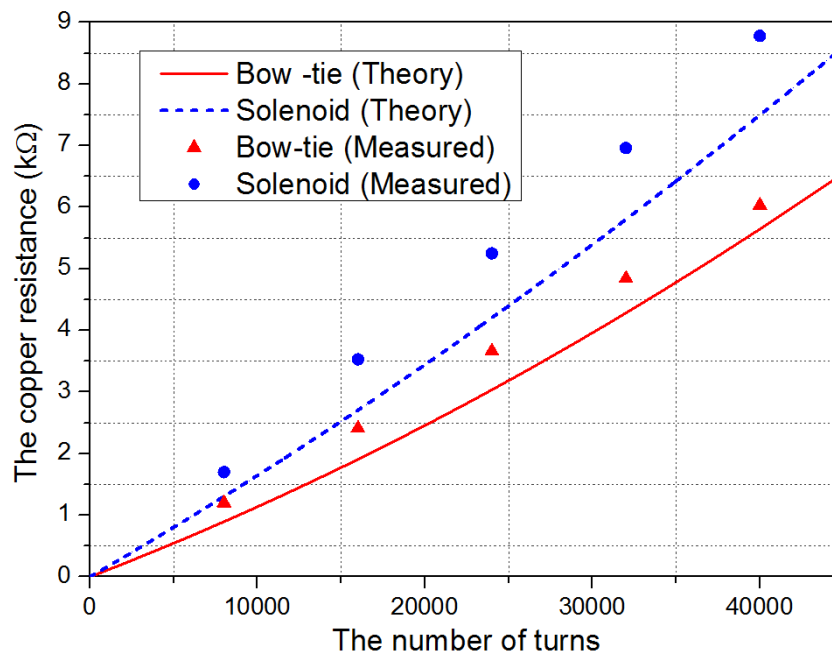


Fig. 3.20 The bow-tie coil fabricated in 5 small piece and then glued together

The effective coil resistance can be measured by a 50 Hz bridge. The power output at the load can be maximized by tuning the capacitor and the load resistance. In this situation, based on the maximum power transfer theory, the effective coil resistance should be the same as the load resistance. The copper resistance is measured with a multi-meter and results are included in Table 3.2. They indicate the copper resistance dominates the effective coil resistance, proving that the eddy current losses are minimized. The measurement results are then compared to the theoretical values as shown in Fig. 3.21.

**TABLE 3.2 The measurement results of the effective coil resistance**

| Coil Type    | Windings | R-wire ( $k\Omega$ ) | R-coil ( $k\Omega$ ) |
|--------------|----------|----------------------|----------------------|
| Solenoid     | 8,000    | 1.69                 | 1.70                 |
| Bow-tie Coil | 8,000    | 1.09                 | 1.2                  |
| Solenoid     | 24,000   | 5.28                 | 5.25                 |
| Bow-tie Coil | 24,000   | 3.72                 | 3.66                 |
| Solenoid     | 40,000   | 8.63                 | 8.78                 |
| Bow-tie Coil | 40,000   | 5.95                 | 6.03                 |



**Fig. 3.21. The copper resistance of the two coils as a function of the winding numbers.**

For the same winding numbers, the copper resistance of the bow-tie coil is smaller than that of the solenoid. As for this novel bow-tie coil, the copper wire is wound around its middle part where the radius is small. Hence, the same number of turns can be achieved with a short enameled wire which results in a smaller copper resistance. The measured values are higher than the theoretical values. Since the two coils are not wound by a fully automatic coil winding machine due to the requirement of special fixtures. Therefore windings are not perfectly aligned which causes a longer wire to achieve the same number of turns and results in the difference between the measured and theoretical values. To wind 40,000 turns on the bow-tie core shown in Fig. 3.18(b), in the ideal situation when the enameled wire is perfectly aligned, the winding diameter shown in Fig. 3.22 would be 4.74 cm. However, the measurement result is 5.5 cm which means a longer wire was used in practice.

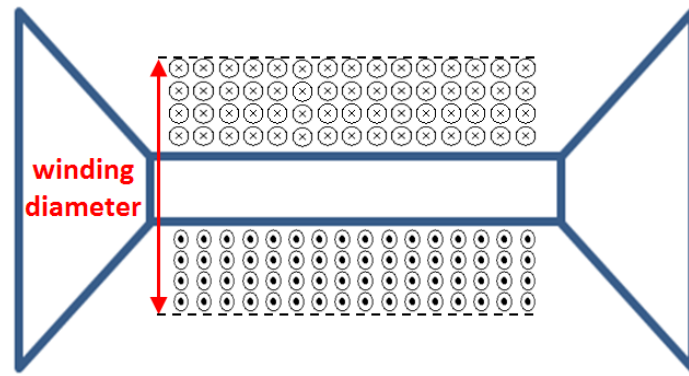


**Fig. 3.22. The winding diameter of a bow-tie coil**

When the air gap model is used to describe the coil voltage, the theoretical values align with the experimental results. The measurement results indicate that the power output from the bow-tie coil can be 2.5 times greater than the output from the conventional solenoid with 40,000 turns. In this case, the power density of the bow-tie coil is  $1.86 \mu\text{W}/\text{cm}^3$  compared to  $0.53 \mu\text{W}/\text{cm}^3$  from the solenoid when placed in a magnetic flux density of  $7 \mu\text{T}_{\text{rms}}$ .

For a fixed space of  $8 \times 10^{-4} \text{ m}^3$ , three different enameled wires have been selected to fully wind on the bow-tie core. Their parameters and output powers are shown in Table 3.3. As expected, the output power does not change much for different wires although other parameters are changed significantly in Table 3.3.

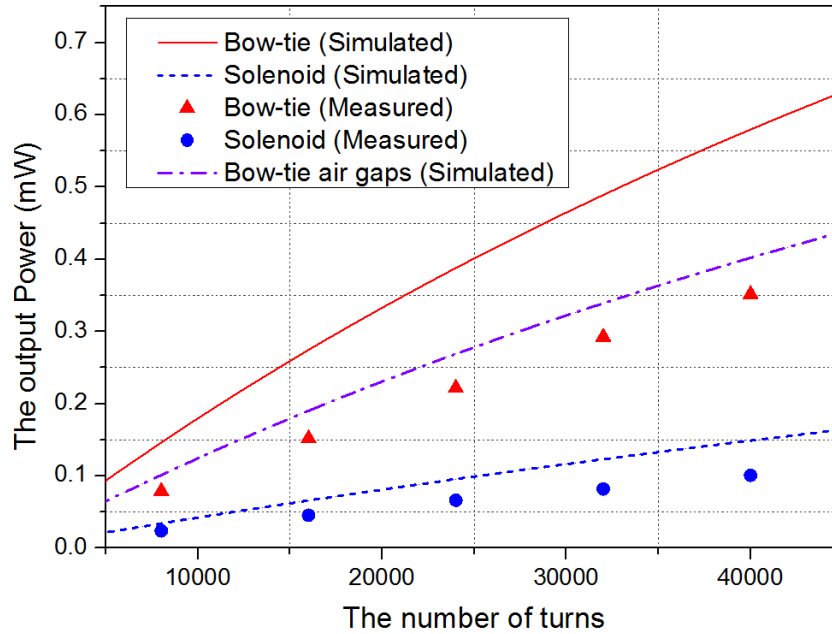


Fig. 3.23 The power output of the two coils as a function of the winding numbers.

TABLE 3.3 The measurement results of the coil output with different wires

| Wire Type                        | 0.14 mm | 0.49 mm | 1.00 mm |
|----------------------------------|---------|---------|---------|
| Resistance ( $\Omega/\text{m}$ ) | 54.41   | 2.176   | 0.544   |
| Number of turns                  | 103,060 | 9,500   | 2,430   |
| Coil voltage ( $V_{rms}$ )       | 8.36    | 0.730   | 0.181   |
| Coil resistance ( $\Omega$ )     | 21500   | 160.2   | 10.1    |
| Power (mW)                       | 0.8127  | 0.831   | 0.811   |

From the experiment, 360  $\mu\text{W}$  was collected at the load by using the bow-tie coil with 40,000 turns, which might be enough to power a small wireless sensor [29]. To boost the power output from the coil for energy hungry sensors, three methods have been considered:

1. To increase the length and the outer radius of the bow-tie coil to increase the effective permeability.
2. To put the coil closer to the power line to increase the external magnetic flux density.
3. To increase the number of winding turns.

If the length and the outer radius of the bow-tie coil can be made larger as shown in Fig. 3.24, the average effective permeability can be increased from 128 to 615. If we wind 160,000 turns of enameled wires with the diameter of 0.14 mm on the core and place the coil 5 meters above the ground where the magnetic flux density is typically around 11  $\mu\text{T}$ , in this situation, the estimated output power is around 146.7 mW which gives the estimated power density of  $103.5 \mu\text{W}/\text{cm}^3$ . This value is comparable to a  $30 \text{ cm} \times 30 \text{ cm}$  solar panel working during a cloudy day [30], but the solar panel does not work at night unlike the proposed solution.

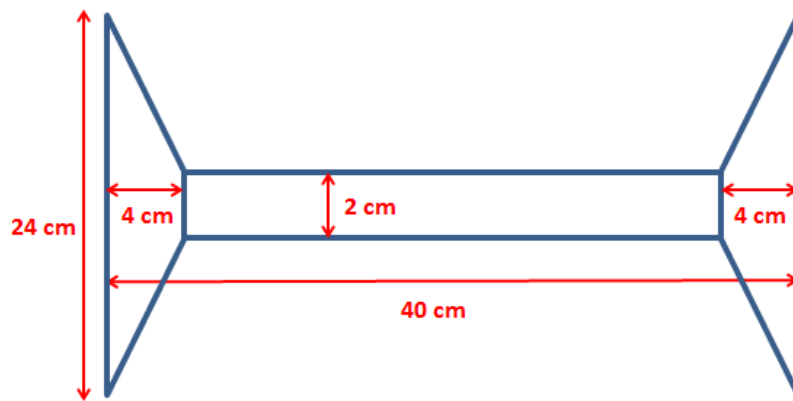


**Fig. 3.24 The bow-tie coil with longer length and larger outer radius**

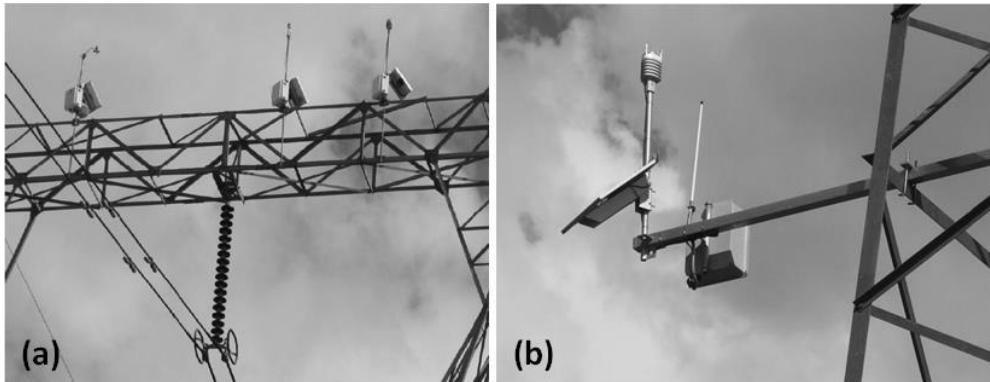


**Fig. 3.25. Installation of weather stations on a pylon. (a). on the top of the pylon. (b) on the anti-climbing protective device**

The power consumption of a typical weather station [31] and a GPRS data logger [32] is 36 mW and 3.6W respectively. If the weather station collects the data in every 30 minutes and the data logger takes a maximum of 1 minute to transmit the information to the server, the average power consumption would be 120 mW. The dynamic thermal rating [33, 34] suggested the weather station should be installed either on top of the pylon or on the anti-



climbing protective device as shown in Fig. 3.25 [33]. In both situations, the height to the ground is larger than 5 meters. This means that the large bow-tie coil shown in Fig. 3.24 is able to power the weather station and the data logger.

The bow-tie coil proposed in this thesis is compared with other recently reported designs. Roscoe *et al* designed a 50 cm long solenoid with the diameter of 5 cm to collect the magnetic field energy in a substation [23]. The power density of their coil was only  $0.845 \mu\text{W}/\text{cm}^3$  when it was placed in a magnetic flux density of  $18.5 \mu\text{T}_{\text{rms}}$ . If the bow-tie coil designed in this thesis was placed in the same magnetic flux density with the same winding number, the power density would be  $13.0 \mu\text{W}/\text{cm}^3$ , which is 15 times more than their design. In addition, their coil is longer and bigger than our bow-tie coil.

### 3.4 Summary

In this chapter, a new and efficient harvesting coil to scavenge the magnetic field energy under overhead power lines has been proposed and presented. The coil does not need to be clamped to the power line and can be placed just above the ground, thus sensors with a larger volume can be powered which is impossible for the conventional method of mounting the energy harvester on the power lines.

A novel bow-tie coil has been introduced, designed and optimized to produce a much higher power density ( $1.86 \mu\text{W}/\text{cm}^3$ ) than the conventional solenoid design ( $0.53 \mu\text{W}/\text{cm}^3$ ). This was based on the theoretical analysis and subsequently verified by the experiment measurements. The special design of its geometric shape and a good selection of the core material have led to much greater effective permeability and lower loss resistance. The core material was selected specifically to eliminate eddy current losses. Ferrite was identified as the most suitable core material, given its high relative permeability and ultra-low conductivity. Different winding methods have been investigated. The results indicated that the power collected by the coil was not only determined by the types of the enameled wire, but also proportional to volume that the wire occupied. However, the wire with a smaller diameter can have higher energy transfer efficiency. It was demonstrated that the power density of the bow-tie coil designed in this thesis was 15 times greater than a recently reported result if both coils were placed into the same magnetic field (our coil was smaller). Thus the proposed solution is extremely efficient and flexible on harvesting energy under overhead power lines and can be used to power a range of sensors.

### 3.5 References

- [1] M. Lacroix, L. Brouillette, and A. Blais, “Hydro Quebec’s de-icing system: Automated overhead line monitoring and de-icing system”, in *Proc.CIFRE*, 2008, pp. B2–211.
- [2] K. Savadjiev and M. Farazaneh, “Modeling of icing and ice shedding on overhead power lines based on statistical analysis of meteorological data”, *IEEE Transactions on Power Delivery*, vol. 19, no. 2, pp. 715–722, 2004
- [3] H. Zangl, T. Bretterkieber and G. Brasseur, “A Feasibility Study on Autonomous Online Condition Monitoring of High-Voltage Overhead Power Lines”, *IEEE Transactions on Instrumentation and Measurement*, vol. 50, no. 5, pp. 1789-1796, 2009
- [4] V. Raghunathan, A. Kansal, J. Hsu, J. Friedman, Mani Srivastava, “Design considerations for solar energy harvesting wireless embedded systems,” *Information Processing in Sensor Networks*, pp. 457-462, 2005
- [5] S. Bader, B. Oelmann, “Enabling Battery-Less Wireless Sensor Operation Using Solar Energy Harvesting at Locations with Limited Solar Radiation,” *4<sup>th</sup> Int. conf. on Sensor Technologies and Applications (SENSORCOMM)*, pp. 602-608), 2010
- [6] J. A. Paradiso and T. Starner, “Energy Scavenging for Mobile and Wireless Electronics”, *IEEE Pervasive Computing*, vol. 4, pp.18-27, 2005
- [7] C. Tsai, C. Hsieh, S. Huang, “Enhancement of Damage-Detection of Wind Turbine Blades Via CWT-Based Approaches”, *IEEE Transactions on Energy Conversion*, vol. 21, no. 3, pp. 776-781, 2006
- [8] K. Chang, S. Kang, K. Park and S. Shin, “Electric Field Energy Harvesting Powered Wireless Sensors for Smart Grid”, *Journal of Electrical Engineering & Technology*, vol. 7, no. 1, pp. 75~80, 2012
- [9] T. Keutel, X. Zhao and O. Kanoun, “Energy Scavenging for Monitoring of Overhead Power Line Networks”, in *Proc. IMTC*, pp. 207-211, 2009

- [10] M. J. Moser, T. Bretterklieber, H. Zangl and G. Brasseur, “Strong and Weak Electric Field Interfering: Capacitive Icing Detection and Capacitive Energy Harvesting on a 220-kV High-Voltage Overhead Power Line”, *IEEE Transaction on Industrial Electronics*, vol. 58, no. 7, pp. 2597-2604, 2011
- [11] F. Guo, H. Hayat, and J. Wang, “Energy Harvesting Devices for High Voltage Transmission Line Monitoring”, *Power and Energy Society General Meeting*, July, pp. 1-8, 2011
- [12] X. Zhao, T. Keutel and M. Balduaf, “Energy harvesting for a wireless-monitoring system of overhead high-voltage power lines”, *IET Generation, Transmission & Distribution*, vol. 7, issue: 2, pp. 101-107, 2013
- [13] J. Moon, S.B. Leeb, “Analysis Model for Magnetic Energy Harvesters”, *IEEE Transactions of Power Electronics*, vol.30, issue: 8, pp. 4302-4311, 2015
- [14] R. Moghe, D. Divan, F. Lambert, “Powering Low-Cost Utility Sensors using Energy Harvesting”, *Power Electronics and Applications (EPE 2011)*, in *Proc. 2011-14th European Conference*, pp. 1-10, 2011
- [15] K. Tashiro, H. Wakiwaka, S. Inoue, and Y. Uchiyama, “Energy Harvesting of Magnetic Power-Line Noise”, *IEEE Transactions on Magnetics*, vol. 47, issue: 10, pp. 4441-4444, 2010
- [16] J.P. Amaro, “Energy harvesting for Zigbee compliant Wireless Sensor Network nodes”, *IECON 2012 - 38th Annual Conference on IEEE Industrial Electronics Society*, pp. 2583-2588, 2012
- [17] T. Taithongchai and Ekachai, “Adaptive Electromagnetic Energy Harvesting Circuit for Wireless Sensor Application”, *Electrical Engineering/Electronics, Computer, Telecommunications and Information Technology*, pp. 278-281, 2009
- [18] C. Li, G. Ma and B. Qi, “Condition Monitoring and Diagnosis of High-Voltage Equipment in China –Recent Progress”, *IEEE Electrical Insulation Magazine*, vol. 29, issue: 5, pp. 71-78, 2013

- [19] D.M. Green, J.P. Gentle and K.S. Myers, "A Comparison of Real-Time Thermal Rating Systems in the U.S. and the U.K.", *IEEE Transactions on Power Delivery*, vol. 29, issue: 4, pp. 1849-1858, 2014
- [20] Vaisala, Vaisala Weather Transmitter WXT520 Access to Real Time Weather Data, <http://www.vaisala.com/Vaisala%20Documents/Brochures%20and%20Datasheets/WEA-MET-WXT520-Weather-datasheet-B210417EN-K-LOW.pdf>, 2014
- [21] M. Zhu and M.D. Judd, "Energy Harvesting in Substations for Powering Autonomous Sensors", *Third International Conference on Sensor Technologies and Applications*, pp. 246-251, 2009
- [22] M. Zhu and P.C. Baker, "Alternative Power Sources for Autonomous Sensors in High Voltage Plant", *2009 IEEE Electrical Insulation Conference*, 2009, pp. 36-40, 2009
- [23] N. M. Roscoe and M. D. Judd, "Harvesting Energy from Magnetic Fields to Power Condition Monitoring Sensors", *IEEE Sensors Journal*, vol. 13, issue: 6, pp. 2263-2270, 2013
- [24] D. Jiles, "Introduction to Magnetism and Magnetism Materials", in *Magnetism*, 2<sup>nd</sup> ed. Ames, Iowa: Chapman & Hall, pp. 49-51, 1998
- [25] N. Roscoe and M. Judd, "Optimization of Voltage Doublers for Energy Harvesting Applications", *IEEE Sensors Journal*, vol. 13, no. 12, pp. 4904-4911, 2013.
- [26] Ferroxcube soft Mn-Zn ferrite cores, datasheet available at <http://www.ferroxcube.com/FerroxcubeCorporateReception/datasheet/sfemisup.pdf>, 2015
- [27] Enameled wires, Data Table for Solid Round Wire, <http://www.williamsonsonic.com/WireTable/index.html>, 2010
- [28] Mn-Zn ferrite, DMR40 Material Characteristics, datasheet available at [www.chinadmegc.com/material\\_download.php?6](http://www.chinadmegc.com/material_download.php?6), 2013
- [29] MICAz wireless sensor, (MPR2400) 2.4 GHz Mote, <http://www.memsic.com/products/wireless-sensor-networks/wirelessmodules.html>,

2013

- [30] K. Tashiro, H. Wakiwaka, S. Inoue, and Y. Uchiyama, "Energy Harvesting of Magnetic Power-Line Noise", *IEEE Transactions on Magnetics*, vol. 47, issue: 10, pp. 4441-4444, 2010
- [31] Vaisala, Vaisala Weather Transmitter WXT520 Access to Real Time Weather Data, <http://www.vaisala.com/Vaisala%20Documents/Brochures%20and%20Datasheets/WEA-MET-WXT520-Weather-datasheet-B210417EN-K-LOW.pdf>, 2014
- [32] Invisible-systems, Gateway GPRS, GPS & RF, <http://www.invisible-systems.com/solutions/pdf/Gateway%20GPRS%20GPS%20RF.pdf>, 2015
- [33] D. J. Spoor and J. P. Roberts, "Development and Experimental Validation of a Weather-Based Dynamic Line Rating System", *IEEE Innovative Smart Grid Technologies Asia (ISGT)*, pp. 1-7, 2011
- [34] M. Matus, D. Saez and M. Favley, "Identification of Critical Spans for Monitoring Systems in Dynamic Thermal Rating", *IEEE Transactions on Power Delivery*, vol. 27, no. 2, pp. 1002-1009, 2012
- [35] M. dos Santos, D. Vieira, Y. Rodriguez, C. Souza, T. Moraes and R. Freire, "Energy harvesting using magnetic induction considering different core materials", *2014 IEEE International Instrumentation and Measurement Technology Conference (I2MTC) Proceedings*, 2014.

## **Chapter 4: The Development of a Helical Coil**

### **4.1 Introduction**

In Chapter 3, a bow-tie-shaped coil is proposed as a free-standing magnetic field energy harvester [1]. Unlike the conventional cable-clamped energy harvester [2-6], a free-standing coil can be installed in any place as long as there is an alternating magnetic field. As a result, it can be used to power a wide range of monitoring sensors which are critical for many smart grid applications [7-16].

In this chapter, a more efficient free-standing magnetic field energy harvester is proposed where the path of the magnetic flux in its new helical core can be lengthened dramatically so that the demagnetization factor is much reduced. Therefore, the magnetic flux density in the core can be significantly increased and more power can be collected. The design details of this energy harvester are presented in Section 4.2. In Section 4.3, the parameters of the helical core are studied. In Section 4.4, the experiment evaluations of the proposed design are presented. The discussions and conclusions are given in Section 4.5.

## 4.2 The Design and Analysis of the Helical Coil

### 4.2.1 Optimum Core Shape Design

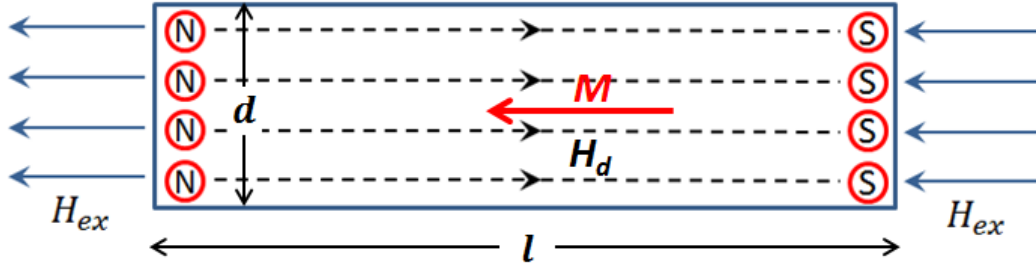


Fig. 4.1. The demagnetizing field  $H_d$  inside a ferromagnetic rod when applying an external magnetic field  $H_{ex}$

As discussed in Chapter 2 and 3, the effective permeability  $\mu_{eff}$  is an important parameter which can affect the induced voltage and the power output significantly. The power can be reduced dramatically due to the demagnetization phenomenon as shown in Fig. 4.1: when a ferromagnetic rod with a finite length is magnetized, the north and south poles are created at two opposite sides, leading to the demagnetizing field  $H_d$ . The demagnetizing field  $H_d$  depends on the magnetization  $M$  inside the core and the demagnetization factor  $D_M$  [17].

$$H_d = D_M \times M \quad (4.1)$$

$D_M$  is solely determined by the core shape and the effective permeability  $\mu_{eff}$  can be expressed:

$$\mu_{eff} = \frac{\mu_r}{1 + D_M(\mu_r - 1)} \quad (4.2)$$

where  $\mu_r$  is the relative permeability of the core material. Therefore, the core shape needs to be optimized to reduce the demagnetization factor and increase the effective permeability. The conventional method suggests that a thin and long rod could have a smaller demagnetization factor [17].

$$D_M \propto \frac{d}{l} \quad (4.3)$$

where  $d$  is the diameter of the rod and  $l$  is the length. By making the rod longer (in other words, making the path of the magnetic flux longer), the separation between the north pole



and the south pole increases, leading to a smaller demagnetizing field. Nevertheless, a very long and thin solenoid may not be the best solution as it occupies too much space because of its length. Besides, a long and thin ferromagnetic rod is brittle and prone to damage.

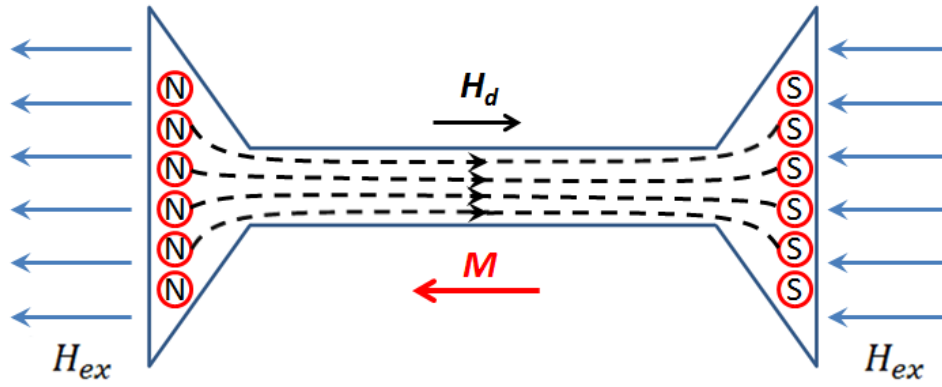


Fig. 4.2. The demagnetizing field inside a bow-tie-shaped core when applying an external magnetic field

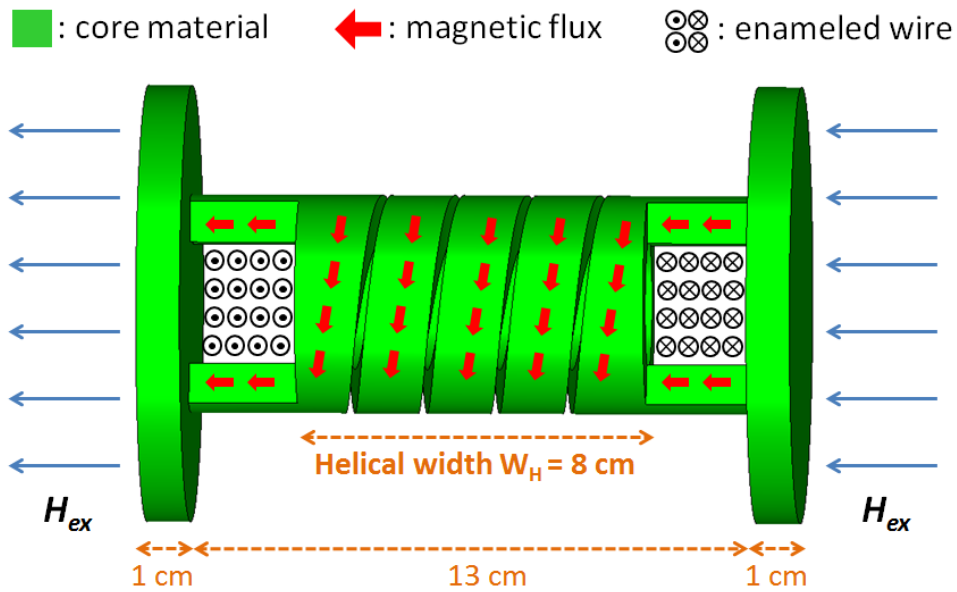


Fig. 4.3. The helical core proposed

In our preview work [1], a bow-tie shaped core has been proposed as shown in Fig. 4.2. By making its two ends broader, the magnetic flux can be concentrated in the center. Thus the effective permeability in middle part of the core can be increased. To further improve the performance, a novel helical core is proposed as shown in Fig. 4.3. Two big circular plates at both ends are used for the flux collection, which could guide more magnetic flux from the air into to the ferromagnetic core. In the middle, a helical shaped core is proposed to increase the

path of the magnetic flux while the physical length of the entirely core remains unchanged. Therefore, the separation between the north pole and south pole is lengthened dramatically which leads to a reduction in the demagnetizing field and an increase in the magnetic flux density.

To validate this new design, four different coils depicted in Fig. 4.4 are compared in the same uniform magnetic field generated by a Helmholtz coil. All of them have the following configurations for easy comparisons:

1. The same physical length of 15 cm;
2. An ideal magnetic core material with the relative permeability  $\mu_r$  and zero conductivity;
3. 100 turns of enameled wires wound on the core;
4. Placed in the same alternating magnetic field area ( $7 \mu T_{rms}$  at 50 Hz).

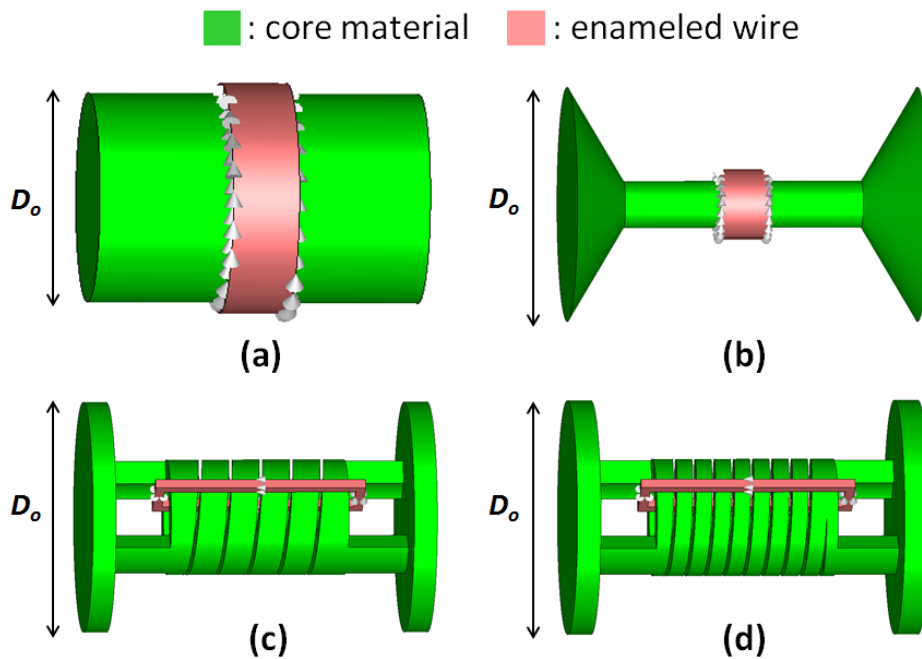


**Fig. 4.4.** (a) the conventional solenoid with diameter  $D_o = 10$  cm. (b) the bow-tie coil (c) the proposed coil with 5 turns of helical slots in the core. (d) the proposed coil with 10 turns of helical slots in the core

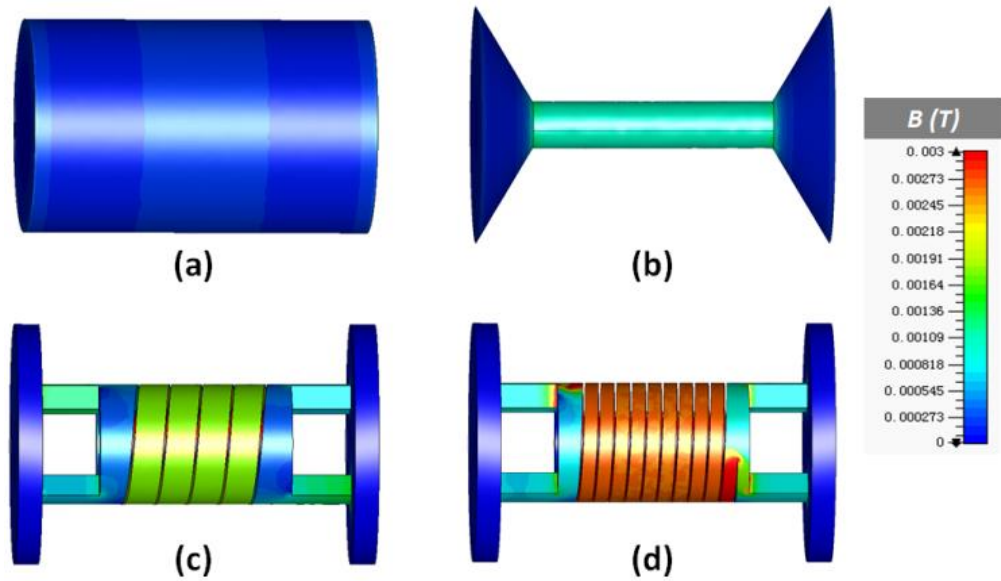


**Fig. 4.5.** The magnetic flux density  $B_{in}$  inside the four cores (refer to Fig. 4.7) when the external magnetic density of  $7 \mu T_{rms}$  is applied and the relative permeability is 10,000

Four cores are placed in a magnetic flux density of  $7 \mu T_{rms}$  which is normally achievable around high voltage equipment [1, 15]. The conductivity of the ferromagnetic material is set to zero intentionally to eliminate the eddy current losses, and the hysteresis effect is ignored. Therefore, we can focus on the magnetic properties with different core shapes. CST software is used as the simulation tool and the boundary condition is set to “open” to emulate the free space environment. Fig. 4.5 shows the simulated magnetic flux density  $B_{in}$  inside the four cores when the relative permeability  $\mu_r$  is assumed to be 10,000. Due to the demagnetization phenomenon, the magnetic flux density is always higher in the center of the core. As clearly depicted in Fig. 4.5, the flux density in the middle of the rod ( $0.16 \text{ mT}_{rms}$ ) and the bow-tie core ( $1.0 \text{ mT}_{rms}$ ) is relative small. For the proposed core (c) with 5 turns of helical slots, the flux density in the middle is around  $2.0 \text{ mT}_{rms}$  which doubles the value of the bow-tie core. When 10 turns of helical slots are introduced to the core as shown in Fig. 4.5(d), the flux density is enlarged to  $3.2 \text{ mT}_{rms}$ . This proves that by using the helical core to lengthen the path of the magnetic flux, the demagnetizing field is reduced and the magnetic flux density inside the core is greatly increased. If an enameled wire with a diameter of 0.14 mm is wound on the four cores for 100 turns, the voltages induced are plotted in Fig. 4.6 as a function of the relative permeability  $\mu_r$ . When  $\mu_r$  is 100,000, the voltage for the helical coil with 11 turns (d), bow-tie coil (b) and solenoid (a) are 69.6 mV, 7.94 mV and 8.98 mV

respectively, which indicates the magnetic flux inside the new helical core can be much larger than the conventional designs. In addition, the four curves become saturated as  $\mu_r$  increases. For solenoid (a) and bow-tie coil (b), their knee points appear when  $\mu_r$  approaches about 100. In contrast, for helical coil (c), its knee point is around 7000 and the knee point for helical coil (d) is even higher as the voltage still has the tendency to increase when  $\mu_r$  is larger than 100,000.

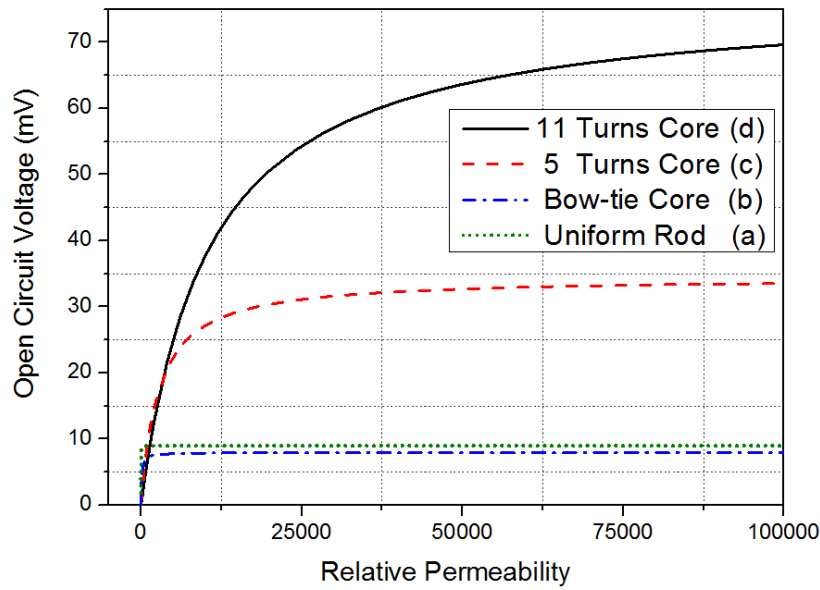


Fig. 4.6. The open circuit voltage of four coils when an external magnetic density of  $7 \mu\text{T}_{rms}$  is applied

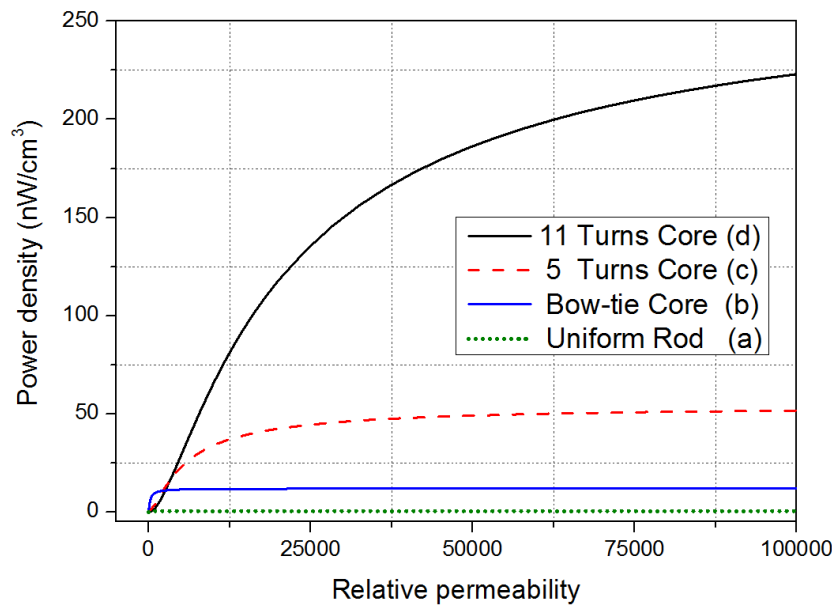


Fig. 4.7. The power density of four coils when an external magnetic flux density of  $7 \mu\text{T}_{rms}$  is applied

However, the power density from the coil depends not only on the induced voltage, but also on the coil resistance and the coil volume. If an ideal core material (no loss) is used, the coil resistance is solely determined by the wire resistance. For the 0.14 mm enameled wire, its resistance is 1.11  $\Omega/\text{m}$ . Using Equation (4.2), the coil resistance, the output power and the power densities of the four coils are calculated and concluded in Table 4.1. As depicted in Fig. 4.7, when  $\mu_r = 100,000$ , the power density of helical coil (d) is 223  $\text{nW}/\text{cm}^3$  which is 20 times more than that of Bow-tie coil (b). As a result, the proposed helical core has demonstrated a much better performance than previous designs due to the longer effective path of the magnetic flux.

**TABLE 4.1 The parameters of the four cores when  $\mu_r = 100,000$  and  $N = 100$**

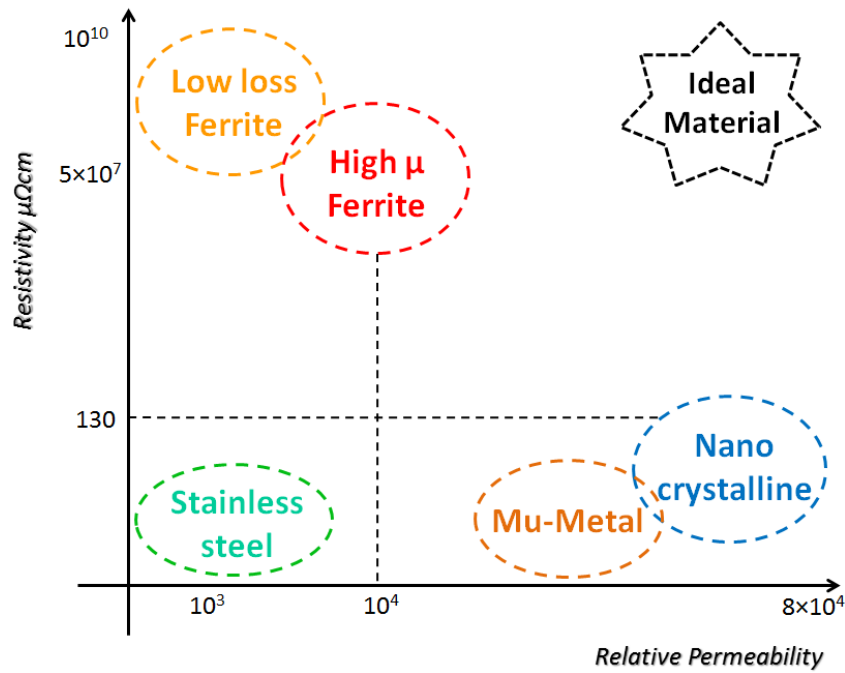
| Core Type   | Solenoid (a) | Bow-tie (b) | Helical (c) | Helical (d) |
|---|--------------|-------------|-------------|-------------|
| Open circuit voltage ( $\text{mV}_{\text{rms}}$ ) | 8.98         | 7.94        | 33.5        | 69.6        |
| Path of magnetic flux (cm)                        | 15.0         | 15.0        | 47.12       | 110.7       |
| Wire resistance ( $\Omega$ )                      | 34.87        | 6.97        | 20.0        | 20.0        |
| Output power ( $\mu\text{W}$ )                    | 0.58         | 2.26        | 14.1        | 60.6        |
| Core volume ( $\text{cm}^3$ )                     | 1178         | 189         | 273         | 273         |
| Power density ( $\text{nW}/\text{cm}^3$ )         | 0.49         | 11.9        | 51.7        | 223         |

## 4.2.2 Core Material Selection

As shown in Fig. 4.7, the power density of the helical coil increases with the increment of the relative permeability of the core material. However, it is also important to take the core losses into considerations. In general conditions, the core losses can be divided into hysteresis losses and eddy current losses. In this application, as the magnetic field is relative small and the frequency is only at 50 Hz, the hysteresis losses can be ignored compared to the eddy current losses. Thus, the core losses are mainly determined by eddy current losses. According to [17], the equation used to calculate the power consumption of the eddy current losses is:

$$w_{eddy} = \frac{S}{2k\rho} \left( \frac{dB_{core}}{dt} \right)^2 \quad (4.4)$$

where  $S$  is the cross section in  $m^2$ ;  $B_{core}$  is the magnetic flux density inside the core in T;  $\rho$  is the material resistivity in  $\Omega m$  and  $k$  is the shape factor. When a helical core is placed inside an alternating magnetic field with a fixed magnitude, the eddy current losses are inversely proportional to the resistivity  $\rho$ . As a consequence, the core material should have high relative permeability  $\mu_r$  as well as high resistivity  $\rho$ .



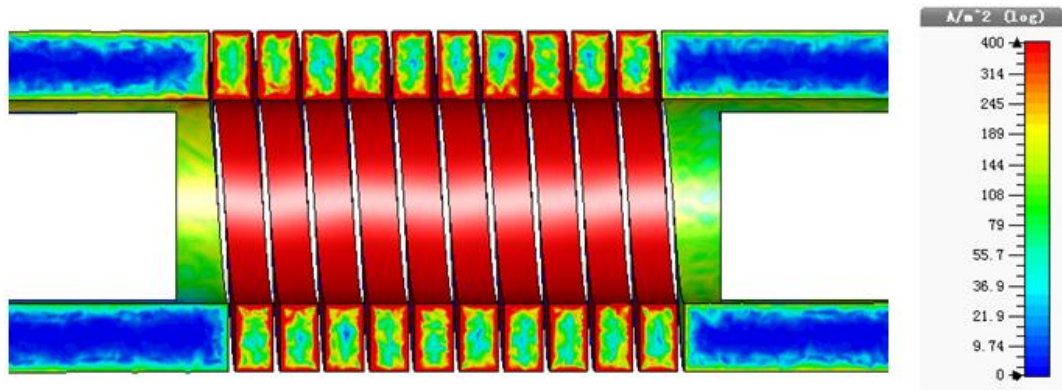
**Fig. 4.8. The relative permeability and resistivity of several typical ferromagnetic materials**

Fig. 4.8 shows the resistivity and relative permeability of some typical ferromagnetic materials. Metals and alloys can have very high relative permeability but low resistivity (usually in the magnitude of a few  $\mu\Omega m$  [18]). Nanocrystalline usually is considered as a popular ferromagnetic material due to its high relative permeability and high resistivity among the alloys [1, 17]. Ferrite is a semiconductor material whose resistivity is extremely high (usually in the unit of  $\Omega m$ ). However, its relative permeability is usually lower than 18,000. In this thesis, three different materials listed in Table II have been investigated to optimize the power output. The helical coil with 100 winding turns shown in Fig. 4.4(d) is selected as a testing example. CST is used to calculate the equivalent core resistance and the results are listed in Table II. The nanocrystalline core has the largest core resistance of 87.3  $\Omega$

because of the highest permeability and the lowest resistivity. Strong eddy currents are generated inside the core as shown in Fig. 4.9. Thus, its power output is greatly limited by the eddy current losses, or in other words, the equivalent core resistance. On the contrary, the core resistance of low loss ferrite is tiny ( $12.1 \mu\Omega$ ) but its power output is still small due to its low relative permeability. For the high  $\mu$  ferrite core, its core resistance is only  $3.97 \text{ m}\Omega$  which is negligible compared with to the wire resistance  $18.3 \Omega$ . Besides, as plotted in Fig. 4.9(d), the induced voltage becomes saturated when the relative permeability approaches to 15,000. The induced voltage of the nanocrystalline core ( $66.4 \text{ mV}$ ) is not significantly bigger than that of high  $\mu$  ferrite core ( $40.5 \text{ mV}$ ). As a result, the high  $\mu$  ferrite core has the largest power output, which indicates that it is the most suitable material for the proposed helical core.

**TABLE 4.2 The comparison of three different ferromagnetic materials**

| Material Type                         | Low loss Ferrite      | High $\mu$ Ferrite    | Nanocrystalline   |
|---------------------------------------|-----------------------|-----------------------|-------------------|
| Reference                             | [19]                  | [20]                  | [21]              |
| Typical core types                    | Cylindrical core      | Ring core, rod        | toroid, 'D' shape |
| Relative permeability                 | 800                   | 12,000                | 80,000            |
| Resistivity ( $\mu\Omega\text{m}$ )   | 108                   | $5 \times 10^5$       | 1.3               |
| Induced voltage ( $\text{mV}_{rms}$ ) | 5.15                  | 40.5                  | 66.4              |
| Core resistance ( $\Omega$ )          | $1.21 \times 10^{-5}$ | $3.97 \times 10^{-3}$ | 87.3              |
| Wire resistance ( $\Omega$ )          | 18.3                  | 18.3                  | 18.3              |
| Power output ( $\mu\text{W}$ )        | 0.36                  | 22.4                  | 10.4              |



**Fig. 4.9.** The eddy current density inside a nanocrystalline core



### 4.3 Optimization of the Helical Coil

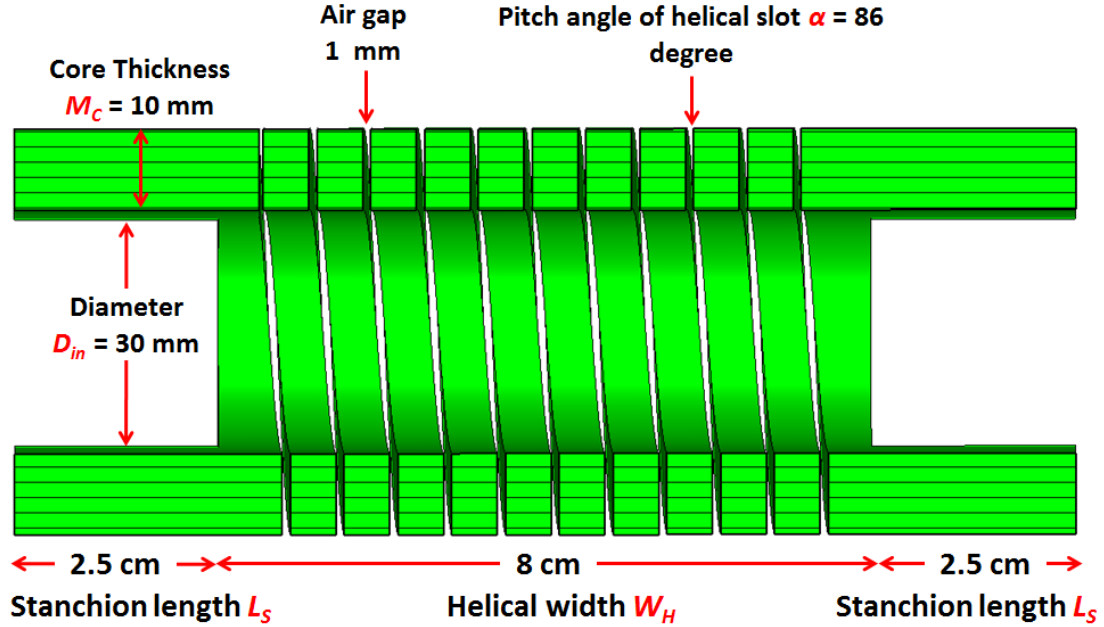


Fig. 4.10. The cross section view of a helical core

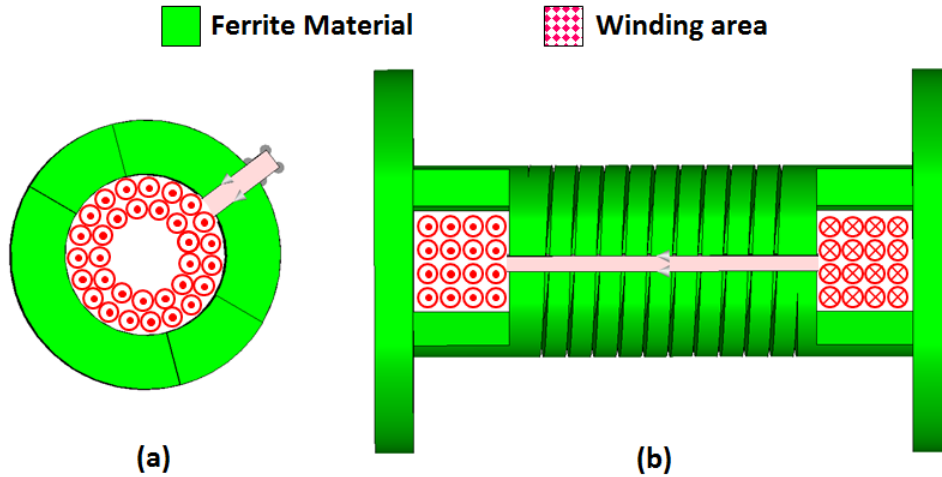


Fig. 4.11. The winding area of a helical core. (a) the cross section view, (b) the overall view from outside

As shown in Fig. 4.5 and Fig. 4.6, the helical coil with a longer path of the magnetic flux can generate higher voltage. The path of the flux can be made longer by increasing the pitch angle of the helical slot  $\alpha$  and the helical width  $W_H$  shown in Fig. 4.10. However, the power output from the harvesting coil also depends on the number of winding turns  $N$  and the wire resistance  $R_{wire}$ . As shown in Fig. 4.11, the winding area for a helical core is limited. If the

diameter  $D_{in}$  and stanchion length  $L_S$  are small, there are less winding areas which reduce the power output. Therefore, the shape of the helical core should be optimized to maximize the output power density. The core shown in Fig. 4.10 is used as a reference and the following three testing conditions are set for the optimizations.

1. The size of two big circular plates as shown in Fig. 4.3(a) is kept unchanged and the physical length of the entire core is 15 cm long.
2. The high  $\mu$  ferrite material with  $\mu_r = 12,000$  and  $\rho = 0.5 \text{ } \Omega\text{m}$  is used and the external magnetic flux density is  $7 \text{ } \mu\text{T}_{rms}$ .
3. An enameled wire with a diameter  $d$  of 0.14 mm and the wire resistance  $\rho_{wire}$  of  $1.11 \text{ } \Omega/\text{m}$  is used to wrap on the helical core with the winding area provided.

As the ferrite material is used, the eddy current can be greatly reduced and the overall coil resistance is determined by the wire resistance. To calculate the wire resistance when the core is fully wound, two situations should be considered.

1. When  $L_S > 0.5D_{in}$ , the wire is fully occupied in the winding area shown in Fig. 4.14(a). The total layer of the enameled wire  $K_{total}$  is:

$$K_{total} = \frac{0.5D_{in}}{d} \quad (4.5)$$

2. When  $L_S < 0.5D_{in}$ , the wire is fully occupied in the winding area shown in Fig. 4.14(b). The total layer  $K_{total}$  is:

$$K_{total} = \frac{L_S}{d} \quad (4.6)$$

Therefore, the total number of turns  $N$  can be obtained:

$$N = \sum_{k=1}^{K_{total}} \left( \frac{\pi}{\arcsin\left(\frac{d}{D_{in} - (2k-1)d}\right)} \right) \quad (4.7)$$

The total resistance of the wire can be calculated:

$$R_{wire} = \rho_{wire} \sum_{k=1}^{K_{total}} L_k = \rho_{wire} \sum_{k=1}^{K_{total}} \left( \frac{\pi(2W_H + 2M_c + 8kd)}{\arcsin\left(\frac{d}{D_{in} - (2k-1)d}\right)} \right) \quad (4.8)$$

where  $\rho_{wire}$  is the wire resistance in  $\Omega/\text{m}$  and  $M_c$  is the thickness of the core in meter. More detailed derivations and explanations of Equations (4.5) to (4.8) can be found in Appendix.

### 4.3.1 The Pitch Angle $\alpha$

When the pitch angle of the helical slot becomes bigger and other parameters are unchanged, the path of the magnetic flux increases and the winding area is not affected. It is expected that the power density increases with the increment of the pitch angle as shown in Fig. 4.12. However, when the pitch angle is too big, the helical core will be very difficult to manufacture and prone to damage especially for the ferrite material.

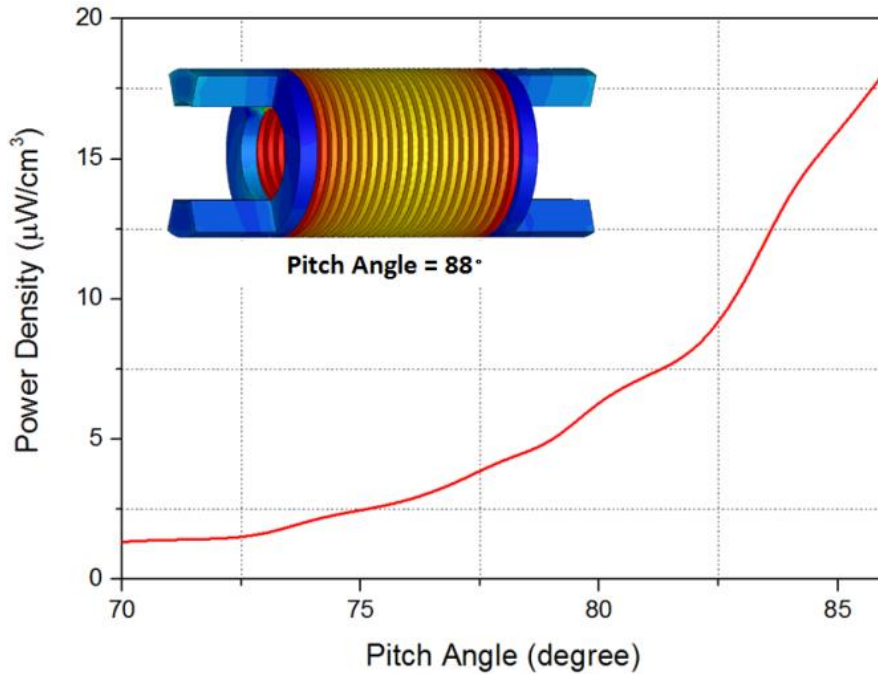


Fig. 4.12. The output power density as a function of the pitch angle

### 4.3.2 Helical Width $W_H$ and Inner Diameter $D_{in}$

When the pitched angle is fixed, the path of the flux can be made longer by increasing the helical width  $W_H$ . However, the stanchion length  $L_S$  will decrease as the physical length of the core is limited to 15 cm. This will reduce the winding area shown in Fig. 4.11(b). As shown in Fig. 4.13, the magnetic flux generated inside the core increases with the helical width. For the number of turns  $N$ , it is constant when the helical width is small as the layer  $K_{total}$  of the enameled wire is determined by the inner diameter  $D_{in}$ . When the helical width continues to increase, the stanchion length  $L_S$  will be smaller than the inner radius  $D_{in}/2$ . In this situation, the layer  $K_{total}$  of the wire is proportional to the stanchion length. Thus, the number of turns drops down as the stanchion length decreases. The output power density of the coil is plotted in Fig. 4.14 as a function of the helical width. The peak value appears when the stanchion length  $L_S$  is equal to the inner radius  $D_{in}/2$ . In this case, both winding areas shown in Fig. 4.11(a) and (b) are fully utilized.

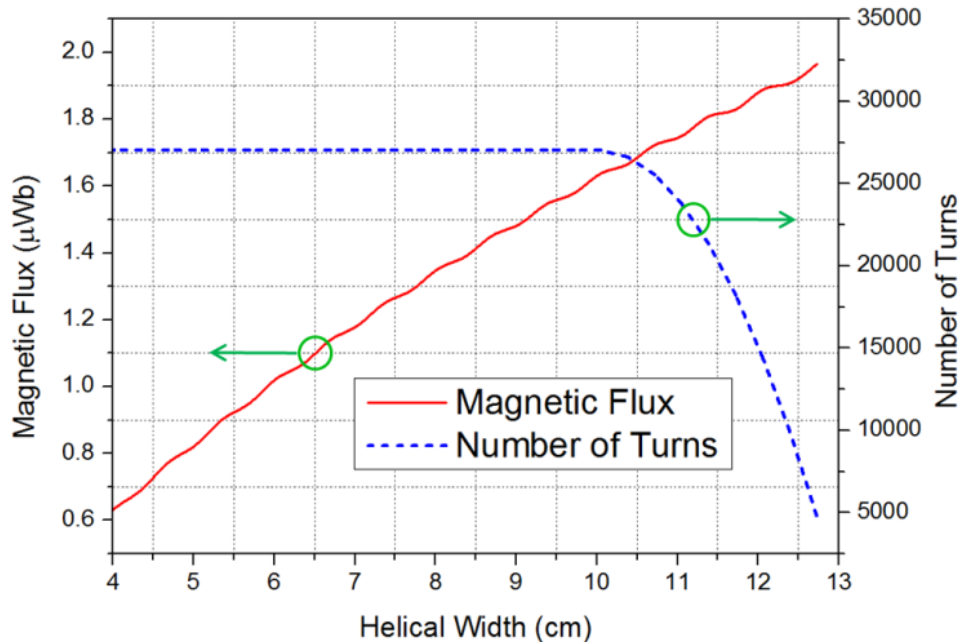


Fig. 4.13. The magnetic flux and the number of turns as a function of the helical width  $W_H$ .

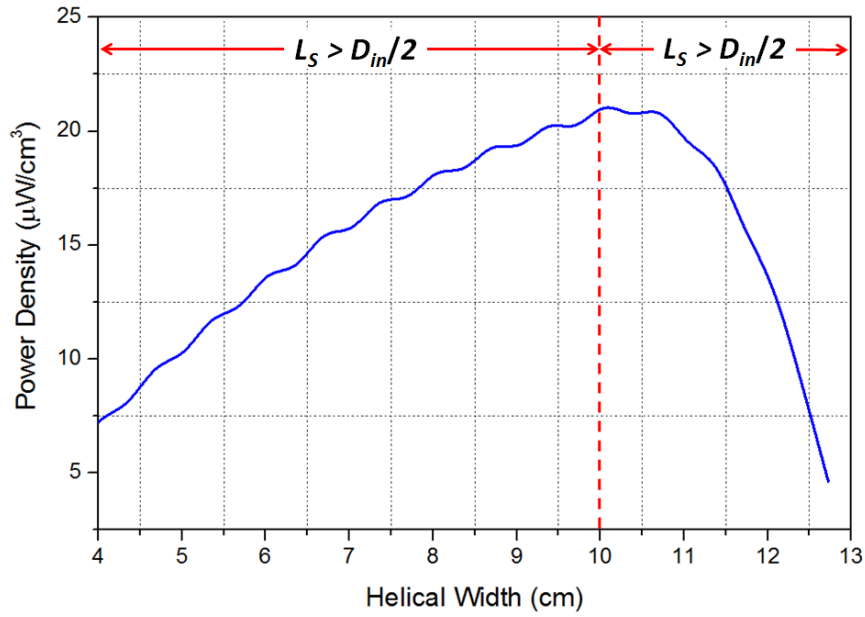


Fig. 4.14. The power density as a function of the helical width  $W_H$ .

### 4.3.3 Core Thickness $M_C$

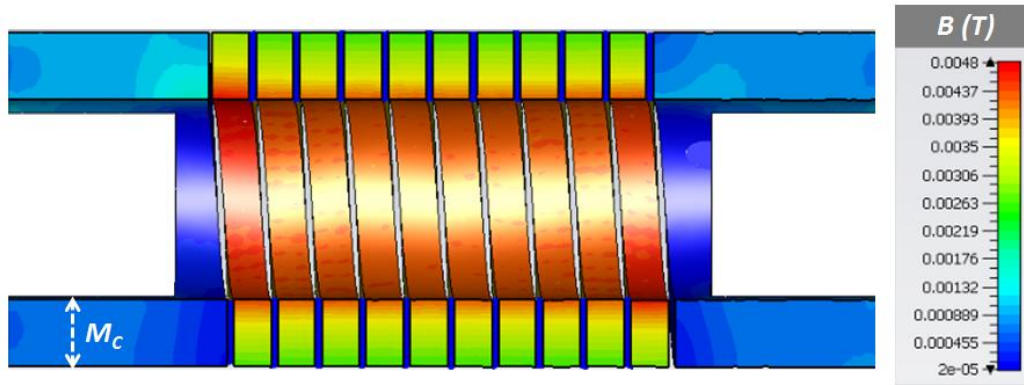


Fig. 4.15. The magnetic flux density inside a helical core when  $M_c = 1$  cm

By increasing the thickness  $M_C$  of the core, more magnetic flux can pass through the core which leads to a higher induced voltage. However, due to the special shape of the helical core, the magnetic flux density inside the core is not uniformly distributed. By applying the magnetic circuit theory [17], the majority of the magnetic flux tends to travel along the shortest path where the magnetic reluctance is small. As shown in Fig. 4.15, the magnetic flux density is larger when it is near to the inner edge of the helical core. Therefore, by

making the core thicker, the total magnetic flux does not always increase correspondingly. Nevertheless, the wire resistance and core volume are always directly related to the core thickness. As depicted in Fig. 4.16, when the core thickness is relative small, the magnetic flux and power density increase with the core thickness  $M_C$ . While the thickness is further increased, the magnetic flux becomes saturated and the power density begins to decrease. For the curve of the magnetic flux in Fig. 4.16, its knee point appears around 0.8 cm where the helical coil produces the maximum power density.

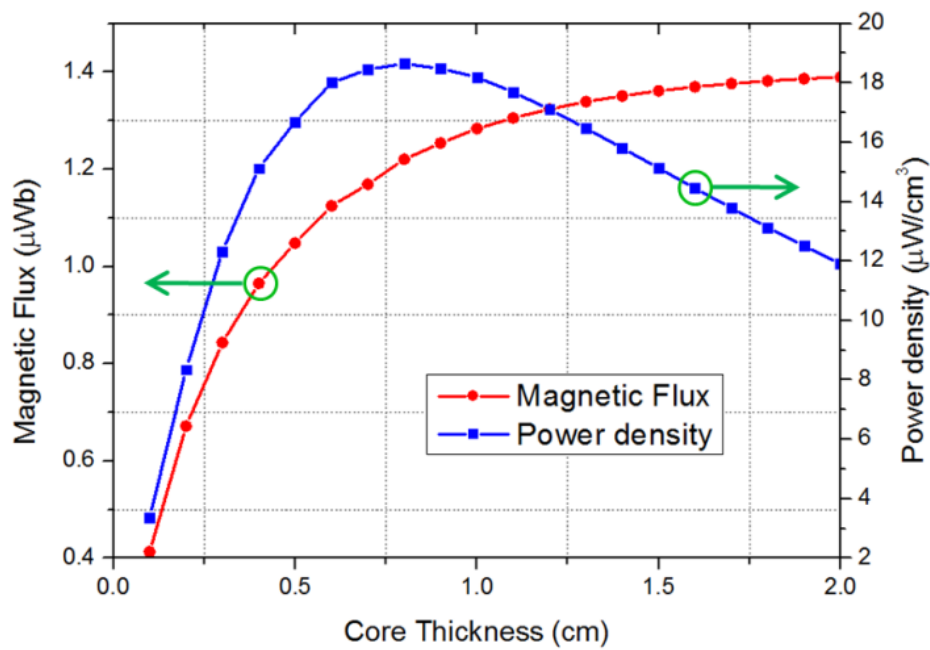
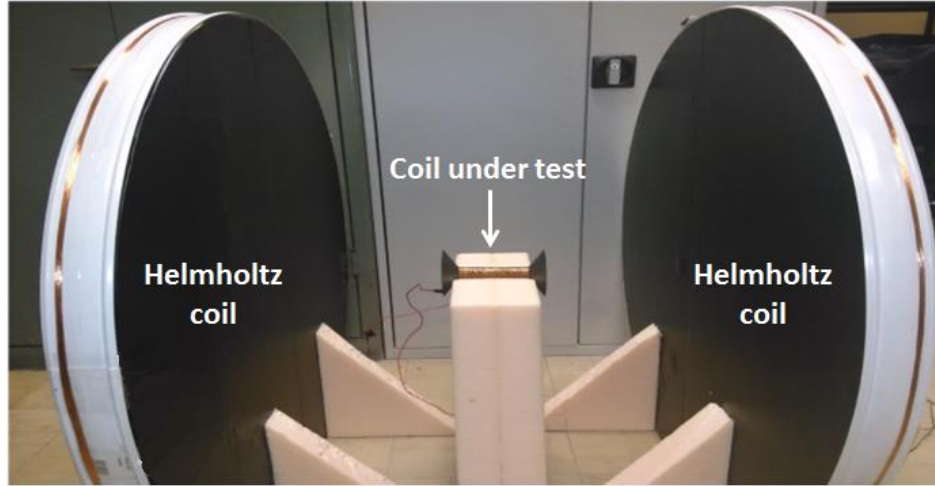


Fig. 4.16. The magnetic flux and power output as a function of the core thickness

In conclusion, to increase the power output from the helical coil, the path of the magnetic flux should be made longer and the winding area needs to be fully utilized. The pitch angle of the helical slot should be increased as big as possible which could significantly boost the power output. When the stanchion length is equal to the inner radius  $D_{in}/2$ , the winding area inside the helical core can be efficiently used and lead to a high power output. Finally, the core thickness needs to be carefully optimized to achieve higher magnetic flux without making the core too big.

## 4.4 Experimental Validations and Discussions



**Fig. 4.17. A Helmholtz coil used to generate a uniform magnetic field in the laboratory**

A Helmholtz coil as shown in Fig. 4.17 (consisting of two identical coil rings) is made to generate a uniform magnetic field to imitate the magnetic field environment near high voltage equipment. The magnetic flux density can be calculated [22]:

$$B = (0.8)^{3/2} \frac{\mu_0 N I}{R_H} \quad (4.9)$$

where  $\mu_0$  is the permeability of free space,  $N$  is the number of turns wound on the Helmholtz coil;  $I$  is the current passing through the coil;  $R_H$  is the radius of the Helmholtz coil. In this experiment, the radius of each coil ring is 0.5 meter with 33 turns of conducting wire on it and the two coil rings are separated by half a meter. With a 120 mA<sub>rms</sub> current passing through the Helmholtz coil, a magnetic flux density of 7  $\mu$ T<sub>rms</sub> is generated. Due to the complex shape of the helical core and the physical properties of the ferrite material, it is very difficult and expensive to manufacture the whole core in one ferrite piece. Instead, five pieces shown in Fig. 4.18 are fabricated separately and then glued together. For each helical piece, a ferrite tube with a suitable size is fabricated and the helical slot is cut carefully by a special grinding tool. The helical core manufactured is shown in Fig. 4.19. The stanchion length is 1.5 cm and equal to inner radius of the core so that the winding area inside the core can be fully utilized. The pitch angle of the helical slot is 86 degrees. The core would be very fragile and prone to damage if the angle is any higher. High permeability Mn-Zn ferrite [23] is used

as the core material with relative permeability  $12000 \pm 30\%$  and the resistivity of  $0.15 \Omega\text{m}$ .

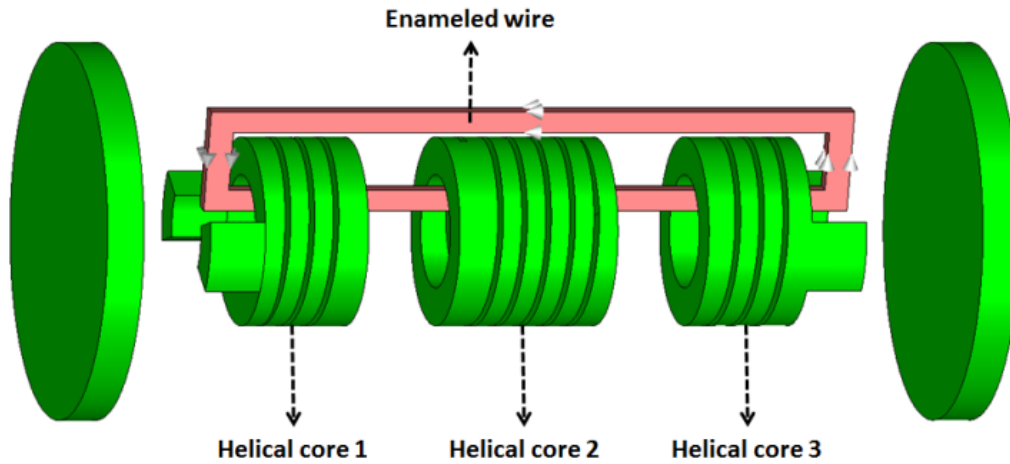


Fig. 4.18. The manufacturing process of a helical core with five ferrite pieces

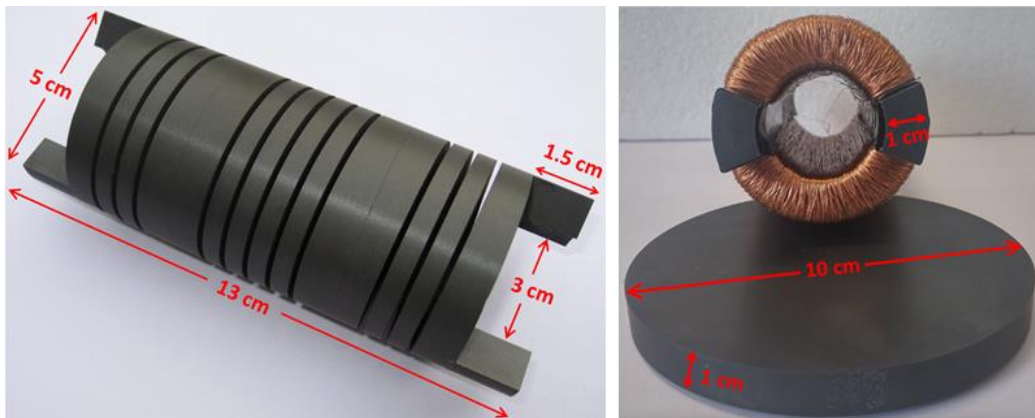


Fig. 4.19. (a) the overview of the helical core. (b) the circular plate and the helical core with the enameled wire

An enameled wire with a diameter of 0.4 mm and the wire resistance of  $0.136 \Omega/\text{m}$  is used to wind on the helical core. As the core is too long, it is very difficult to find a proper winding machine to wrap the wire on the helical core automatically. Therefore, only 200 and 400 turns of the wire is wound manually just to prove the proposed concept. The coil is put inside the Helmholtz coil and the open circuit voltage is measured using a multimeter. The measured voltage is listed in Table III and compared to the simulated values. The measured results are slightly lower than the simulated ones which are mainly caused by the fabrication errors of the ferrite core. Firstly, the relative permeability of the ferrite is in the range of 8400 to 15600 according to the datasheet [22], which may bring some uncertainty into the experiment.



Secondly, as the whole helical core is made of five separated ferrite pieces, gaps may exist in each contact surface which reduces the overall effective permeability.

**TABLE 4.3 The measured and simulated results of coil voltage**

| The number of turns | Simulated results (rms) | Measured results (rms) |
|---------------------|-------------------------|------------------------|
| $N = 200$           | 101.6 mV                | 91.5 mV                |
| $N = 400$           | 203.1 mV                | 184.7 mV               |

**TABLE 4.4 The measured and calculated results of the coil resistance**

| Number of turns | R-wire (theory) | R-wire (measured) | R-coil (measured) |
|-----------------|-----------------|-------------------|-------------------|
| $N = 200$       | 6.11 $\Omega$   | 6.85 $\Omega$     | 6.88 $\Omega$     |
| $N = 400$       | 12.54 $\Omega$  | 13.88 $\Omega$    | 13.96 $\Omega$    |

The effective coil resistance can be measured by a 50 Hz bridge. The power output at the load can be maximized by tuning the compensating capacitor and the load resistance. According to the maximum power transfer theory, the coil resistance should be the same as the load resistance. The wire resistance is measured with a multi-meter and results are listed in Table 4.4. The measured wire resistance is about 10% higher than the theoretical value as the enameled wire is manually wrapped and cannot be perfectly aligned. This causes a longer wire to achieve the same number of turns and results in the difference between the measured and theoretical values. The overall coil resistance measured at 50 Hz is very close to the wire resistance, proving that the eddy current losses are minimized by using ferrite material.

**TABLE 4.5 The measured and calculated results of power output**

| The number of turns | Simulated results | Measured results    |
|---------------------|-------------------|---------------------|
| $N = 200$           | 0.42 mW           | 0.31 mW             |
| $N = 400$           | 0.83 mW           | 0.61 mW             |
| $N = 2000$          | 3.96 mW           | 2.86 mW (predicted) |

The helical coil with 400 turns can deliver a power output of 0.61 mW under the magnetic flux density of  $7 \mu\text{T}_{\text{rms}}$ . When more winding can be added on the core, the more power output from the coil can be achieved [1]. From Equation (9) and in the ideal case, the fabricated core shown in Fig. 4.19 can wrap a maximum of 3310 turns of enameled wire (diameter  $d = 0.4$  mm). However, due to the imperfect winding (e.g. wire misalignments), we conservatively estimate that only 2000 turns of wire can be wound on the core. In this case, it can be predicted that the coil voltage will increase to 910 mV as the induced voltage is linearly proportional to the number of turns. According to Equations (9) and (10), when  $N = 2000$ , the wire resistance is  $66 \Omega$ . As a consequence, the predicted power output from the core is 2.86 mW when  $N = 2000$ .

**TABLE 4.6 The comparison of different designs**

| The coil type        | Bow-tie coil [1]               | Solenoid [15]                   | Helical coil $N = 400$         |
|----------------------|--------------------------------|---------------------------------|--------------------------------|
| Physical length      | 15 cm                          | 50 cm                           | 15 cm                          |
| Applied flux density | $7 \mu\text{T}_{\text{rms}}$   | $18.5 \mu\text{T}_{\text{rms}}$ | $7 \mu\text{T}_{\text{rms}}$   |
| The number of turns  | 40,000                         | 40,000                          | 400                            |
| The wire diameter    | 0.14 mm                        | Unknown                         | 0.4 mm                         |
| Induced voltage      | $2.95 \text{ V}_{\text{rms}}$  | $10.5 \text{ V}_{\text{rms}}$   | $185 \text{ mV}_{\text{rms}}$  |
| Coil resistance      | $6.03 \text{ k}\Omega$         | $33 \text{ k}\Omega$            | $13.96 \Omega$                 |
| Volume               | $188 \text{ cm}^3$             | $981 \text{ cm}^3$              | $292 \text{ cm}^3$             |
| Power output         | $360 \mu\text{W}$              | $833 \mu\text{W}$               | $612 \mu\text{W}$              |
| Power density        | $1.86 \mu\text{W}/\text{cm}^3$ | $0.85 \mu\text{W}/\text{cm}^3$  | $2.10 \mu\text{W}/\text{cm}^3$ |

The measured power density for the helical coil with 400 turns is  $2.1 \mu\text{W}/\text{cm}^3$  at  $7 \mu\text{T}_{\text{rms}}$ . If the number of turns can be increased to 2000, the predicted power output will be  $7.9 \mu\text{W}/\text{cm}^3$ . Both values are lower than the simulated results ( $21 \mu\text{W}/\text{cm}^3$  at  $7 \mu\text{T}_{\text{rms}}$ ) shown in Fig. 4.17. This is mainly limited by the ferrite core fabrication and low number of winding turns. If a specific injection mold can be invested, a helical core can be manufactured in one ferrite piece and more helical slots can be cut compared to the fabricated core in Fig. 19(a). Therefore, the measured output power can be inflated. Furthermore, by using a mold, the

fabrication process can be simplified and the unit price of a helical core can be reduced dramatically. If a proper coil winding machine can be found and utilized, more wires can be efficiently wound on the core which also leads to a higher power output. Despite of these limitations, the measured power density is still better than previous reported designs demonstrated in Table 4.6. If more wires can be wound on this helical core, the power density will increase as shown in Fig. 4.20. When  $N = 2000$ , its predicted power density ( $9.8 \mu\text{W}/\text{cm}^3$ ) is 4 times larger than that of the bow-tie coil [1] which was achieved with 40,000 turns of wires.

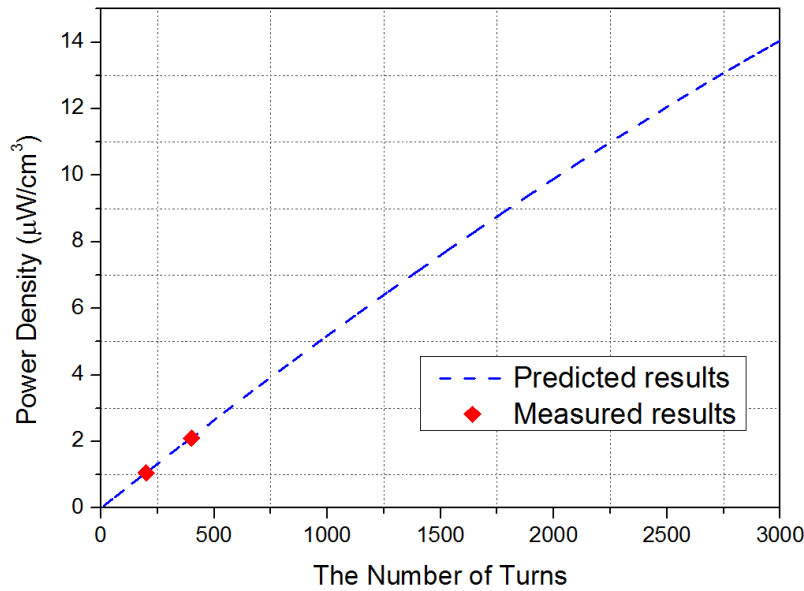


**Fig. 4.20. The predicted power output as a function of the number of turns**

From the experiment,  $612 \mu\text{W}$  was collected at the load by using the helical coil with 400 turns, which might be enough to power a small wireless sensor [24]. The power harvested can be further increased to  $2.86 \text{ mW}$  if the coil can have 2000 turns of wires. However, the power consumption of a GPRS data logger is  $3.6 \text{ W}$  [25]. If the data is collected in every 30 minutes and the data logger takes a maximum of 1 minute to transmit the information to the server, the average power consumption would be  $120 \text{ mW}$ . As a result, a larger helical core shown in Fig. 4.21 is designed to collect more power. The physical length of the core is increased to  $25 \text{ cm}$  so that the path of the magnetic flux can be further lengthened. Meanwhile, the outer diameter  $D_o$  of the big circular plate is enlarged to guide more flux passing through the helical core. According to some previous research listed in Table VII, the magnetic flux

densities under overhead lines or inside electric substations are usually larger than  $11 \mu\text{T}_{rms}$ . If we can wind 8,000 turns of enameled wires with the diameter of 0.4 mm and place this coil in a magnetic flux density of  $11 \mu\text{T}_{rms}$ , 160.5 mW can be harvested. This means that the large helical coil shown in Fig. 4.21 is able to power a GPRS data logger when it is near high voltage equipment.

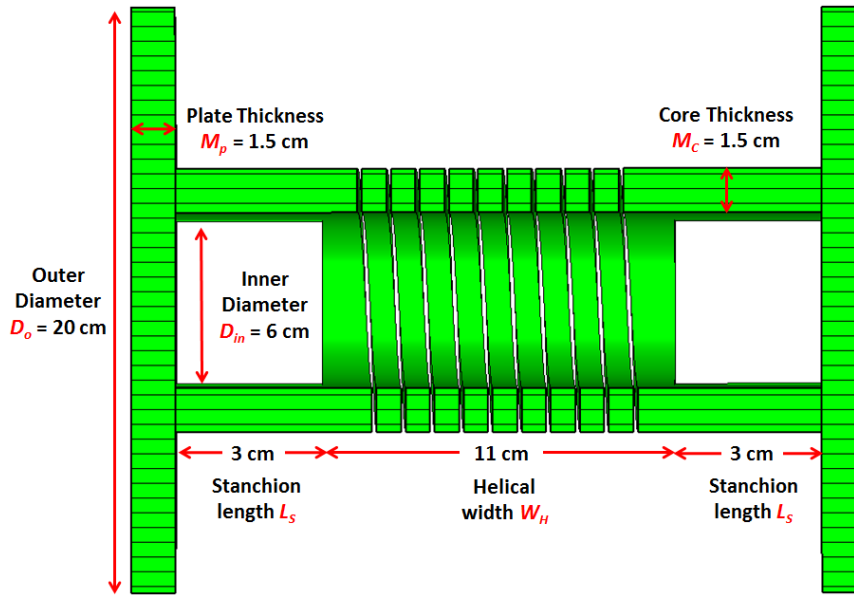


Fig. 4.21. The cross section view of a larger and longer helical core

TABLE 4.7 The survey of magnetic field near high power equipment

| Test environment          | Test conditions  | Magnetic flux density            |
|---------------------------|--|----------------------------------|
| 132 kV L7 overhead lines  | 5 meters above the ground<br>$I_{rms} = 700 \text{ A}$ | $11.0 \mu\text{T}_{rms}$ [26]    |
| 400 kV L12 overhead lines | 3 meters above the ground<br>$I_{rms} = 700 \text{ A}$ | $11.3 \mu\text{T}_{rms}$ [26]    |
| 11 kV indoor substation   | Near high voltage transformers and switchgears         | $15 - 20 \mu\text{T}_{rms}$ [27] |
| 150 kV outdoor substation | Near high voltage transformers                         | $26 - 28 \mu\text{T}_{rms}$ [28] |
| 345 kV outdoor substation | Close to high voltage circuit breakers                 | $30 - 40 \mu\text{T}_{rms}$ [29] |

## 4.6 Summary

In this chapter, a completely new design of a special coil has been proposed to scavenge the magnetic field energy near high power equipment such as overhead lines, transformers, switchgears, etc. The coil does not need to be clamped to the power cable and can be installed almost anywhere in a substation or under overhead lines. It is highly efficient thus a range of sensors can be powered which is not always possible for the cable-clamped energy harvester.

A novel helical core has been proposed and optimized to produce a much higher power density compared to the conventional designs. This was based on the theoretical analysis and subsequently verified by the experiment measurements. The special helical shape design has dramatically lengthened the path of the magnetic flux, which reduced the demagnetization and led to a higher power output. The core material was selected by compromising high permeability and low eddy current losses. High permeability ferrite was identified as the most suitable core material, given its high relative permeability and ultra-low conductivity. The geometry shape of the helical core has been optimized to increase the path of the magnetic flux and better utilize the winding area available inside the core. From the experimental results, the power density of a helical coil with only 400 turns was already greater than a recently reported result if both coils were placed into the same magnetic field. If the fabricated coil can have 2000 turns of wire, the predicted power density ( $9.8 \mu\text{W}/\text{cm}^3$ ) is 4 times larger than the previous designs with the same or larger size. Thus the proposed solution is extremely efficient on harvesting the magnetic field energy near high voltage equipment and can be used to power a range of wireless sensors.

## 4.7 References

- [1] S. Yuan, Y. Huang, J. Zhou, Q. Xu and C. Song, “Magnetic Field Energy Harvesting Under Overhead Power Lines”, *IEEE Transaction on Power Electronics*, vol. 30, issue 11, pp. 6191 – 6202, 2015
- [2] J. Moon, S.B. Leeb, “Analysis Model for Magnetic Energy Harvesters”, *IEEE Transactions of Power Electronics*, vol.30, issue: 8, pp. 4302-4311, 2015
- [3] J. Moon, S.B. Leeb, “Power Electronic Circuits for Magnetic Energy Harvesters”, *IEEE Transactions on Power Electronics*, Vol.31, Issue: 1, pp. 270-279, 2016
- [4] T. Hosseinimehr and A. Tabesh, "Magnetic Field Energy Harvesting from AC Lines for Powering Wireless Sensor Nodes in Smart Grids", *IEEE Transactions on Industrial Electronics*, pp. 1-1, 2016.
- [5] J. Moon and S. Leeb, "Power loss analysis with high primary current in magnetic energy harvesters", *2015 IEEE 16th Workshop on Control and Modeling for Power Electronics (COMPEL)*, 2015.
- [6] M. J. Moser, T. Bretterkieber, H. Zangl and G. Brasseur, “Strong and Weak Electric Field Interfering: Capacitive Icing Detection and Capacitive Energy Harvesting on a 220-kV High-Voltage Overhead Power Line”, *IEEE Transaction on Industrial Electronics*, vol. 58, no. 7, pp. 2597-2604, 2011
- [7] D. J. Spoor and J. P. Roberts, “Development and Experimental Validation of a Weather-Based Dynamic Line Rating System”, *Innovative Smart Grid Technologies Aisa (ISGT)*, pp. 1-7, 2011
- [8] Y. Biçen; F. Aras and Y. Kirkrici, “Lifetime Estimation and Monitoring of Power Transformer Considering Annual Load Factors”, *IEEE Transaction on Dielectrics and Electrical Insulation*, vol. 21, issue. 3, pp. 1360-1367, 2014
- [9] D. M. Green, J. P. Gentle and K. S. Myers, “A Comparison of Real-Time Thermal Rating Systems in the U.S. and the U.K.”, *IEEE Transactions on Power Delivery*, vol. 29, issue: 4, pp. 1849-1858, 2014

- [10] A. K. Kazerooni, J. Mutale, M. Perry, S. Venkatesan and D. Morrice, "Dynamic thermal rating application to facilitate wind energy integration", *IEEE Trondheim PowerTech*, pp. 1-7, 2011
- [11] A. Safdarian, M. Degefa, M. Fotuhi-Firuzabad and M. Lehtonen, "Benefits of Real-Time Monitoring to Distribution Systems: Dynamic Thermal Rating", *IEEE Transaction on Smart Grid*, vol. 6, no. 4, pp. 2023-2031, 2015.
- [12] C. Li, G. Ma and B. Qi, "Condition Monitoring and Diagnosis of High-Voltage Equipment in China –Recent Progress", *IEEE Electrical Insulation Magazine*, vol. 29, issue: 5, pp. 71-78, 2013
- [13] Z. Wang, M. Begovi, and J. Wang, "Analysis of Conservation Voltage Reduction Effects Based on Multistage SVR and Stochastic Process", *IEEE Transactions on Smart Grid*, vol. 5, no. 1, pp. 431-439, 2014
- [14] Z. Wang and J. Wang, "Review on Implementation and Assessment of Conservation Voltage Reduction", *IEEE Transaction on Power System.*, vol. 29, no. 3, pp. 1306-1315, 2014.
- [15] N. M. Roscoe and M. D. Judd, "Harvesting Energy from Magnetic Fields to Power Condition Monitoring Sensors", *IEEE Sensors Journal*, vol. 13, issue: 6, pp. 2263-2270, 2013
- [16] K. Tashiro, H. Wakiwaka, S. Inoue, and Y. Uchiyama, "Energy Harvesting of Magnetic Power-Line Noise", *IEEE Transactions on Magnetics*, vol. 47, issue: 10, pp. 4441-4444, 2011
- [17] D. Jiles, "Introduction to Magnetism and Magnetics Materials", in *Magnetism*, 2<sup>nd</sup> ed. Ames, Iowa: Chapman & Hall, pp. 49-51, 1998
- [18] C. Heck, "Magnetic Materials and their Applications", London Butterworths, pp. 212-213, 1974
- [19] Ferroxcube, 3R1 Material Specification, datasheet available at <http://www.ferroxcube.com/FerroxcubeCorporateReception/datasheet/3r1.pdf>, 2008

- [20] Ferroxcube, 3E12 Material Specification, datasheet available at <http://www.ferroxcube.com/FerroxcubeCorporateReception/datasheet/3e12.pdf>, 2013
- [21] Wiltan, Nanocrystalline Toroidal Cores, datasheet available at [http://media.wix.com/ugd/aba60c\\_dae514a99bb04303b0630f221483c0dc.pdf](http://media.wix.com/ugd/aba60c_dae514a99bb04303b0630f221483c0dc.pdf), 2013
- [22] E. Javor and T. Anderson, "Design of a Helmholtz coil for low frequency magnetic field susceptibility testing", *1998 IEEE EMC Symposium. International Symposium on Electromagnetic Compatibility. Symposium Record (Cat. No.98CH36253)*.
- [23] Mn-Zn ferrite, R12k Material Characteristics, datasheet available at [www.chinadmegc.com/material\\_download.php?22](http://www.chinadmegc.com/material_download.php?22), 2014
- [24] Memsic, Wireless Measurement System (MPR2400VB), [http://www.memsic.com/userfiles/files/Datasheets/WSN/6020-0060-04-B\\_MICAz.pdf](http://www.memsic.com/userfiles/files/Datasheets/WSN/6020-0060-04-B_MICAz.pdf), 2013
- [25] Invisible-systems, Technical Datasheet: Gateway GPRS, GPS & RF, <http://www.invisible-systems.com/solutions/pdf/Gateway%20GPRS%20GPS%20RF.pdf>, 2015
- [26] National Grid, "On-line calculator | EMFs.info", *EMFs.info*, <http://www.emfs.info/sources/overhead/ohl-calculating/calculator/>, 2016
- [27] I. Said, H. Hussain and V. Dave, "Characterization of magnetic field at distribution substations", *2010 9th International Conference on Environment and Electrical Engineering*, 2010.
- [28] K. Choma and M. Etezadi-Amoli, "Magnetic field measurements in a 345 kV substation", *2011 North American Power Symposium*, 2011.
- [29] A. Safigianni and C. Tsompanidou, "Electric- and Magnetic-Field Measurements in an Outdoor Electric Power Substation", *IEEE Transactions on Power Delivery*, vol. 24, no. 1, pp. 38-42, 2009.



## Chapter 5. Matching Circuit and Energy Management Unit

### 5.1 Introduction

The energy harvesting technique is the enabling technology for the application of wireless sensors to many industrial applications where the hard-wired power is not available, and the battery cannot be frequently replaced due to the inaccessibility, the large amount of batteries and the risk to personal safety [1]. The real-time data collected by self-powered wireless sensors are the foundation of many smart grid applications. There are several ambient energy sources near high voltage equipment including solar [2-3], wind [4-5], electric field [6-11] and magnetic field [12-19]. As discussed in Section 1.2, a free-standing magnetic field energy harvester is a good energy source to power wireless sensors due to a combination of the reliability, flexibility, quick deployment and low price. In Chapters 3 and 4, two highly efficient coils have been developed to collect the magnetic field energy at a matched load (a compensating capacitor and a resistor). However, to utilize the harvested energy to power a wireless sensor, a more complicated circuit system is required and the structure is demonstrated in Fig. 5.1 and Fig. 5.2.

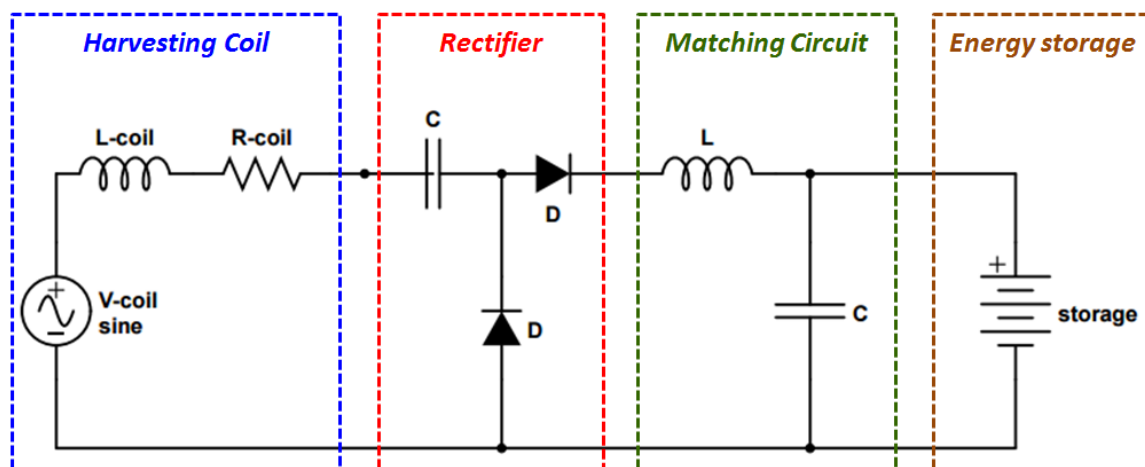
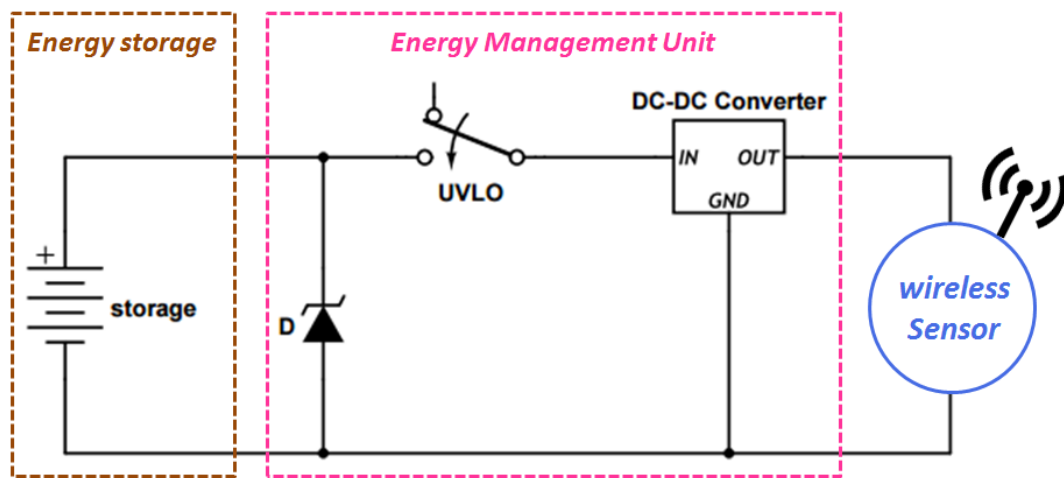


Fig. 5.1. The circuit system of using a harvesting coil to charge an energy storage device

First of all, a rectifier is needed to convert the AC signal from the harvesting coil into a DC value. As the output voltage from a free-standing coil is relatively small, a Cockcroft-Walton voltage multiplier can be applied to boost the output voltage and also provide full-wave rectification [1, 12].

Secondly, a good matching circuit has to be developed by taking the nonlinear components in to consideration (e.g. diodes, transistors, rechargeable batteries, charging capacitors, etc.). Nina *et al* built an analytic model to calculate the optimum value of a resistive load connected to a voltage doubler [1]. Nevertheless, in practice, the power harvested from the magnetic field energy is not large enough to directly power a wireless sensor. A small energy storage unit (ESU) (a rechargeable battery or a capacitor) should be applied as a buffer stage to store the harvested energy for a certain period before powering a wireless sensor. Hence, a special matching network should be designed to match the impedance of the ESU to the harvesting coil so that the charging speed can be accelerated.



**Fig. 5.2.** An energy storage device connected with an energy management unit and a wireless sensor

Finally, an energy management unit (also known as battery management unit) is needed as a start-up circuit for the wireless sensor. It monitors the status of the energy storage unit. When the energy accumulated in the ESU is higher than a threshold, the wireless sensor is connected to the ESU via a DC-DC converter.

This chapter contains four parts:

1. In Section 5.2, the selection of the rectifier is discussed and the input resistance of a

charging capacitor is investigated as a function of time.

2. In Section 5.3, a switch mode power converter is developed as a matching network to accelerate the charging speed of a capacitor
3. An energy management unit with ultra-low power consumption is designed in Section 5.4 which includes an under voltage lockout and a DC-DC converter.
4. In Section 5.5, an experiment is conducted to power a commercial wireless sensor by a bow-tie coil, a voltage doubler, a switch mode power converter and an energy management unit.

## 5.2 The Investigation of Input Impedance

### 5.2.1 Rectifier Design

There have been various types of rectifier topologies such as single-series diode rectifiers, single-shunt diode rectifiers, voltage multipliers, and bridge type rectifiers. As discussed in Chapter 2, a free-standing coil has a low output voltage due to the demagnetization and low magnetic field strength. Thus, the output voltage must be boosted before it can be used to power electronics.

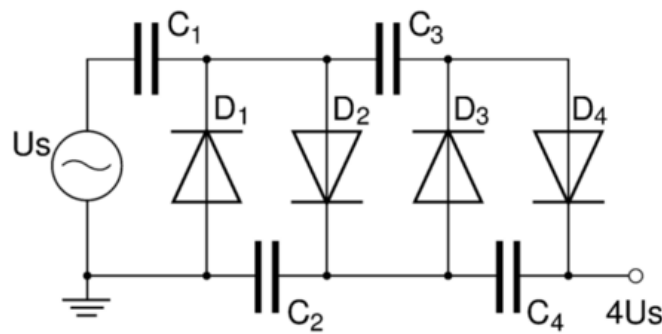


Fig. 5.3. Crockcroft-Walton voltage multiplier [20]

Crockcroft-Walton voltage multipliers (also known as voltage multipliers for short) employ the charge pump principle to accumulate a DC voltage on capacitors from an AC voltage source [1]. Schottky diodes are used as switches due to the low forward bias voltage. When the input voltage from the coil is relatively small, many stages of multiplication can be applied to boost the voltage to a desired level. However, the energy conversion efficiency degrades as the number of stages increases due to the increased number of diodes. The Crockcroft-Walton doubler (known as voltage doubler for simplicity) is an effective solution by compromising the low input voltage and the energy conversion efficiency. It provides full-wave rectification but uses less diodes (hence less energy losses) compared to a conventional bridge rectifier. Fig. 5.4 shows a voltage doubler connected to a harvesting coil and a resistive load. The capacitor  $C_1$  connected in series of the coil has two functions:

1. Compensate the self-inductance of the harvesting coil
2. Act as the series capacitor in the voltage doubler

In the negative clock cycle, the diode  $D_2$  is turned off and the load is isolated from the voltage source. Meanwhile, the diode  $D_1$  is turned on and the capacitor  $C_1$  is charged as shown in Fig. 5.4 (a). In the positive clock cycle,  $D_1$  is reverse-biased and the current flows from the coil to the load resistor as shown in Fig. 5.4(b). As  $C_1$  is already charged in the negative clock cycle, the voltage added on the load is roughly doubled the value of the input coil voltage [21]. The waveform of the voltage on the load resistor is plotted in Fig. 5.5 where  $V_p$  is the peak value of the coil voltage,  $V_f$  is the forward-bias voltage across the diode and the smoothing capacitor  $C_s$  is ignored from the circuit.

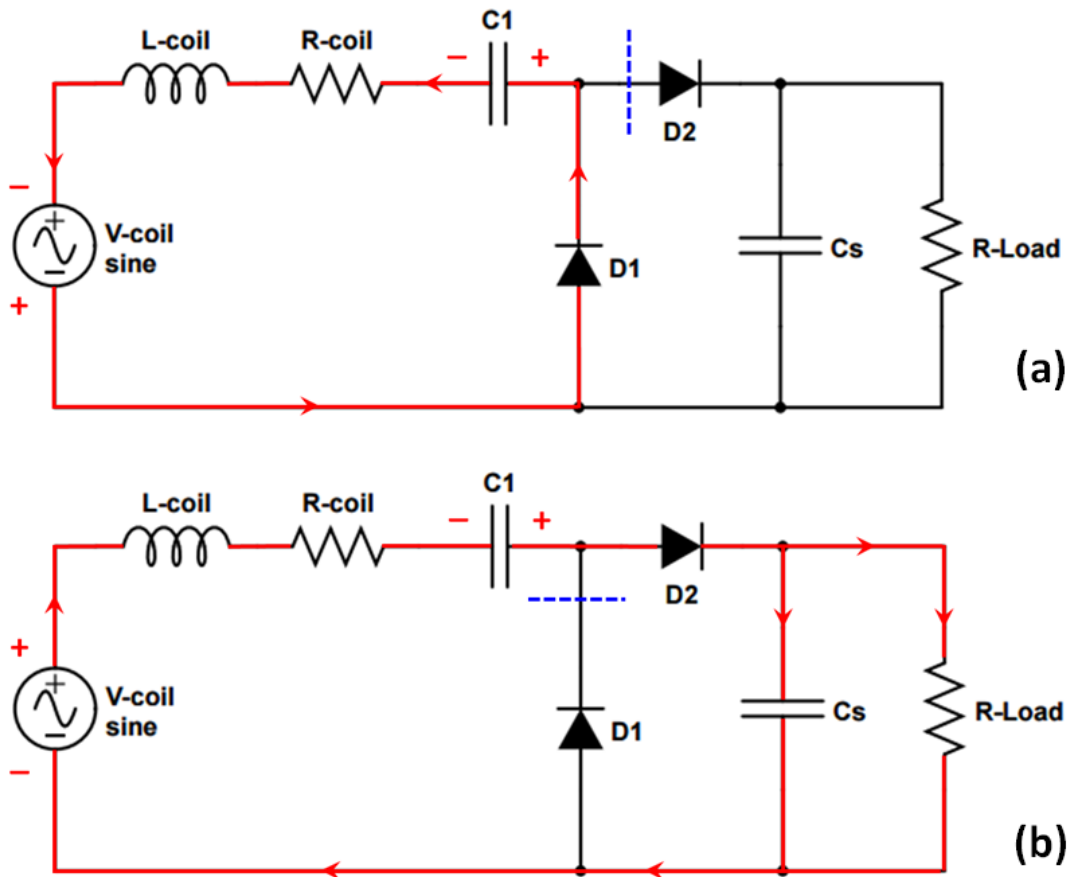


Fig. 5.4. The voltage doubler connected to a harvesting coil

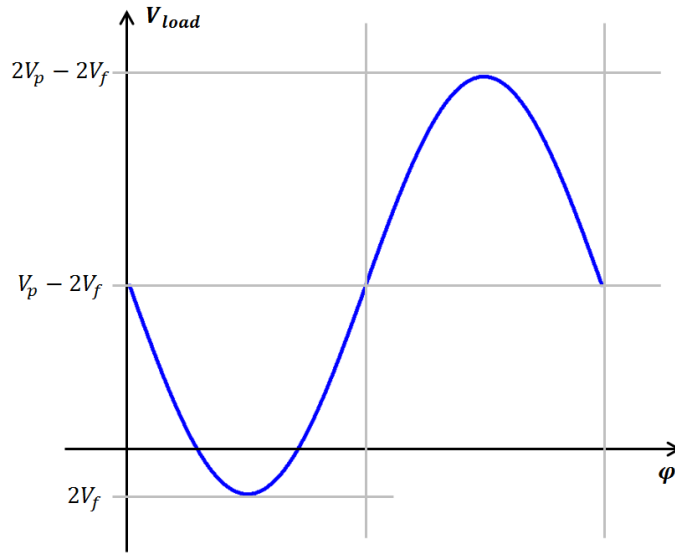


Fig. 5.5. The waveform of the voltage on the load resistor

## 5.2.2 The Input Impedance of a Resistive Load

Before designing a matching network, it is necessary to identify the source impedance  $Z_{source}$  and calculate the input impedance  $Z_{in}$  looking from the coil as shown in Fig. 5.6. The source impedance can be easily expressed at the frequency domain by:

$$Z_{source} = R_{coil} + j\omega L_{coil} \quad (5.1)$$

where  $R_{coil}$  is the effective coil resistance at the power frequency (50/60 Hz),  $L_{coil}$  is the coil inductance in the unit of H and  $\omega$  is the angular frequency in rad/s.

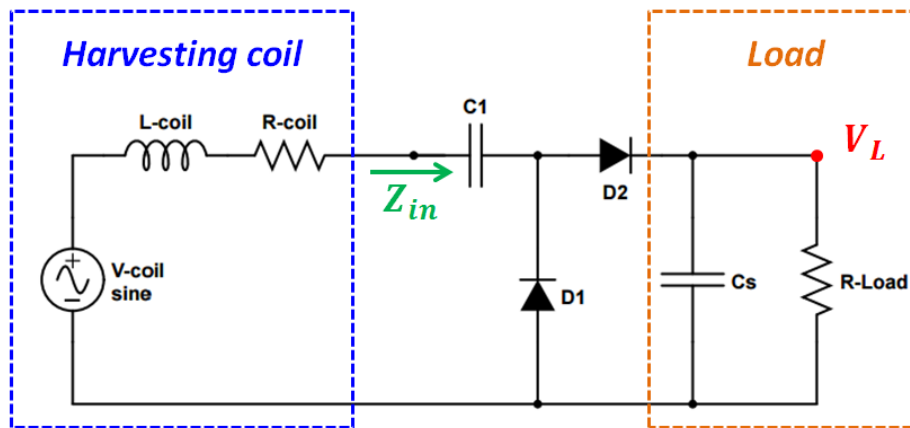


Fig. 5.6. The input impedance looking from the harvesting coil

The input impedance depends not only on the circuit topology but also on how the circuit is operated. In this section, a typical resistive load in parallel with a smoothing capacitor is analyzed and the circuit diagram is plotted in Fig. 5.6. Due to the present of the diode  $D_2$ , in the ideal case, no current can flow from the load back to the harvesting coil. Thus, the imaginary-part of the input impedance is purely determined by the capacitor  $C_1$  in the voltage doubler:

$$\text{img}(Z_{in}) = \frac{1}{j\omega C_1} \quad (5.2)$$

In the steady stage, the capacitor  $C_s$  is only used for voltage smoothing and does not consume any real energy. The real-part of the input impedance (input resistance) is a function of the diode characteristics and the load resistor  $R_{load}$ . If there is a voltage  $V_{in}$  (rms) applied to the voltage doubler, the voltage on the load resistor  $V_{load}$  (rms) is roughly:

$$V_{load} \approx 2V_{in} - 2V_f \quad (5.3)$$

where  $V_f$  is the forward bias voltage of the diode. The power on the load resistor can be derived by applying Ohm's law:

$$P_{load} = \frac{(2V_{in} - 2V_f)^2}{R_{load}} \approx \frac{4(V_{in})^2}{R_{load}} \quad (5.4)$$

By using the Schottky diode, the forward bias voltage  $V_f$  can be easily reduced to 0.32 V [22]. When the input coil voltage  $V_{in}$  is much bigger than 0.32 V,  $V_f$  can be ignored from Equation (5.4). The total power delivered to the voltage doubler can be expressed by:

$$P_{in} = \frac{V_{in}^2}{R_{in}} = P_{load} + 2P_{diode} \approx P_{load} \quad (5.5)$$

where  $P_{diode}$  is the power losses of the diode. As the Schottky diode has a low  $V_f$ ,  $P_{diode}$  is normally ignored compared to the power delivered to the load resistor. Combining Equations (5.4) and (5.5), the input resistance  $R_{in}$  can be calculated:

$$R_{in} = \frac{V_{in}^2}{P_{load}} \approx \frac{R_{load}}{4} \quad (5.6)$$

The input impedance looking from the coil can be obtained by:

$$Z_{in} \approx \frac{R_{load}}{4} + \frac{1}{j\omega C_1} \quad (5.7)$$

To validate this derivation, Advanced Design System (ADS) is used as a simulation tool. The input coil voltage  $V_{in}$  is set to 10 V<sub>rms</sub> and a Schottky diode with a forward bias voltage  $V_f$  of 0.32 V is used [22]. Therefore,  $V_{in}$  is much bigger than  $V_f$ . The coil inductance  $L_{coil}$  is set to 1000 H and the capacitor  $C_1$  is configured to 101 nF so that  $L_{coil}$  and  $C_1$  are resonant at 50 Hz. A power meter is added in series of the load resistor  $R_{load}$  to measure the power consumption  $P_{load}$ . Finally,  $R_{load}$  is optimized by the software to maximize  $P_{load}$  and the optimization results are listed in Table 5.1. When the load resistance  $R_{load}$  is roughly four times as big as the coil resistance  $R_{coil}$ , maximum energy can be transferred from the coil into the load resistor, which proves Equation (5.6) is indeed correct.

**Table 5.1: The optimized load resistance as a function of the coil resistance**

| $R_{coil}$ (k $\Omega$ ) | $P_{in}$ (mW) | Optimized $R_{load}$ (k $\Omega$ ) | $R_{load}/R_{coil}$ | Energy conversion efficiency |
|--------------------------|---------------|------------------------------------|---------------------|------------------------------|
| 5                        | 5             | 20.92                              | 4.18                | 92.6%                        |
| 10                       | 2.5           | 41.85                              | 4.18                | 92.5%                        |
| 15                       | 1.67          | 62.42                              | 4.16                | 92.3%                        |
| 20                       | 1.25          | 83.74                              | 4.19                | 91.9%                        |
| 25                       | 1             | 105.2                              | 4.20                | 90.9%                        |
| 30                       | 0.83          | 125.03                             | 4.17                | 89.3%                        |
| 35                       | 0.71          | 142.92                             | 4.08                | 87.6%                        |

### 5.2.3 The Input Impedance of a Charging Capacitor

In general cases, the power harvested from the magnetic field is only around several milliwatts or even smaller [1, 19]. The typical energy consumption of a wireless sensor is around hundred milliwatts when it is transmitting data via the wireless link [23]. As a result, the energy harvested from the coil should be accumulated in an energy storage unit first before powering a wireless device. Capacitors and rechargeable batteries are the common energy storage devices. The capacitor has a longer lifetime compared to the rechargeable battery in terms of charge cycles and can operate under a wide range of temperatures [24].



The capacitor has a disadvantage of a smaller energy density compare to the rechargeable battery. However, only one or two Joule energy is big enough for most of small wireless sensors to sense the data and transmit to the receiver [23]. Therefore, a capacitor is a suitable choice for the application of self-powered wireless sensors.

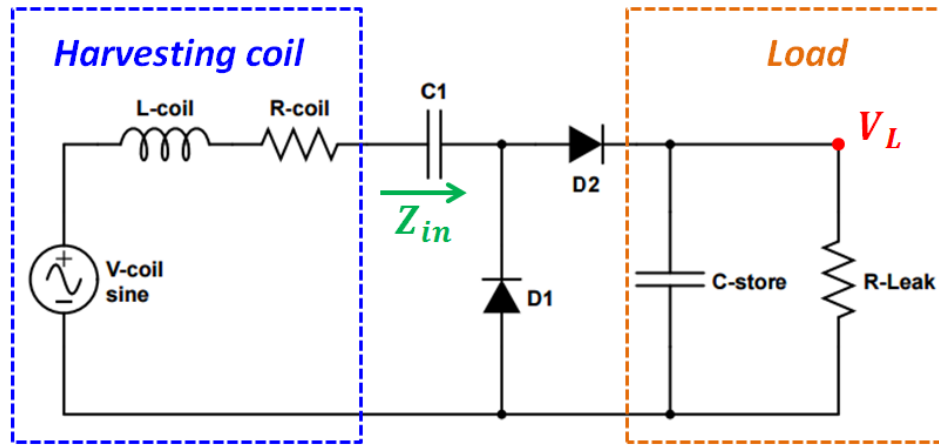


Fig. 5.7. A charging capacitor and a leakage resistance connected to the voltage doubler

Fig 5.7 shows a storage capacitor is charged by a harvesting coil via a voltage doubler. Although the circuit topology is exactly the same as the circuit in Fig 5.6, they work in totally different ways. The capacitor  $C_{store}$  in Fig 5.7 is an energy storage device compared to the smoothing capacitor  $C_s$  in Fig. 5.6. During the charging process, the energy management unit is turned off and the wireless sensor is in sleep mode. The leakage resistor  $R_{leak}$  in Fig 5.7 is used to model the leakage current in energy management unit as well as the wireless sensor. The main difference between the two circuits is the energy flow. To charge a capacitor, obviously the majority of the energy should flow into  $C_{store}$  while the leakage resistance  $R_{leak}$  should be maximized to reduce the energy losses. For a resistive load in Fig 5.6, ideally all the energy should be consumed by the load resistor  $R_{load}$  and the smoothing capacitor  $C_s$  is only used as a voltage regulator.

As the circuit for charging a capacitor works differently from a resistive load with a smoothing capacitor, a new method is investigated to determine the input resistance looking from the coil. The frequency domain analysis is not valid for this problem because the voltage of the storage capacitor  $C_{store}$  is always a function of the time. Therefore, the transient analysis is applied to calculate the voltage of the capacitor  $C_{store}$  and the input resistance  $R_{in}$

as a function of time. To simplify the circuit mode, the harvesting coil with a voltage doubler can be approximately equivalent to a voltage source  $V_s$  in series of a resistor  $R_s$  and a diode  $D$  shown in Fig. 5.8. The new voltage source  $V_s$  and the source resistance  $R_s$  can be expressed by:

$$V_s \approx 2V_{coil} - V_f = A\sin(\omega t) \quad (5.8)$$

$$R_s = R_{coil} \quad (5.9)$$

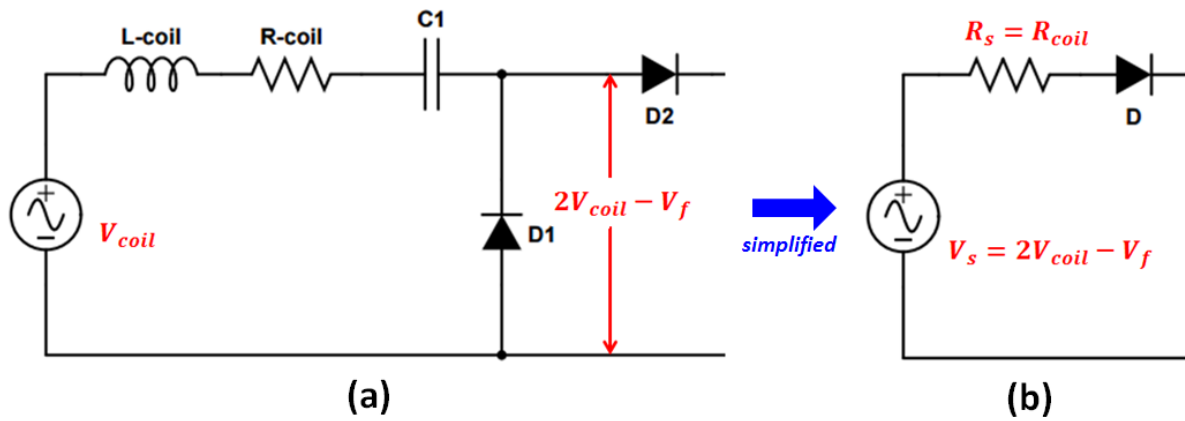


Fig. 5.8. The simplified circuits of a harvesting coil with a voltage doubler

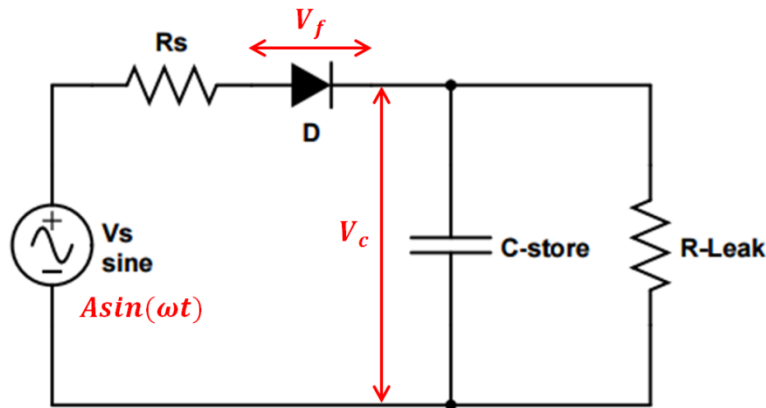
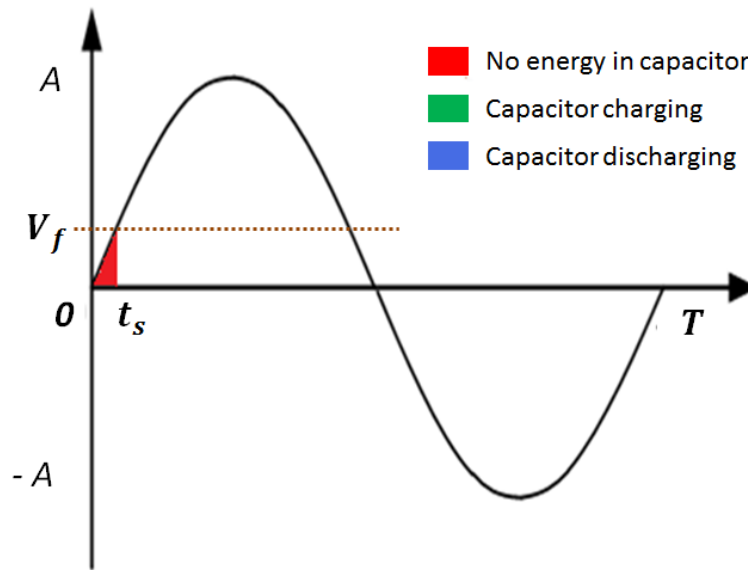


Fig. 5.9. The equivalent half-wave rectifier connected with a storage capacitor and a leakage resistor

The completed equivalent circuit is shown in Fig. 5.9 and the voltage source is a 50 Hz sine wave with the amplitude of  $A$ . To further reduce the complexity of the calculation, the diode in this circuit is treated as an ideal one with a fixed turn-on voltage  $V_f$  and its reverse current is totally ignored. For the transient analysis, the initial state of the circuit is of great importance and should be clearly declared. When the time is 0 second, the voltage on the storage capacitor is zero. The whole transient analysis can be divided into three different

periods: the circuit initialization period, the capacitor charging period and the capacitor discharging period.

### ***A. The circuit initialization period***



**Fig. 5.10. The circuit initialization period**

The initialization period starts from 0 second and no current flows in the circuit as the diode is in the reverse bias. The storage capacitor  $C_{store}$  is neither charged nor discharged and its voltage is still 0 V. This period ends at the time  $t_s$  when the source voltage  $V_s$  equal to the diode forward bias  $V_f$ .

$$t_s = \frac{\arcsin\left(\frac{V_f}{A}\right)}{\omega} \quad (0 \leq t_s \leq T) \quad (5.10)$$

The time  $t_s$  therefore becomes the initial conditions for the next transient state analysis.

### ***B. The capacitor charging period***

When the source voltage  $V_s$  is higher than the voltage of the capacitor  $V_c$  plus the diode turn-on voltage  $V_f$ , the capacitor starts to charge and its voltage goes up. According to the Kirchhoff's Voltage Law (KVL), the equation below can be derived:

$$V_c + V_f + \left( C_{store} \frac{dV_c}{dt} + \frac{V_c}{R_{Leak}} \right) R_s - A \sin(\omega t) = 0 \quad (5.11)$$

Where  $V_c$  is the voltage of the storage capacitor,  $C_{store}$  is the value of the storage capacitor in F,  $t$  is the time in the unit of seconds,  $R_s$  is the source resistance in  $\Omega$ ,  $A$  is the amplitude of the voltage source and  $\omega$  is the frequency in the unit of rad/s.

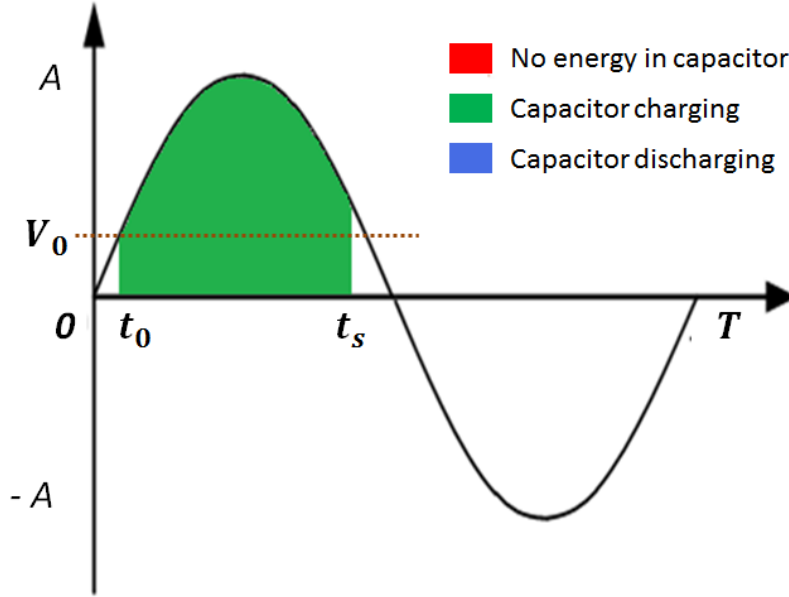


Fig. 5.11. The capacitor charging period

By rearranging Equation (5.11):

$$R_s C_{store} \frac{dV_c}{dt} + \left( 1 + \frac{R_s}{R_{Leak}} \right) V_c = A \sin(\omega t) - V_f \quad (5.12)$$

Assuming the time constant  $\tau = R_s C_{store}$  and  $a = 1 + \frac{R_s}{R_{Leak}}$ , it becomes a first order ordinary differential equation:

$$\tau \frac{dV_c}{dt} + a V_c = A \sin(\omega t) - V_f \quad (5.13)$$

By solving this equation,  $V_c$  can be expressed as the function of time  $t$ :

$$V_c = \frac{A}{\frac{a^2}{\tau} + \omega^2 \tau} \left( \frac{a}{\tau} \sin \omega t - \omega \cos \omega t \right) - V_f - A \frac{e^{\frac{a(t_0-t)}{\tau}}}{\frac{a^2}{\tau} + \omega^2 \tau} \left( \frac{a}{\tau} \sin \omega t_0 - \omega \cos \omega t_0 \right) + \left( \frac{V_f}{a} + V_0 \right) e^{\frac{a(t_0-t)}{\tau}} \quad (t_0 \leq t \leq t_s) \quad (5.14)$$

$t_0$  is the time when the capacitor begins to charge and  $V_0$  is the voltage of the capacitor at the time  $t_0$ . The charging period stops at the time  $t_s$  when the voltage of the capacitor  $V_c$  equals to the source voltage  $V_s$  minus the diode forward bias  $V_f$ .

$$V_c = A \sin \omega t_s - V_f \quad (0 \leq t_s \leq T) \quad (5.15)$$

$$t_s = \frac{\arcsin\left(\frac{V_c + V_f}{A}\right)}{\omega} \quad (0 \leq t_s \leq T) \quad (5.16)$$

The time  $t_s$  and its instantaneous voltage of the capacitor  $V_c$  become the initial conditions for the next transient state analysis.

### *C. The capacitor discharging period*

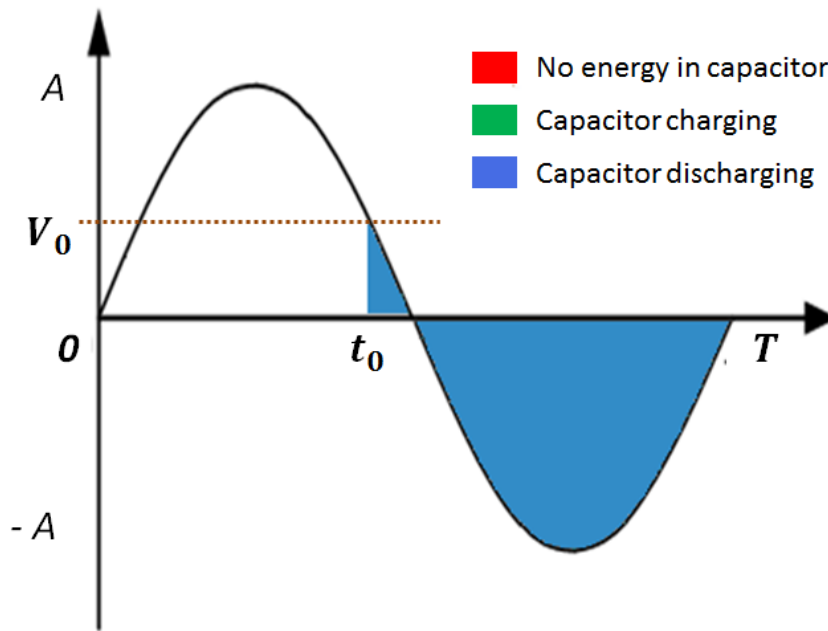


**Fig. 5.12. The capacitor discharging period I**

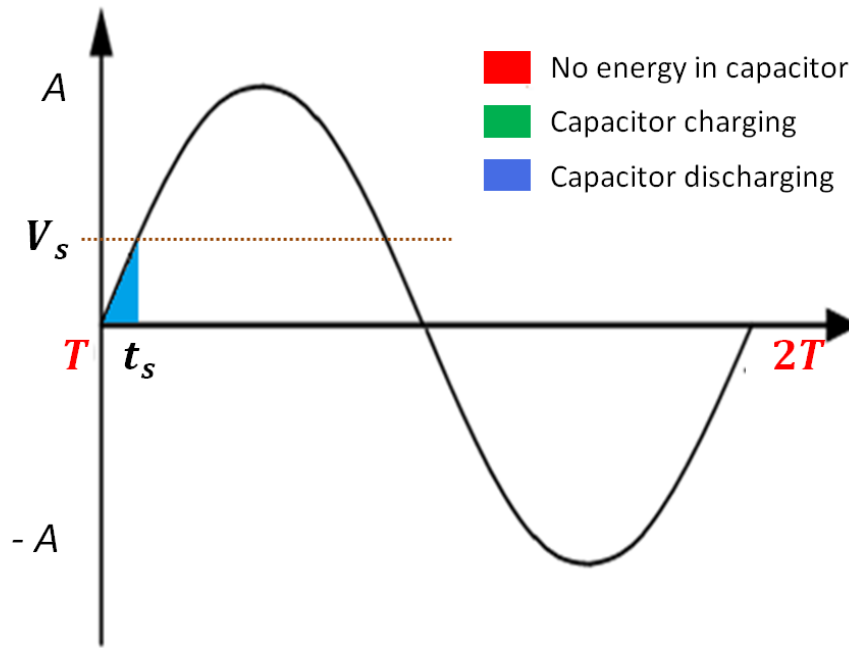


**Fig. 5.13. The capacitor discharging period II**

When the charging period is finished and the diode is in the reverse-bias, the storage capacitor  $C_{store}$  is totally isolated from the voltage source. In this case, the circuit becomes a classic  $RC$  discharge problem. By applying the Kirchhoff's Voltage Law (KVL) again, the equation below can be derived:

$$V_c + R_{Leak} C_{store} \frac{dV_c}{dt} = 0 \quad (5.17)$$

Rearrange the equation:

$$-\int_{t_0}^t \frac{1}{R_{Leak} C_{store}} dt = \int_{V_0}^{V_c} \frac{1}{V_c} dV_c \quad (5.18)$$

$V_c$  can be derived as a function of time  $t$  by:

$$V_c = V_0 e^{(t_0-t)/(R_{Leak} C_{store})} \quad (t_0 \leq t \leq t_s) \quad (5.19)$$

The discharging continuous until the input source voltage  $V_s$  equals to the capacitor voltage  $V_c$  plus the diode forward bias  $V_f$ .  $t_s$  is the time when the capacitor stops discharging and can be calculated as follow:

$$A \sin(\omega t_s) = V_c + V_f \quad (T \leq t_c \leq 2T) \quad (5.20)$$

$$t_s = \frac{\arcsin\left(\frac{V_c + V_f}{A}\right)}{\omega} \quad (T \leq t_c \leq 2T) \quad (5.21)$$

The time  $t_s$  and its instantaneous capacitor voltage  $V_c$  become the initial conditions for the next transient state analysis. In the next stage, the diode is turned on and the capacitor begins to charge again. The transient analysis for the capacitor charging derived in the previous section can be applied again. The charging and discharging cycle takes place by turn until the circuit reaches to its steady state. Under this condition, in each clock cycle, the energy delivered from the voltage source to the capacitor should be the same of the energy that the capacitor discharges to the leakage resistor.

From Equation (5.10) to Equation (5.21), the voltage on the storage capacitor  $V_c$  is derived as a function of time and an example is plotted in Fig. 5.14. The theoretical results agree well with the simulated ones from ADS.

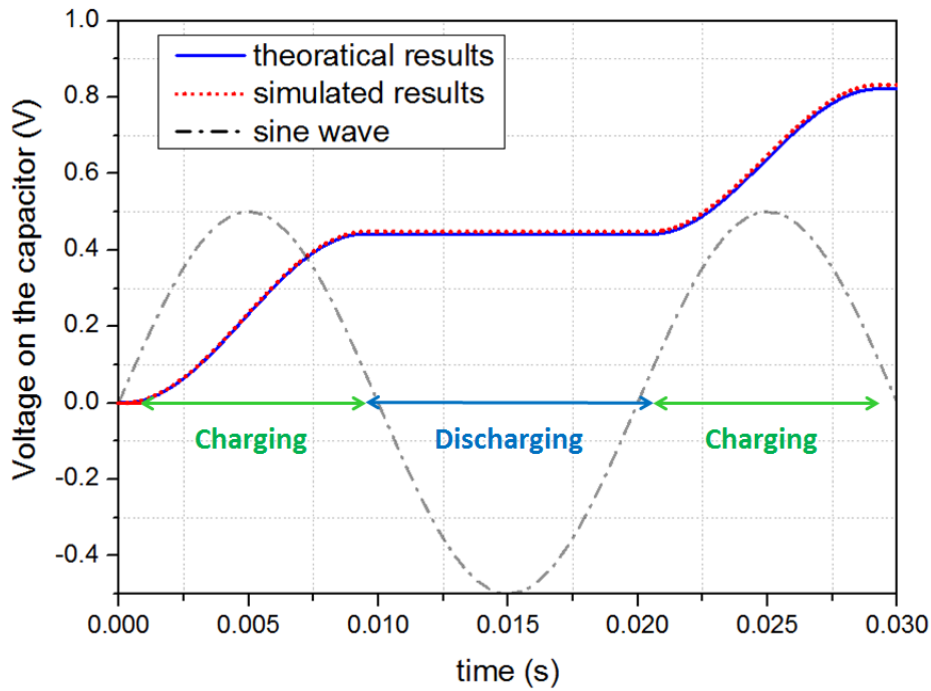


**Fig. 5.14.** The voltage on the storage capacitor as a function of time when  $A = 5$  V,  $R_s = 6$  k $\Omega$ ,  $C_{store} = 10$   $\mu$ F,  $V_f = 0.32$  V and  $R_{leak} = 500$  k $\Omega$

Based on the equations derived above, the current  $I_s(t)$  flowing out of the voltage source can be obtained:

$$I_s(t) = \frac{V_s(t) - V_f - V_c(t)}{R_s} = \frac{A \sin(\omega t) - V_f - V_c(t)}{R_s} \quad (5.22)$$

Therefore, the input resistance  $R_{in}$  looking from the voltage source is also a function of time and can be calculated by:

$$R_{in}(t) = \frac{V_c(t) + V_f}{I_s(t)} = \frac{(V_c(t) + V_f)R_s}{A \sin(\omega t) - V_c(t) - V_f} \quad (5.23)$$

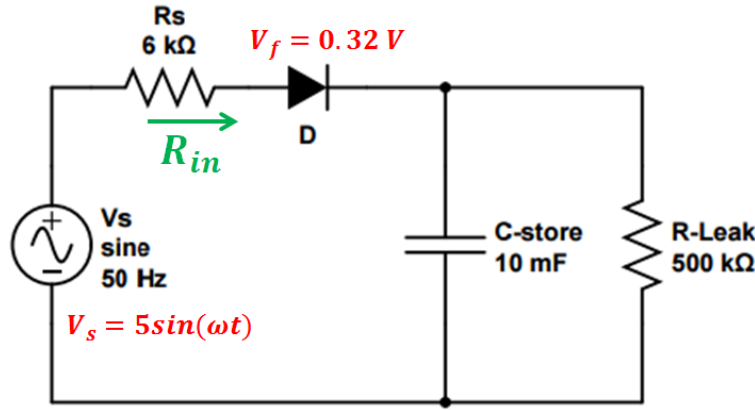


Fig. 5.15. The circuit configuration for the investigation of the input resistance

To explore how the input resistance  $R_{in}$  changes with time  $t$ , a case study is conducted and the circuit configuration is shown in Fig. 5.15. The storage capacitor is set to a large value (10 mF) intentionally so that in each clock cycle the voltage of the capacitor does not change significantly. The input resistance  $R_{in}$  in the first clock cycle is plotted in Fig. 5.16. During the charging process, the input resistance varies significantly from 410  $\Omega$  to more than 12 k $\Omega$ . At the time when the capacitor begins to charge or finishes charging ( $V_s = V_c + V_f$ ), the input resistance  $R_{in}$  becomes infinitely large as almost no current can flow into the storage capacitor. However, when the source voltage  $V_s$  reaches to its peak value ( $t = 5$  ms), the voltage difference between  $V_s$  and  $V_c$  is maximized and therefore the input resistance has its minimum value  $\overline{R_{in}}$  in this clock cycle. At this specific time ( $t = 5$  ms in this case), maximum energy can be transferred from the source to the storage capacitor. To accelerate the charging speed, the source resistance  $R_s$  should be matched to  $\overline{R_{in}}$  in each clock cycle during the charging time. In Fig. 5.17, the minimum input resistance  $\overline{R_{in}}$  in each clock cycle is plotted and the charging time is configured to 10 minutes. As the voltage of the capacitor continues to go up,  $\overline{R_{in}}$  increases from 410  $\Omega$  to 31.6 k $\Omega$ .



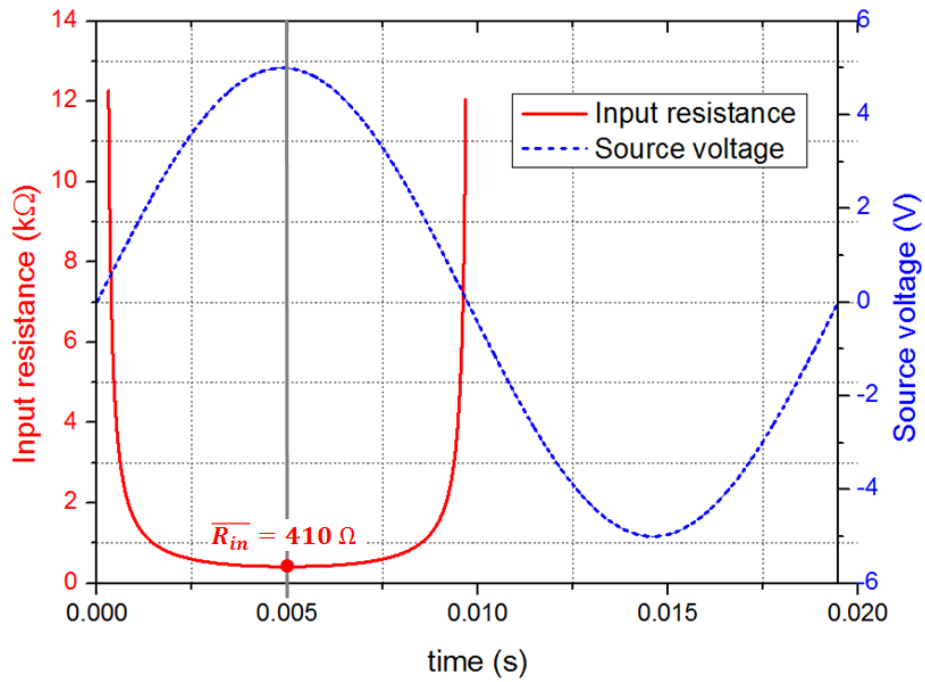


Fig. 5.16. The input resistance in the first clock cycle

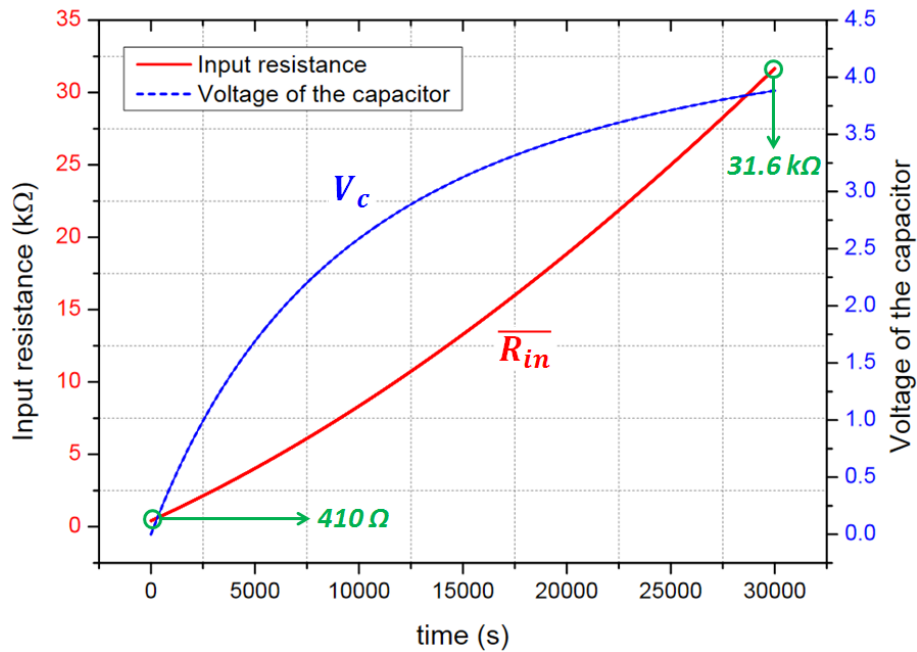
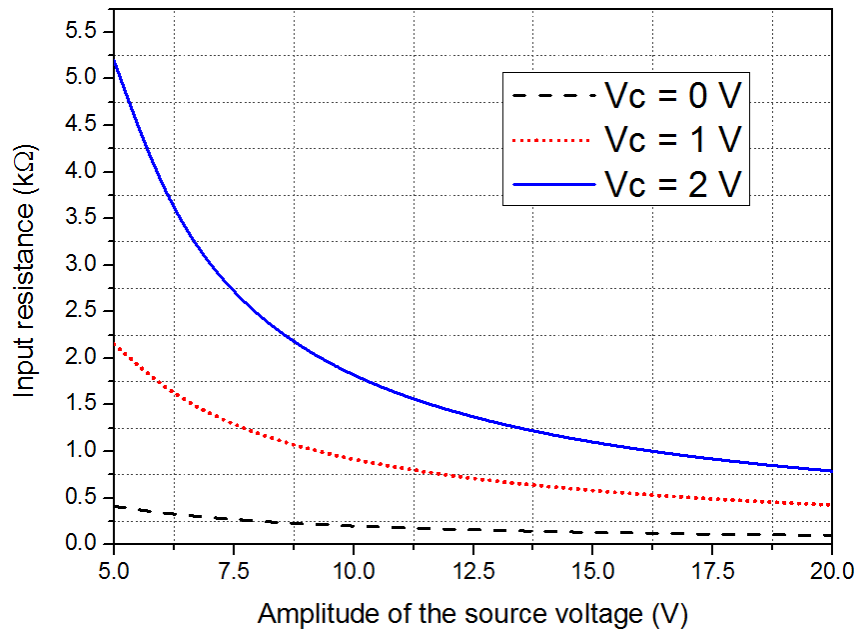


Fig. 5.17. The minimum input resistance in each clock cycle as a function of time

Furthermore, according to Equation (5.23), the input resistance is not only a function of time but also depends on the amplitude of the source voltage  $A$ . As the magnetic field applied to the harvesting coil may varies from time to time, the amplitude of the coil voltage will

change correspondingly. We assume that at a specific time, the capacitor has a voltage of  $V_c$  and the source voltage has amplitude of  $A$ . The instantaneous input resistance is plotted in Fig. 5.18 as a function of the amplitude. It can be concluded that the input impedance of a charging capacitor is determined by the coil voltage as well as the voltage of the capacitor.



**Fig. 5.18.** The input resistance as a function of the input and output voltage

### 5.3 Matching Circuit Design of a Charging Capacitor

A transient analysis has been conducted in Section 5.2 to investigate the input resistance of a charging capacitor as a function of time. It can be concluded that the input resistance varies significantly with the voltage of the charging capacitor as well as the coil voltage. Therefore, it is extremely difficult to use conventional linear components to design a proper matching circuit as the inductance and the capacitance is only a function of the frequency. A more advanced matching network consisted of nonlinear components (e.g. switches, diodes, transistors, etc.) may be required to tackle this problem.

Switched mode power converters are used in kinetic energy harvesters to provide voltage boosting and rectification [25-28]. The current flow in a circuit can be properly controlled by varying the gate signal applied on the switch. A similar idea can be applied to design a power converter as a matching network which is able to emulate a constant input resistance regardless of the input and output voltages. The proposed circuit topology is shown in Fig. 5.18. The storage capacitor  $C_{store}$  can be totally isolated from the voltage source by the switch mode power converter. As the storage capacitor is not directly connected to the voltage source, the input resistance can be independent of the input and output voltages if a proper power converter is designed.

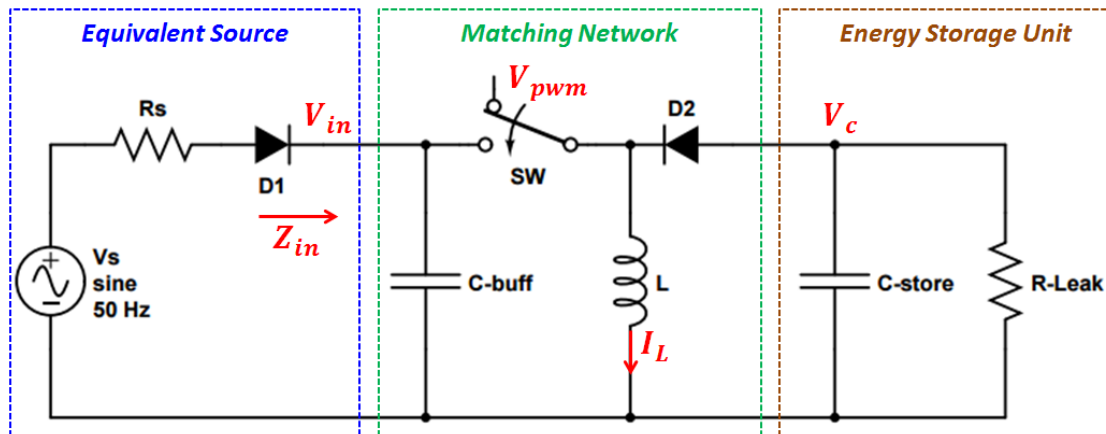


Fig. 5.18. The circuit topology of a switched mode matching network

The power converter consists of a capacitor  $C_{buff}$ , a switch  $SW$ , an inductor  $L$  and a Schottky diode  $D_2$ . The switch is the key component and controlled by a power width modulation

(PWM) with a switching frequency of  $f_{sw}$  and a duty cycle of  $D_{sw}$ . The switching frequency  $f_{sw}$  is usually in the order of kHz which is hundred times higher than the power frequency (50/60 Hz). The inductor  $L$  is used as a temporary energy storage medium to collect the energy from the voltage source and discharge to the storage capacitor. The capacitor  $C_{buff}$  acts as a voltage regulator and ideally does not consume real energy. The working principle of this power converter is illustrated in Fig. 5. 19 and Fig. 5.20

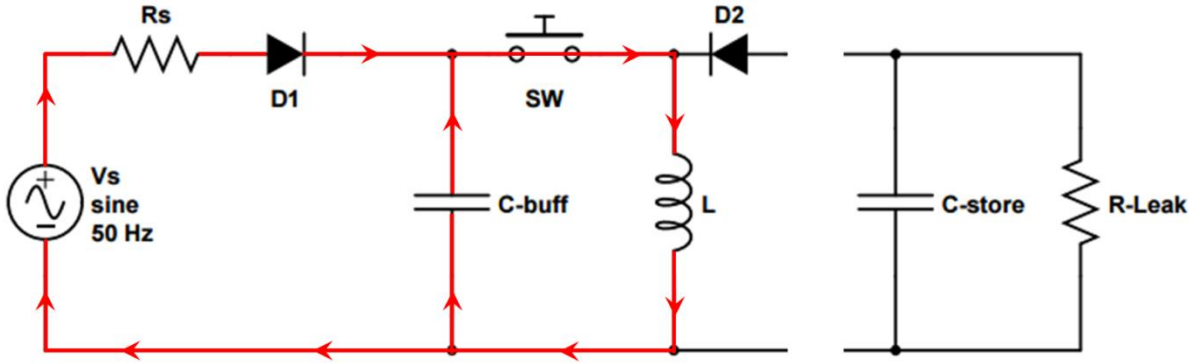


Fig. 5.19. The current flow during the ON time of the switching period

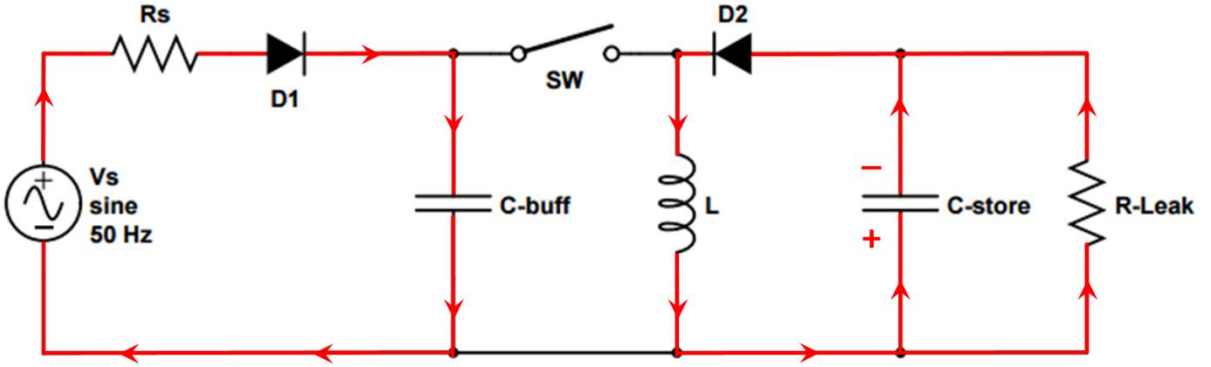


Fig. 5.20. The current flow during the OFF time of the switching period

During the ON time of the switching period, the diode  $D_2$  is in the reverse bias and the storage capacitor  $C_{store}$  is isolated from the voltage source. The inductor  $L$  is charged by the voltage source as shown in Fig. 5.19. The current in the inductor can be correlated to the time by:

$$V_{in} = L \frac{dI_L}{dt} \quad (5.24)$$

where  $I_L$  is the current in the inductor in the unit of amperes. The capacitor  $C_{buff}$  is

configured to a relatively big value (in the order of  $\mu\text{F}$ ) so that, in each switching period, the input voltage  $V_{in}$  can be treated as a constant. Thus, the current  $I_L$  is linearly proportional to the time  $t$  as shown in Fig. 5.21 and the slope  $k_{up}$  can be calculated by:

$$k_{up} = \frac{dI_L}{dt} = \frac{V_{in}}{L} \quad (5.25)$$

Suppose that at the beginning of every switching period, the current in the inductor  $I_L$  is always zero. At the time when the switch is about to be turned OFF, the inductor can have a maximum current  $I_{peak}$ :

$$I_{peak} = k_{up} D_{sw} T_{sw} = \frac{V_{in} D_{sw} T_{sw}}{L} \quad (5.26)$$

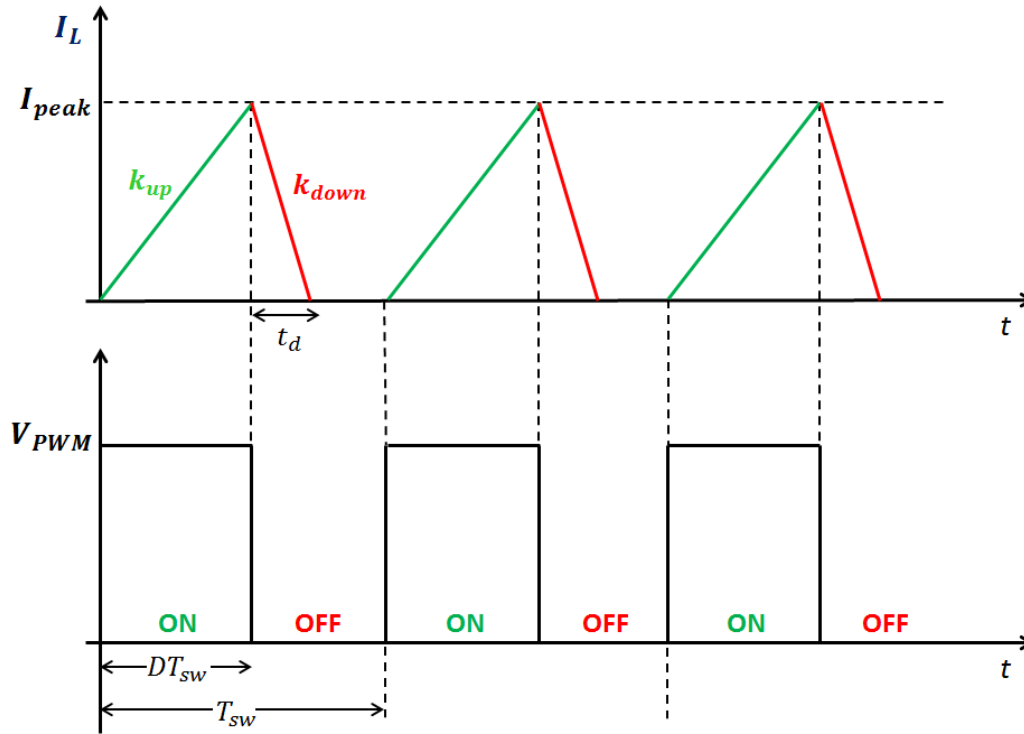


Fig. 5.21. The current flow during the ON time of the switching period

During the OFF time of the switching period, the inductor is isolated from the voltage source and carries an initial current of  $I_{peak}$ . Due to the natural property of an inductor, its current continues to flow in its previous direction so that the storage capacitor can be charged. Fig. 5.20 shows the current flow in the circuit when the switch is turned off. The voltage of the storage capacitor  $V_c$  can be derived by:

$$V_c = -L \frac{dI_L}{dt} \quad (5.27)$$

The slope of the inductor discharging  $k_{down}$  can be obtained by:

$$k_{down} = -\frac{dI_L}{dt} = -\frac{V_c}{L} \quad (5.28)$$

The time interval  $t_d$  shown in Fig. 5.21 is the total time that all the current in the inductor is fully discharged to the storage capacitor.  $t_d$  can be calculated by:

$$t_s = \frac{I_{peak}}{k_{down}} = \frac{I_{peak}L}{V_c} \quad (5.29)$$

By selecting a suitable value for the inductor  $L$ , the switching period  $T_{sw}$  and the duty cycle  $D_{sw}$ , the time interval  $t_s$  can be smaller than the OFF time of the switching period  $(1 - D_{sw})T_{sw}$  and the power converter is operated in discontinues conduction mode (DCM). In other words, during the OFF time of the switching period, all the current in the inductor can be fully discharged. Therefore, in the beginning of every ON time, the current in the inductor  $I_L$  is always zero as shown in Fig. 5.21. As a result, in each switching period, the average current  $\overline{I_{in}}$  flowing out of the voltage source can be calculated by:

$$\overline{I_{in}} = \frac{I_{peak}D_{sw}T_{sw}}{2T_{sw}} = \frac{V_{in}D_{sw}^2T_{sw}}{2L} \quad (5.30)$$

The emulated input resistance  $\overline{R_{in}}$  looking into the power converter is defined as:

$$\overline{R_{in}} = \frac{V_{in}}{\overline{I_{in}}} = \frac{2L}{D_{sw}^2T_{sw}} \quad (5.31)$$

It is noted that the resistance emulated by the power converter can be assumed as a constant if the switching frequency and the duty cycle are kept unchanged. By using a correct combination of the inductor  $L$ , the switching frequency  $f_{sw}$  and the duty cycle  $D_{sw}$ , the emulated input resistance  $\overline{R_{in}}$  can be matched to the source resistance so that maximum energy can be delivered from the harvesting coil to the storage capacitor.

## 5.4 Energy Management Unit

By using a switch mode power converted, the energy conversion efficiency from the coil to the storage capacitor can be increased. However, the energy stored in the capacitor cannot be directly used to power a wireless sensor as the supply voltage of a sensor is always a fixed value. Therefore, an energy management unit shown in Fig. 5.22 is required to monitor the energy in the storage capacitor [29], protect the components from overload and provide a stable voltage output to the wireless sensor.

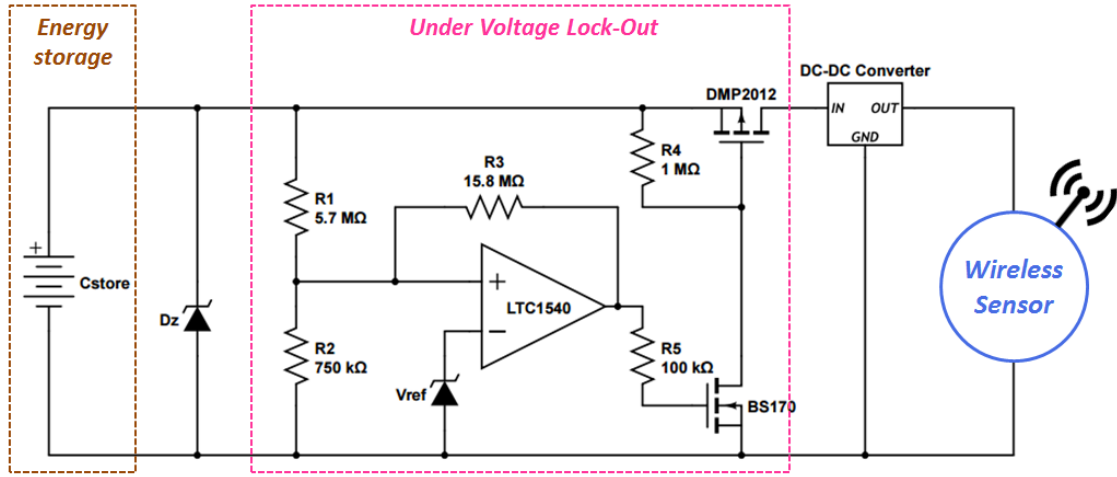


Fig. 5.22. The circuit diagram of an energy management unit

A Zener diode is connected in parallel to the storage capacitor to prevent the voltage overload. An under voltage lock-out (UVLO) is designed to monitor the voltage on the storage capacitor  $V_c$ . Once  $V_c$  is higher than the upper threshold voltage  $V_{up}$  of the UVLO, the storage capacitor is connected to a wireless sensor via a DC-DC converter. As the energy is consumed by the sensor, the capacitor voltage  $V_c$  starts to decrease. While  $V_c$  is smaller than the lower threshold voltage  $V_{low}$  of the UVLO, the storage capacitor is disconnected from the DC-DC converter and can be charged again by the harvesting coil. The working principle of the under voltage lock-out is discussed in [29]. The total energy  $E_c$  that the storage capacitor can discharge to the wireless sensor is determined by the threshold voltage  $V_{up}$  and  $V_{low}$  of the UVLO.  $E_c$  can be calculated as follows:

$$E_c = \frac{1}{2} C V_{up}^2 - \frac{1}{2} C V_{low}^2 \quad (5.32)$$

It is assumed that  $E_{sensor}$  is the minimum energy that the wireless sensor is required to operate and transmit the information to the receiver. Obviously,  $E_c$  should be higher than  $E_{sensor}$  plus the energy losses  $E_{loss}$  in the energy management unit.

$$E_c \geq E_{sensor} + E_{loss} \quad (5.33)$$

A DC-DC converter needs to be carefully selected in terms of the energy conversion efficiency, the input voltage range and the output voltage range.



## 5.5 Experimental Results and Discussions

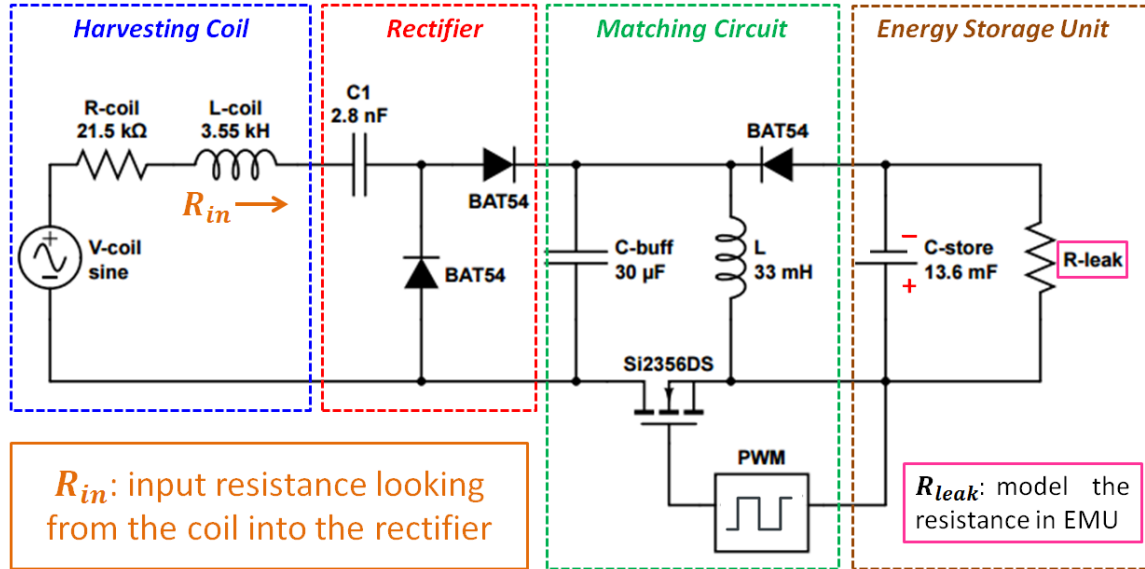


Fig. 5.23. The circuit diagram that transfers the energy from the coil into the storage capacitor

The circuit diagram implemented in the lab is shown in Fig. 5.23 which includes a harvesting coil, a voltage doubler, a matching circuit (switch mode power converter) and an energy storage unit. The bow-tie coil shown in Fig. 3.18 is used as a testing coil due to its high output voltage. It is placed in an area where the magnetic flux density is around  $7 \mu T_{rms}$  and the coil properties are summarized in Table 5.2. The Schottky diode BAT54 is used in the circuit due to its low forward bias voltage, small reverse current and high breakdown voltage [31]. The MOSFET Si2356DS is used as a switch in the power converter and is driven by a PWM from an arbitrary waveform generator [32]. A 13.6 mF electrolytic capacitor is selected as the energy storage unit as it is cheap and widely available on the market. The resistor  $R_{leak}$  represents the leakage current in the energy management unit during the capacitor charging process.

The harvesting coil has a self-inductance of 3550 H and a compensating capacitor of 20.8 nF is added to make the circuit resonant at 50 Hz. As the harvesting coil has an effective coil resistance of 21.5 kΩ and according to Equation (5.6) derived in Section 5.2, the input resistance should be four times as large as the coil resistance to achieve the maximum energy conversion efficiency. Therefore, the emulated input resistance looking into the power converter should be designed around 86 kΩ. The configuration of the switch mode power

converter is summarized in Table 5.3, which gives an emulated input resistance of 82.5 k $\Omega$ .

**Table 5.2: The properties of the bow-tie coil inside a magnetic field of 7  $\mu\text{T}_{rms}$**

| Parameters                | Values          |
|---------------------------|-----------------|
| Coil Voltage              | 7.45 $V_{rms}$  |
| Number of turns           | 103,000         |
| Effective coil resistance | 21.5 k $\Omega$ |
| Coil inductance           | 3550 H          |
| Output power              | 0.64 mW         |

**Table 5.3: The configuration of the switch mode power converter**

| Parameters                | Values          |
|---------------------------|-----------------|
| Inductance                | 33 mH           |
| Period of PWM             | 0.5 ms          |
| Duty cycle of PWM         | 4%              |
| Emulated input resistance | 82.5 k $\Omega$ |

Fig. 5.24 shows the circuit diagram of the energy management unit. A commercial wireless sensor provided by the Invisible-Systems Ltd [33] is chosen for laboratory trials. This module requires an average power of 0.72 W (0.2 A at 3.6 V) during its active operation. It takes about 400 ms to sense a temperature reading and transmit to a receiver, which gives an overall energy requirement of 288 mJ for a single operation. The threshold voltage  $V_{up}$  and  $V_{low}$  of the under voltage lock-out is set to 10.5 V and 7.7 V respectively. Thus, the energy that can be delivered to the wireless sensor is around 346 mJ which is larger than the energy required by the wireless sensor. LTC1540 from Linear Technology [34] is selected as the comparator in the UVLO due to its low power consumption and a wide range of supply voltage (2 V to 11 V). A step-down DC-DC converter MAX15020 is used to regulate the

voltage of the storage capacitor and provide a stable 3.6 V output to the wireless sensor. It has several advantages such as high energy conversion efficiency up to 96%, low power consumption in shutdown mode and a wide input range from 7.5 V to 40 V.

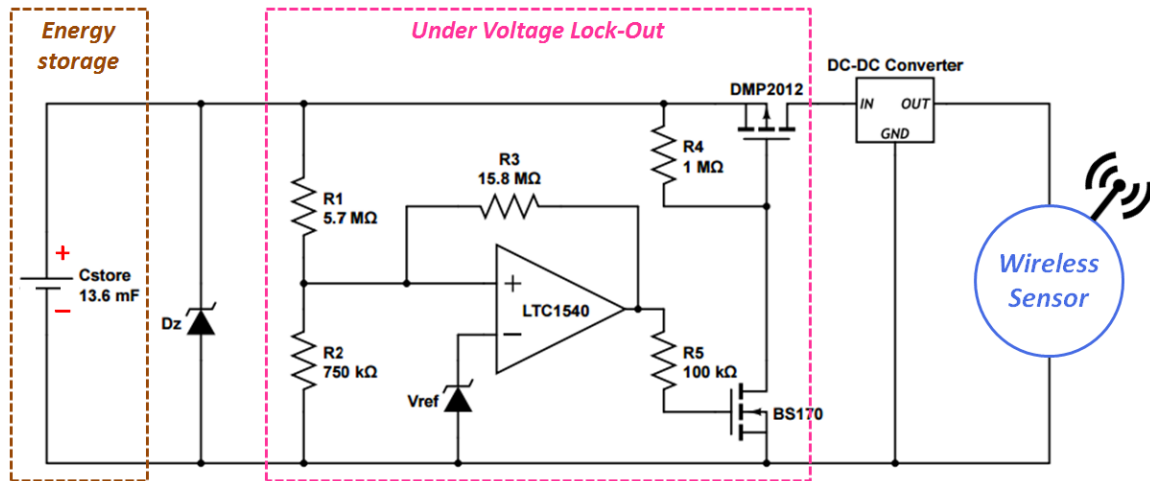


Fig. 5.24. The circuit diagram that transfers the energy from the storage capacitor to a wireless sensor

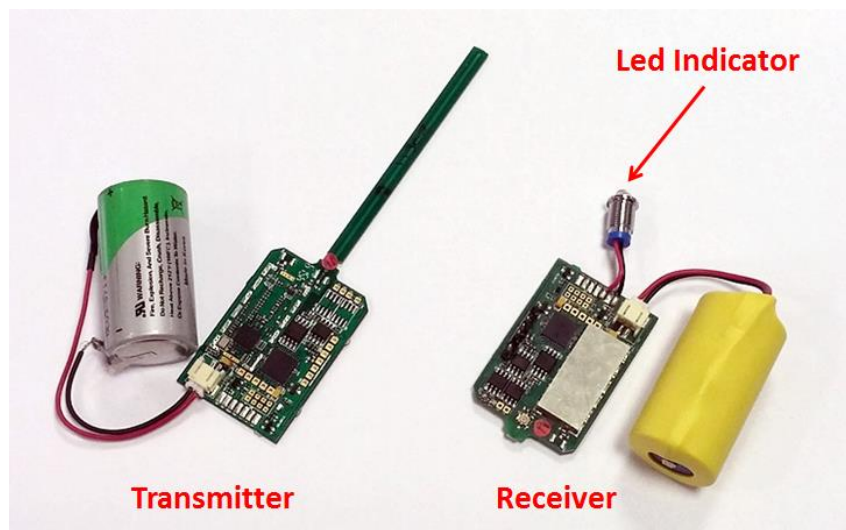


Fig. 5.25. The wireless sensor and receiver used for the experiment

Fig. 5.26 shows the measured voltage of the storage capacitor as a function of time. Before the charging process, the storage capacitor has an initial voltage of 7.7 V. When the coil is placed in an alternating magnetic flux density of  $7 \mu T_{rms}$ , the storage capacitor begins to charge and its voltage increases gradually. After 12 minutes and 12 seconds, the voltage of the capacitor reaches to 10.52 V and the under voltage lock-out is turned on. The wireless sensor is powered by the storage capacitor via a DC-DC converter. As the energy is quickly

drained by the sensor, the voltage of the capacitor decreased dramatically. When the voltage is lower than 7.7 V, the UVLO is turned off. And the storage capacitor can be charged again for the next operation.

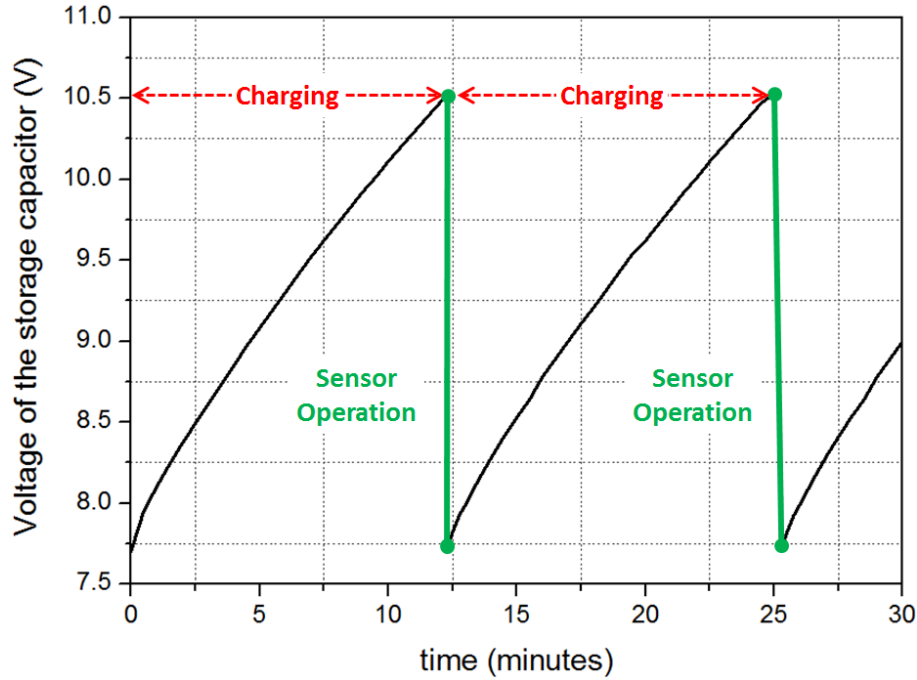


Fig. 5.26. The measured voltage of the storage capacitor as a function of time

During the charging period, 349 mJ energy is delivered from the coil to the storage capacitor. The harvesting coil is able to generate a maximum power of 0.64 mW if it is connected to a perfectly matched load. The energy conversion efficiency  $\eta$  can be calculated by:

$$\eta = \frac{E_c}{P_m \times T_c} \quad (5.34)$$

where  $E_c$  is the energy stored in the capacitor,  $P_m$  is the power that delivered to a perfectly matched load and  $T_c$  is the total charging time. In roughly 12.5 minutes (the total charging time), 468 mJ can be collected at a matched load. As a result, **the energy conversion efficiency from the harvesting coil to the storage capacitor is about 74.6 %**. The energy losses are mainly caused by the diode losses and the leakage current in the energy management unit. Nevertheless, the achieved efficiency is much higher than a previous reported design which only has the efficiency of 36 % [12].

## 5.5 Summary

In this chapter, a completed impedance matching circuit and management system has been proposed and designed to transfer the energy from the harvesting coil to a storage capacitor efficiently. It has been demonstrated that a commercial wireless sensor could be powered up by the magnetic field energy collected from the harvesting coil.

A voltage doubler has been applied to provide full-wave rectification and simultaneously boost the voltage output. Besides, it requires less diodes (hence less energy losses) compared to a conventional bridge rectifier. A transient analysis has been conducted to calculate the input resistance of a charging capacitor as a function of time and subsequently verified by the software simulation. The analysis indicated that the input resistance of a charging capacitor was dependent on the input and output voltages. Therefore, a conventional matching circuit that consisted of linear components could not work properly. A switch mode power converter was introduced as a matching network so that the storage capacitor could be isolated from the power source. The emulated input resistance looking into the power converter could be a constant and determined by the frequency and the duty cycle of the PWM applied on the switch. From the experimental results, the energy conversion efficiency from the harvesting coil to the storage capacitor was around 74.6 %, which was twice as large as a previously reported result. Finally, an energy management unit has been developed that effectively utilized the energy stored in the capacitor to power a commercial wireless sensor.

## 5.6 References

- [1] N. Roscoe and M. Judd, "Optimization of Voltage Doublers for Energy Harvesting Applications", *IEEE Sensors Journal.*, vol. 13, no. 12, pp. 4904-4911, 2013.
- [2] V. Raghunathan, A. Kansal, J. Hsu, J. Friedman, Mani Srivastava, "Design considerations for solar energy harvesting wireless embedded systems," *Information Processing in Sensor Networks*, pp. 457-462, 2005
- [3] S. Bader, B. Oelmann, "Enabling Battery-Less Wireless Sensor Operation Using Solar Energy Harvesting at Locations with Limited Solar Radiation," *4<sup>th</sup> Int. conf. on Sensor Technologies and Applications (SENSORCOMM)*, pp. 602-608, 2010
- [4] M. Weimer, T. Paing and R. Zane, "Remote area wind energy harvesting for low-power autonomous sensors", *37th IEEE Power Electronics Specialists Conference*, 2006
- [5] Y. Tan and S. Panda, "Self-Autonomous Wireless Sensor Nodes With Wind Energy Harvesting for Remote Sensing of Wind-Driven Wildfire Spread", *IEEE Transaction on Instrumentation and Measurement.*, vol. 60, no. 4, pp. 1367-1377, 2011.
- [6] H. Zangl, T. Bretterkieber and G. Brasseur, "A Feasibility Study on Autonomous Online Condition Monitoring of High-Voltage Overhead Power Lines", *IEEE Transactions on Instrumentation and Measurement*, vol. 50, no. 5, pp. 1789-1796, 2009
- [7] K. Chang, S. Kang, K. Park and S. Shin, "Electric Field Energy Harvesting Powered Wireless Sensors for Smart Grid", *Journal of Electrical Engineering & Technology*, Vol. 7, No. 1, pp. 75~80, 2012
- [8] T. Keutel, X. Zhao and O. Kanoun, "Energy Scavenging for Monitoring of Overhead Power Line Networks", in *Proc. IMTC*, pp. 207-211, 2009
- [9] M. J. Moser, T. Bretterkieber, H. Zangl and G. Brasseur, "Strong and Weak Electric Field Interfering: Capacitive Icing Detection and Capacitive Energy Harvesting on a

- 220-kV High-Voltage Overhead Power Line”, *IEEE Transaction on Industrial Electronics*, vol. 58, no. 7, pp. 2597-2604, 2011
- [10] F. Guo, H. Hayat, and J. Wang, “Energy Harvesting Devices for High Voltage Transmission Line Monitoring”, *Power and Energy Society General Meeting*, July, pp. 1-8, 2011
- [11] X. Zhao, T. Keutel and M. Balduaf, “Energy harvesting for a wireless-monitoring system of overhead high-voltage power lines”, *IET Generation, Transmission & Distribution*, vol. 7, issue: 2, pp. 101-107, 2013
- [12] N. M. Roscoe and M. D. Judd, “Harvesting Energy from Magnetic Fields to Power Condition Monitoring Sensors”, *IEEE Sensors Journal*, vol. 13, issue: 6, pp. 2263-2270, 2013
- [13] J. Moon, S.B. Leeb, “Analysis Model for Magnetic Energy Harvesters”, *IEEE Transactions of Power Electronics*, vol.30, issue: 8, pp. 4302-4311, 2015
- [14] R. Moghe, D. Divan, F. Lambert, “Powering Low-Cost Utility Sensors using Energy Harvesting”, *Power Electronics and Applications (EPE 2011)*, in *Proc. 2011-14th European Conference*, pp. 1-10, 2011
- [15] K. Tashiro, H. Wakiwaka, S. Inoue, and Y. Uchiyama, “Energy Harvesting of Magnetic Power-Line Noise”, *IEEE Transactions on Magnetics*, vol. 47, issue: 10, pp. 4441-4444, 2011
- [16] J.P. Amaro, “Energy harvesting for Zigbee compliant Wireless Sensor Network nodes”, *IECON 2012 - 38th Annual Conference on IEEE Industrial Electronics Society*, pp. 2583-2588, 2012
- [17] T. Taithongchai and Ekachai, “Adaptive Electromagnetic Energy Harvesting Circuit for Wireless Sensor Application”, *Electrical Engineering/Electronics, Computer, Telecommunications and Information Technology*, pp. 278-281, 2009
- [18] M. Zhu and P.C. Baker, “Alternative Power Sources for Autonomous Sensors in High Voltage Plant”, *2009 IEEE Electrical Insulation Conference*, pp. 36-40, 2009

- [19] S. Yuan, Y. Huang, Q. Xu, J. Zhou, C. Song and P. Thompson, "Magnetic Field Energy Harvesting Under Overhead Power lines", *IEEE Transactions on Power Electronics*, volume 30, issue 11, May, 2015.
- [20] "Voltage multiplier | Wikiwand", *Wikiwand*, 2016. [Online]. Available: [http://www.wikiwand.com/en/Voltage\\_multiplier](http://www.wikiwand.com/en/Voltage_multiplier). [Accessed: 10- May- 2016].
- [21] "Diode detectors for RF measurement", David W Knight, 2014. [Online]. Available: [http://www.g3ynh.info/circuits/Diode\\_det.pdf](http://www.g3ynh.info/circuits/Diode_det.pdf). [Accessed: 10- May- 2016].
- [22] "BAT54 Series, Schottky Barrier Diodes", NXP Semiconductors, 2012. [Online]. Available: [http://www.nxp.com/documents/data\\_sheet/BAT54\\_SER.pdf](http://www.nxp.com/documents/data_sheet/BAT54_SER.pdf). [Accessed: 10- May- 2016].
- [23] Invisible-systems, Gateway GPRS, GPS & RF, [Online]. <http://www.invisible-systems.com/solutions/pdf/Gateway%20GPRS%20GPS%20RF.pdf>, 2015. [Accessed: 10- May- 2016].
- [24] F. Ongaro, S. Saggini and P. Mattavelli, "Li-Ion Battery-Supercapacitor Hybrid Storage System for a Long Lifetime, Photovoltaic-Based Wireless Sensor Network", *IEEE Transactions on Power Electronics*, vol. 27, no. 9, pp. 3944-3952, 2012.
- [25] P. Proynov, G. Szarka, B. Stark and N. McNeill, "Resistive matching with a feed-forward controlled non-synchronous boost rectifier for electromagnetic energy harvesting", *2013 Twenty-Eighth Annual IEEE Applied Power Electronics Conference and Exposition (APEC)*, 2013.
- [26] P. Proynov, G. Szarka, B. Stark and N. McNeill, "The effect of switching frequency, duty ratio, and dead times on a synchronous boost rectifier for low power electromagnetic energy harvesters", *2012 Twenty-Seventh Annual IEEE Applied Power Electronics Conference and Exposition (APEC)*, 2012.
- [27] G. Szarka, S. Burrow, P. Proynov and B. Stark, "Maximum Power Transfer Tracking for Ultralow-Power Electromagnetic Energy Harvesters", *IEEE Transactions on Power Electronics*, vol. 29, no. 1, pp. 201-212, 2014.



- [28] T. Paing, J. Shin, R. Zane and Z. Popovic, "Resistor Emulation Approach to Low-Power RF Energy Harvesting", *IEEE Transactions on Power Electronics*, vol. 23, no. 3, pp. 1494-1501, 2008.
- [29] V. Boitier, P. Estève, R. Monthéard, M. Bafleur and J. Dilhac, "Under Voltage Lock-Out Design Rules for Proper Start-Up of Energy Autonomous Systems Powered by Supercapacitors", *Journal of Physics.: Conference Series*, vol. 476, p. 012121, 2013.
- [30] J. Kraus, *Electromagnetics*. New York: McGraw-Hill, 1953.
- [31] Fairchild, BAT54/ BAT54A/ BAT54C/ BAT54S Schottky Diodes, 2016. [Online]. Available: <https://www.fairchildsemi.com/datasheets/BA/BAT54.pdf>. [Accessed: 20-May- 2016].
- [32] Vishay, N-Channel 40 V (D-S) MOSFET Si2356DS, [Online]. <http://www.vishay.com/docs/62893/si2356ds.pdf>, [Accessed: 10- May- 2016].
- [33] Invisible-systems, 868 MHz Temperature & Pulse Transmitter, [Online]. <http://www.invisible-systems.com/Transmitters.php#temperature>, [Accessed: 10-May- 2016].
- [34] Linear Technology, LTC1540 Nanopower Comparator with Reference, [Online]. <http://cds.linear.com/docs/en/datasheet/1540fas.pdf>, [Accessed: 10- May- 2016].

## Chapter 6. Future Work and Contributions

### 6.1 Summary

In this thesis, a highly efficient free-standing magnetic field energy harvesting system has been studied, optimized and fabricated. The system can be installed in almost anywhere in a substation or under overhead lines as long as there is an alternating magnetic field. Due to the great flexibility, the proposed system is capable of powering different kinds of wireless sensors deployed near the high voltage equipment.

In Chapter 2, the magnetic field near the high voltage equipment has been investigated. According to the mathematical calculations and published results, a minimum magnetic flux density of  $7 \mu T_{rms}$  is available under overhead power lines or inside electrical substations. In addition, the system overview of a free-standing magnetic field energy harvester has been presented and discussed, including the demagnetization phenomenon, eddy current losses and the relevant circuit design. The knowledge provided in this chapter should be very valuable for researchers who are currently working on this topic or going to start the research in this area.

In Chapter 3, a novel bow-tie-shaped coil has been proposed, designed and optimized. The special design of its geometric shape has made the magnetic flux concentrated in the middle of the core which leads to much greater effective permeability compared to a conventional rod. The core material was selected specifically to eliminate eddy current losses. Mn-Zn Ferrite was identified as the most suitable core material, given its high relative permeability and ultra-low conductivity. Different winding methods have been investigated. The results indicated that the power collected by the coil was not only determined by the types of the enameled wire, but also proportional to volume that the wire occupied. It was demonstrated that the power density of the bow-tie coil designed in this chapter was 15 times greater than a recently reported result if both coils were placed into the same magnetic field.

Chapter 4 introduces a new coil with a special helical core. It also uses the flux concentration technique discussed in Chapter 3. In addition, the special helical-shaped design has

dramatically lengthened the path of the magnetic flux, which reduced the demagnetization factor and led to a much higher power output. The core material was selected by compromising high permeability and low eddy current losses. High permeability ferrite was identified as the most suitable core material, given its high relative permeability and ultra-low conductivity. The geometry shape of the helical core has been optimized to increase the path of the magnetic flux and better utilize the winding area available inside the core. From the experimental results, the power density of a helical coil with only 400 turns was already greater than the proposed bow-tie coil if both coils were placed into the same magnetic field. If the fabricated coil can have 2000 turns of wire, its predicted power density ( $9.9 \mu\text{W}/\text{cm}^3$ ) is 4 times larger than that of the bow-tie coil.

In Chapter 5, an AC-DC converter has been studied and presented. A voltage doubler has been applied to provide full-wave rectification and simultaneously boost the output voltage. A transient analysis has been carried out to calculate the input impedance of a charging capacitor as a function of time. The theoretical analysis indicated that the input impedance was dependent on the input and output voltage. A switch mode power converter has been developed as a matching network. The emulated input resistance looking into the power converter could be a constant and determined by the frequency and the duty cycle of PWM applied on the switch. From the experimental results, the energy conversion efficiency from the harvesting coil to the storage capacitor was around 74.6 %. This value was twice as large as a previously reported design. Finally, an energy management unit has been developed which effectively utilizes the energy stored in the capacitor to power a commercial wireless sensor.

## 6.2 Key Contributions

This work has provided a thorough study on a magnetic field energy harvesting system from the coil design into circuit analysis. The key contributions to new knowledge are detailed as follows:

### 1. Chapters 1&2: Overview of Electromagnetic Field Energy Harvesting

A comprehensive literature review has been presented to illustrate the recent development of the electric field and magnetic field energy harvesting near power infrastructure.

### 2. Chapter 3: Development of a Bow-tie Coil

The idea “flux concentration” is proposed to increase the effective permeability of a ferromagnetic core. Thus, a novel bow-tie-shaped core are designed, fabricated and measured. The energy losses inside the ferromagnetic core are studied and Mn-Zn ferrite is identified as the most suitable core material due to its ultra-low conductivity. Different winding methods are investigated and it is indicated that the power collected by the coil is proportional to volume that the wire occupied. From the experimental result, the power density of the proposed bow-tie coil is 15 times greater than a conventional solenoid if both coils were placed into the same magnetic field.

### 3. Chapter 4: Development of a Helical Coil

On top of the “flux concentration” technique, a new coil with a helical core is proposed. The special design of the helical shape dramatically lengthens the path of the magnetic flux, which reduced the demagnetization factor and lead to a much higher power output. The geometry shape of the helical core is carefully optimized to increase the path of the magnetic flux and better utilize the winding area available inside the core. From the experimental results, the power density of a helical coil with only 400 turns was already greater than a bow-tie coil with 40,000 turns if both coils were placed into the same magnetic field. If the fabricated helical coil can have 2000 turns of wire, its predicted power density ( $9.9 \mu\text{W}/\text{cm}^3$ ) is 4 times larger than that of the bow-tie coil.

### 4. Chapter 5: Impedance Matching and Energy Management System

The work in Chapter 5 focuses on developing a specific circuit system for a magnetic field energy harvester. It effectively utilizes the energy from the harvesting coil to power a wireless sensor. As a capacitor is used as an energy storage unit, a transient analysis is carried out to calculate the input resistance as a function of time. The theoretical analysis indicates that the input resistance is highly related to the input and output voltage. A switch mode power converter is developed as a matching network by only using a switch, a capacitor, an inductor and a diode. Therefore, the input resistance looking into the power converter is a constant and can be tuned by the switching frequency and the duty cycle. From the experimental results, the energy conversion efficiency is around 74.6 %. This value is twice as large as a previously reported design. Finally, an energy management unit is employed to utilize the energy stored in the capacitor to power a commercial wireless sensor and therefore a completed energy harvesting system has been accomplished.

## 6.3 Future Work

Based upon the conclusions above and considering the limitations of the work existed, future research could be carried out in the following areas.

- Although the helical core can have a much better performance compared to other core shapes in terms of the demagnetization factor, the complex physical structure makes it difficult and expensive to fabricate, especial in the bulk-production. Furthermore, ferrite materials are fragile and prone to damage. Further studies are necessary to optimize the structure of the helical core to make it more robust.
- In reality, the direction of the magnetic field near the high power equipment, especial in the electrical substation, always changes with the real-time demand from the grid. Therefore, the harvesting coil should be further optimized to capture the magnetic field coming from different angles.
- In this work, a small wireless sensor can be powered up to transmit a temperature reading in every 10.5 minutes. However, for other sensors with a GPRS module, more energy is required during the active operation. The magnetic field energy harvester can be combined with other energy harvesting systems (e.g. solar panel, electric field energy harvester) to provide a reliable and strong power output to an energy-hungry device.
- The coil proposed in this work may also be a good candidate of magnetic field sensors. Due to the special design of the helical coil, the effective permeability is much larger than a conventional solenoid. A tiny magnetic field in the air can be significantly amplified by the helical core and the open circuit voltage directly indicates the strength of the measured magnetic field. If a proper calibration method is developed, the helical coil is able to measure a tiny magnetic field in the air without using an amplifier circuit.

## Appendix

To calculate the wire resistance, it is critical to figure out how many layers of the enameled wire are wound inside the helical core. The parameter  $K_{total}$  is defined to express the total layer of the enameled wire existing inside a helical core. Some examples are provided in Fig. A.1 to help better understand the definition of  $K_{total}$ .

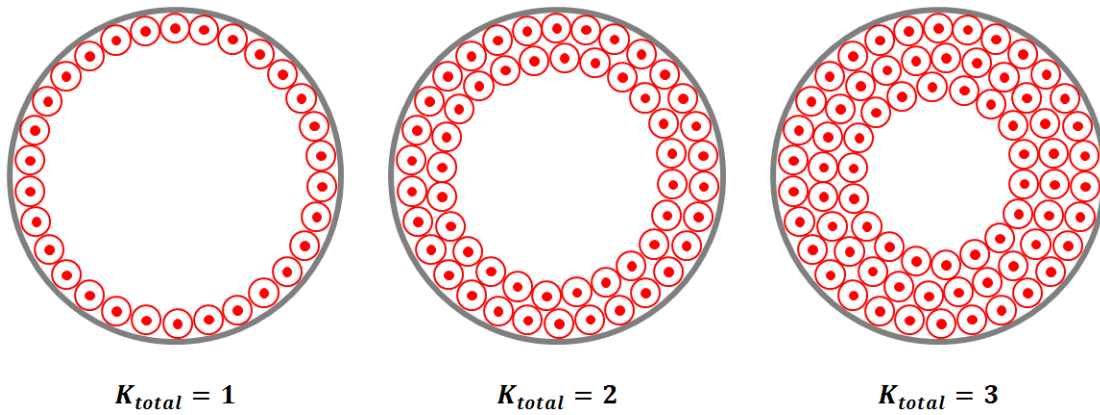


**Fig. A.1. The definition of the total layer of the enameled wire inside a core**

For a particular layer of the wire inside a helical core, the number of turns in this layer  $N_k$  can be correlated to the wedge angle  $\alpha$  shown in Fig. A.2.

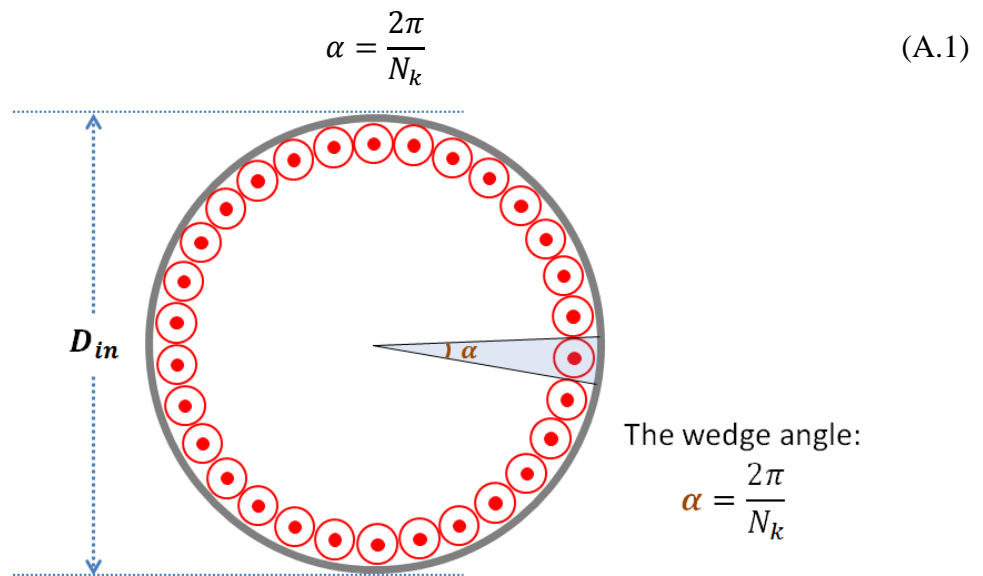


**Fig. A.2. The wedge angle  $\alpha$  defined inside a helical core**

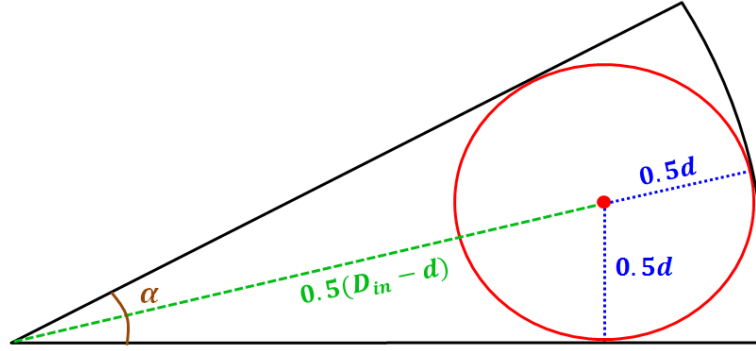


Fig A.3. The parameters of a small wedge

The wedge angle  $\alpha$  can be obtained by:

$$\alpha = 2\arcsin\left(\frac{d}{D_{in} - d}\right) \quad (A.2)$$

where  $d$  is the diameter of the enameled wire and  $D_{in}$  is the inner diameter of helical core shown in Fig. A.3. By combining Equation (12) and (13), the number of turns in this particular layer  $N_k$  can be derived:

$$N_k = \frac{\pi}{\arcsin\left(\frac{d}{D_{in} - d}\right)} \quad (A.3)$$

Assuming that there are  $K_{total}$  layers of enameled wire inside the core, the total number of turns  $N_{total}$  can be calculated by the summation of the number of turns in each layer  $N_k$ .

$$N_{total} = \sum_{k=1}^{K_{total}} N_k = \sum_{k=1}^{K_{total}} \left( \frac{\pi}{\arcsin\left(\frac{d}{D_{in} - (2k-1)d}\right)} \right) \quad (A.4)$$

The length of the enameled wire at the  $k^{th}$  layer  $L_k$  can be expressed by:

$$L_k = N_k(2W_H + 2M_c + 8kd) \quad (A.5)$$

where  $W_H$  is the helical width and  $M_c$  is the core thickness shown in Fig 4.10. The total length of all the enameled wire  $L_{total}$  inside the core can be obtained by the summation of  $L_k$  in each layer.

$$L_{total} = \sum_{k=1}^{K_{total}} L_k = \sum_{k=1}^{K_{total}} (N_k(2W_H + 2M_c + 8kd)) \quad (A.6)$$



By combining Equations (15) and (17), the wireless resistance  $R_{wire}$  can be calculated:

$$R_{wire} = \rho_{wire} \sum_{k=1}^{K_{total}} L_k = \rho_{wire} \sum_{k=1}^{K_{total}} \left( \frac{\pi(2W_H + 2M_c + 8kd)}{\arcsin\left(\frac{d}{D_{in} - (2k-1)d}\right)} \right) \quad (A.7)$$

where  $\rho_{wire}$  is the wire resistance in  $\Omega/\text{m}$ .